Measurement of simultaneous $\Upsilon + J/\psi$ production in PbPb collisions at $\sqrt{s_{NN}} = 5.02$ TeV with the CMS detector

By

GRAHAM WAEGEL
DISSERTATION

Submitted in partial satisfaction of the requirements for the degree of

DOCTOR OF PHILOSOPHY

in

Physics

in the

OFFICE OF GRADUATE STUDIES

of the

UNIVERSITY OF CALIFORNIA

DAVIS

Approved:

Manuel Calderón de la Barca Sánchez, Chair

Daniel Cebra

Ramona Vogt

Committee in Charge

2023

Copyright © 2023 by
Graham Waegel
All rights reserved.

CONTENTS

List of Figures . . . iv

List of Tables . . . xvi

Abstract . . . xvii

1 Theoretical Background **1**

1.1 Standard Model . . . 1

1.2 Quark-Gluon Plasma . . . 3

1.3 Heavy-ion collisions . . . 5

1.4 Heavy quarkonia . . . 7

1.5 Nuclear Modification . . . 9

1.5.1 QGP effects . . . 11

1.5.2 Cold nuclear matter effects . . . 13

1.6 Double quarkonia . . . 15

2 Experimental facilities **19**

2.1 The LHC at CERN . . . 19

2.2 The CMS detector . . . 26

2.2.1 Coordinate system . . . 27

2.2.2 Solenoid magnet . . . 30

2.2.3 Silicon tracker . . . 31

2.2.4 Calorimeters . . . 33

2.2.5 Muon system . . . 35

2.2.6 Trigger system . . . 41

3 Data selection and simulated samples **45**

3.1 Dataset . . . 45

3.2 Monte Carlo . . . 46

3.3 Selections . . . 47

3.4 Double dimuons . . . 51

3.4.1 Triggers in Onia trees 54

4 Analysis **57**

4.1 Signal extraction 57

4.2 Acceptance and efficiency corrections 64

4.3 Prompt and non-prompt J/ψ 69

4.4 Systematic uncertainties 71

4.4.1 Acceptance 71

4.4.2 Efficiency 72

4.4.3 Signal PDF 73

4.4.4 Background PDF 74

4.4.5 Fixed parameters 74

4.5 Closure test 76

5 Results **81**

5.1 Comparison to theory and simulation 84

6 Conclusion **89**

A Scale factors for asymmetric dimuons **91**

LIST OF FIGURES

1.1 Chart of the fundamental particles of the Standard Model [1]. . . . 2

1.2 Results of lattice QCD calculations with several lattice sizes (N_t), using 2+1 flavors (u, d, and s) and realistic quark masses [2]. The horizontal axis represents the temperature T of the system, and the vertical axis represents the ratio of energy density ϵ over T^4. The inset panel shows the temperature range 100–250 MeV of the same plot for greater detail in that region. 5

1.3 Phase diagram of QCD matter. The vertical axis represents the temperature of the system, and the horizontal axis represents the net baryon density (number of baryons minus antibaryons per unit volume of space). The lower left region is the hadronic matter or hadron gas phase, in which quarks and gluons are confined, and the upper region is the QGP phase, where the quarks and gluons are deconfined. The solid line separating these two phases indicates a first-order phase transition, while the dashed line indicates a crossover transition. The critical point between these two types of transition is located at approximately $T \approx 154$ MeV. The far right region is where QCD matter may take more exotic phases. For reference, ordinary nuclear matter such as protons and neutrons are indicated on the diagram at room temperature, approximately ($2.5 \times 10^{-3}\ eV$). 6

1.4 Space-time schematic of a heavy-ion collision at the LHC [3]. The horizontal axis represents distance along the axis of the colliding beams, and the vertical axis represents time. The fireball thermalizes into a QGP at time $\tau_0 < 1$ fm/c. The QGP hadronizes over T_c, which is a range of temperatures because this system is undergoing a crossover transition. Chemical freezeout occurs at temperature T_{chem} and kinetic freezeout at T_{kin}. Arrows indicate particles emitted during the fireball's evolution, including photons and various hadrons. 7
1.5 Diagram of bottomonia (left) and charmonia (right) states [4]. The vertical axis represents mass and the horizontal axis denotes the quantum numbers of the quarkonium state. Arrows indicate decay channels between states. The $B\bar{B}$ threshold (left) indicates at what mass a bottomonium is energetically permitted to decay to $B\bar{B}$, while the $D\bar{D}$ (right) threshold indicates a similar threshold to decay into $D\bar{D}$ for charmonia. 9
1.6 Dimuon invariant mass distributions in Pb+Pb (left) [5] and p+Pb (right) [6] collisions. The black dots are data points, and the dashed red lines are the expected distributions assuming that there is no suppression of Υ yields. 10
1.7 Nuclear modification factors. 10
1.8 Radial wave functions of Υ(1S), (2S), and (3S) states (red solid, blue dashed, and green dotted lines respectively.) calculated from the screened Cornell potential for $T = 0$ MeV (lower) and $T = 200$ MeV (upper) [7]. The RMS radius is labeled for each state. 12
1.9 Diagram of quarkonia states as a thermometer of the QGP [8]. As the temperature of the QGP rises above the critical temperature T_c, quarkonium states progressively melt and disappear. 12

1.10 Real (left) and imaginary (right) parts of the $q\bar{q}$ potential in a QGP medium of various temperatures. [9]. 13

1.11 Left: Parton distribution function of a proton [10]. The horizontal axis is the momentum fraction x, and the vertical axis is the value of the distribution function multiplied by x. The u and d are valence quarks, g is the gluon distribution, and the rest are sea quarks. The gluon distribution is divided by 10 to fit in the plot. Right: Modification of parton distribution functions in a ^{208}Pb nucleus compared to a deuteron. 14

1.12 Diagram of SPS (left) and DPS (right) in a proton-proton collision [11]. In SPS, one parton from each proton interact in a single scattering process (dark circle) to produce two final-state particles. In DPS, two partons from each proton interact in two seperate scattering processes that each produce one final-state particle. 15

1.13 Sketch of three different DPS processes in a collision between two large nuclei containing A nucleons, each resulting in the production of two quarkonia. Upper: two partons from one nucleon interact with two partons from another nucleon. Middle: two partons from one nucleon interact with two partons from two different nucleons. Lower: two partons from two nucleons interact with two partons from two different nucleons. 16

2.1 An aerial photo of the location where the LHC is buried [12]. The LHC ring is drawn in yellow, and smaller accelerators in the complex are in blue and red. The dashed white line indicates the border between France and Switzerland. Also labeled are the two main CERN laboratory sites, as well as the sites for the four main experiments. 20

2.2 Left: Proton source for the LHC [13]. The hydrogen bottle has a capacity of 750 ml, enough to supply the LHC for 200,000 years [14]. Right: Block of isotropically pure lead, used as a source of lead ions in the LHC [15]. One block is 2 cm long and 500 mg. The LHC consumes about 2 mg of lead per hour to produce lead ion beams [16]. 21
2.3 A schematic of the CERN accelerator complex [17]. The labels on the individual accelerators show their year of first operation and their length or circumference in meters. The key accelerators used for producing heavy-ion collisions are LINAC3, the LEIR, the PS, the SPS, and LHC. 22
2.4 Photo of UC Davis graduate students and LHC dipole magnet (blue cylinder) at the magnet test facility at CERN in 2018. From left to right: Ota Kukral, Santona Tuli, Graham Waegel, and Jared Jay. . 24
2.5 Photo of LHC dipole magnet at the magnet test facility at CERN in 2018, viewed from one end. The two capped pipes in the center are the parallel beam pipes through which the particles travel. . . . 25
2.6 Photo of a cross section of the CMS detector [18]. 27
2.7 Diagram of the CMS detector [19], with a cutaway to show the internal components. Key components for this thesis are highlighted in red boxes: the silicon trackers, muon chambers, and solenoid. . . 28
2.8 Diagram of CMS detector cross section. [20]. From the inside out: all particles pass through the silicon tracker; the electron (red line) and photon (dashed blue line) stop and produce showers in the electromagnetic calorimeter; the charged and neutral hadrons (solid and dashed green lines) stops and produce showers in the hadronic calorimeter, and the muon (light blue line) travels all the way out to and through the muon detectors. 29

2.9 Examples of the relation between pseudorapidity η and the angle θ from the beam axis. The angle $\theta = 0$ is parallel to the beam axis, corresponding to $\eta = \infty$, and the angle $\theta = 90^\circ$ is perpendicular to the beam axis, corresponding to $\eta = 0$. 30

2.10 Schematic of one quadrant of the CMS silicon tracker system [21]. The lower left corner of the figure is the collision point at the center of the detector. The x axis represents longitudinal distance along the beamline, and the y axis represents radial distance from the beam. Pseudorapidity values are displayed at the top and right of the figure. The pixel tracker and all parts of the strip tracker are seen: the inner barrel (TIB), the inner endcap (TID), the outer barrel (TOB) and the outer endcap (TEC). Components marked A and B are alignment tubes and beam splitters for a laser alignment system used to calibrate the position of the detector. 32

2.11 Left: Photo of polished $PbWO_4$ crystal with attached photodetector. Right: ECAL module containing 1700 crystals [22]. 34

2.12 Schematic of one quadrant of the CMS hadronic calorimeter [23]. The blue dot in the lower right is the collision point at the center of the detector. The x axis represents longitudinal distance along the beam line, and the y axis represents radial distance from the beam (not labeled). All four parts of the HCAL are shown: the barrel (HB), the the endcap (HE), the forward calorimeter (HF) located farther down the beam line, and the outer calorimeter (HO) located outside the solenoid magnet. The HB is located between the radii of 1.78 m and 2.88 m around the beam line. 35

2.13 Diagram of the muon system layout in one quadrant of the CMS detector [24] with DTs are highlighted in yellow, CSCs in green, and RPCs in blue. The interaction point where collisions occur is in the lower left corner of the figure. The x axis represents longitudianal distance along the beamline, and the y axis represents radial distance from the beam. The angle θ from the beam and equivalent η are displayed at the top and right of the figure. 36
2.14 Diagram of a drift tube [22], illustrating a muon passing through (red arrow) and inducing a signal. 37
2.15 Diagram of a DT chamber [25]. There are three superlayers of four layers each, with the middle superlayer oriented perpendicularly to the outer two. 37
2.16 Transverse cross section of the DT barrel region [22]. The four concentric DT stations are highlighted in blue. 38
2.17 Diagram of CSC [22] showing the trapezoidal panels, anode wires, and cathode strips. 39
2.18 Photo of CSC endcap. [22]. 40
2.19 Diagram of resistive plate chamber [26]. 40
2.20 Event display of an Υ decay candidate in the CMS detector. [27]. The red lines are the reconstructed muon tracks, and the red wireframes are the muon chambers that registered muon tracks. The yellow lines are other tracks registered by the silicon tracker in the same event, and the green squares represent energy deposits in the calorimeters. Event selected by me during 2018 Pb+Pb data taking at CERN. 41

2.21 Diagram of the L1 trigger system of CMS. [28]. Data from the ECAL and HCAL are combined in the regional calorimeter trigger, then sent to the global calorimeter trigger and then the global trigger. The global muon trigger selects muon candidates using data from the DTs, CSCs, and RPCs. The global trigger combines the calorimeter and muon triggers and uses a menu of trigger paths to decide whether to accept or reject the event. For heavy ions, the minimum-bias trigger is based on the HF calorimeter. 44

3.1 Event display of an Υ+J/ψ double-quarkonia candidate. The yellow and orange lines represent tracks in the inner tracker. The green blocks represent energy deposited in the calorimeter, with a segment removed from this display for visibility. The large transparent segments are the muon detectors. The muons from the Υ candidate are highlighted in purple and the muons from the J/ψ candidate are highlighted in blue, with a more noticeable curvature due to their lower p_T. Figure produced by me using Fireworks software [29]. 45

3.2 Invariant mass distributions of dimuons in Pb + Pb 2018 data for various triggers: The Υ-region trigger (yellow) the J/ψ-region trigger (red), and the inclusive double-muon trigger (blue) [30]. 49

3.3 Plots of single muons from simulations of quarkonium decays. The horizontal and vertical axes on both plots represent the η and p_T of the muons, respectively. Left: Transverse momentum and $|\eta|$ of single muons from MC simulated Υ decays, with the acceptance cut shown as the red line. Color from blue to yellow indicates muon count. Right: Single muon acceptance×efficiency from MC simulated J/ψ decays [31]. The acceptance cut for 2018 $\mathrm{Pb} + \mathrm{Pb}$ data is displayed as the green line, located below the black line. The black line represents older acceptance cuts used for 2015 $\mathrm{Pb} + \mathrm{Pb}$ data. Color from blue to red indicates the ratio of reconstructed muons passing acceptance and efficiency selections divided by the generated muons, where a value of 1 means they agree perfectly. . . 50

3.4 Examples of dimuon pair combinations for events with two positive muons (blue circles) and two negative muons (red circles) that pass selections. The lines connecting the muons, labeled 1 through 4, represent opposite-sign dimuons that satisfy the vertex probability selection. Purple lines indicate dimuons that pass the mass-gated trigger and green lines indicate dimuons that do not pass the trigger. The "pairs added" cells show which dimuon pairs in each case satisfy all requirements and would be added to the final dataset, with the color indicating which dimuon is sorted into the m_1 category (purple) and which is sorted into the m_2 category (green). Grey-colored cells denote that the dimuons of that pair will be sorted into the m_1 and m_2 categories according to their mass. 52

3.5 Invariant mass distribution of paired dimuons. The dimuon in the pair that passed the trigger (Υ candidate) is in purple, and the dimuon in the pair that did not pass the trigger (J/ψ candidate) is in green. If both dimuons in a pair passed the trigger, the higher mass dimuon is purple and the lower mass dimuon is green. 53

3.6 Invariant mass distribution of paired dimuons. The mass of the dimuon in the pair that passed the trigger (Υ candidate) is on the horizontal axis labeled m_1 and the mass of the dimuon in the pair that did not pass the trigger (J/ψ candidate) is on the vertical axis labeled m_2. If both dimuons in a pair passed the trigger, the higher-mass dimuon is on the horizontal axis and the lower-mass dimuon is on the vertical axis. 54
3.7 Illustration of dimuon trigger assignment for the case of an event with four muons and three dimuons passing selections. The pairwise invariant mass of the two muons on the left and the two muons on the right are each greater than 7 GeV, and the diagonal pairing in the center is less than 7 GeV. The individual trigger status of each of the four muons stored in the AOD is that they passed the mass-gated trigger. In the Onia tree the center dimuon is marked as passing the trigger despite having invariant mass less than 7 GeV, since both constituent muons are individually flagged as having passed the trigger. 56

4.1 Invariant mass plots of one-dimensional fits of the Υ (left) and the J/ψ (right). 60
4.2 Components of two-dimensional fit to dimuon pairs in data: pure signal component of Υ+J/ψ pairs (upper left panel), ridge component of Υ paired with background dimuons (upper right), ridge component of J/ψ paired with background dimuons (lower left), and pure background component of background dimuons paired with other background dimuons (lower right). 61
4.3 Two-dimensional fit of dimuon pairs in data. The bars represent data and the red wireframe represents the fitted model. 62

4.4 Projections of two-dimensional fit of dimuon pairs in data. The left panel shows the projection onto the Υ axis and the right panel shows the projection onto the J/ψ axis. 63

4.5 Comparison of measured Υ efficiency vs $p_T^{\mu\mu}$(left) with efficiency measurement from Ref. [30]. 68

4.6 Comparison of measured J/ψ efficiency vs $p_T^{\mu\mu}$(left) with efficiency measurement from Ref. [32]. The comparable efficiency on the right plot is shown by the red points. Note that the red points on the right plot are for 0–100% centrality, but the legend displays 0–10%. 69

4.7 Distribution of $c\tau$ in units of standard deviation for dimuons in the mass range of the J/ψ, $3.0 < m_{\mu\mu} < 3.2$. The range of the cut on $c\tau$ is indicated by the red lines. 70

4.8 Fit of J/ψ with no $c\tau$ cut (left) and with $c\tau < 3\sigma$ (right). 70

4.9 Invariant mass plots of Υ (left) and J/ψ (right) from data. All events below and beside the signal peak are subtracted, as delineated by the red lines. 71

4.10 Ratios of data/MC vs p_T for Υ (left) and J/ψ (right) signal counts used for reweighting the MC for acceptance estimation. 71

4.11 Ratios of data/MC as functions of p_T for Υ (left) and J/ψ (right) signal counts used for reweighing the MC for efficiency estimation. . 72

4.12 Percentage differences in double-quarkonia yield between nominal and alternate signal PDF for Υ (left) and J/ψ (right). 74

4.13 Percentage differences in double-quarkonia yield between nominal and alternate background PDF for Υ (left) and J/ψ (right). 75

4.14 Percentage differences in double-quarkonia yield between nominal and alternate signal parameters for Υ (left) and J/ψ (right). 76

4.15 Case 1: Difference between the true number of uncorrelated double quarkonia generated in Monte Carlo and the uncorrelated yield calculated from the fit using Eq. 4.17 The differences are recorded from many pseudoexperiments and plotted twice, in units of percentage of the true number (left) and standard deviation from the fit (right). 78

4.16 Case 1: Difference between the true number of all double quarkonia generated in Monte Carlo and the yield extracted from the pure signal component $N_{\Upsilon,\mathrm{J}/\psi}$ of the fit. The differences are recorded from many pseudoexperiments and plotted twice, in units of percentage of the true number (left) and standard deviation from the fit (right). 79

4.17 Case 2: Difference between the true number of all double quarkonia generated in Monte Carlo and the yield extracted from the pure signal component $N_{\Upsilon,\mathrm{J}/\psi}$ of the fit. The differences are recorded from many pseudoexperiments and plotted twice, in units of percentage of the true number (left) and standard deviation from the fit (right). 79

4.18 Case 2: Difference between the true number of correlated double quarkonia generated in Monte Carlo and the yield of the pure signal component $N_{\Upsilon,\mathrm{J}/\psi}$ minus the uncorrelated yield calculated from Eq. 4.17. The differences are recorded from many pseudoexperiments and plotted twice, in units of percentage of the true number (left) and standard deviation from the fit (right). 80

5.1 Two-dimensional fit of dimuon pairs in data. The bars represent data and the red wireframe represents the fitted model. 82

5.2 Projections of two-dimensional fit of dimuon pairs in data. The left panel shows the projection onto the Υ axis and the right panel shows the projection onto the J/ψ axis. 83

5.3 Pull of two-dimensional fit of dimuon pairs in data. The z-axis represents the difference between the fit and data, divided by the statistical uncertainty of the data in each bin. 83
5.4 Left panel: Two-dimensional plot of dimuon pairs in $p + p$ data from [33]. Right panel: Two-dimensional plot of dimuon pairs in $\mathrm{Pb} + \mathrm{Pb}$ data from this thesis, where the bars represent data and the red wireframe represents the fitted model. 84

A.1 Probability tree of asymmetric dimuons. Green denotes branches that pass the efficiency, and red denotes branches that do not pass. 92

List of Tables

1.1 Mass and dimuon branching ratio for relevent quarkonia [34]. 8

3.1 Dataset for Pb + Pb 2018 5.02 TeV collisions. 46
3.2 Monte Carlo samples for Pb + Pb 2018 5.02 TeV collisions. 47

4.1 Shape parameters of Υ and J/ψ signal PDFs obtained from 1D fits to data and MC. 75

ABSTRACT OF THE DISSERTATION

Measurement of simultaneous $\Upsilon + J/\psi$ production in PbPb collisions at $\sqrt{s_{NN}} = 5.02$ TeV with the CMS detector

The yield of simultaneous uncorrelated production of Υ+J/ψ mesons in $\mathrm{Pb} + \mathrm{Pb}$ collisions at $\sqrt{s_{NN}} = 5.02$ TeV is measured for the first time using data collected by the CMS experiment. Reconstructed Υ and J/ψ candidates are paired together to make a two-dimensional invariant mass distribution, which is fitted with a four-component model that accounts for total signal of correlated+uncorrelated Υ+J/ψ, single-quarkonia Υ+$\mu\mu$ and J/ψ+$\mu\mu$, and pure background $\mu\mu$+$\mu\mu$. The total signal of correlated+uncorrelated Υ+J/ψ directly from the fit is consistent with zero. A new method is devised to calculate the uncorrelated Υ+J/ψ yield alone from the three other fit components, thereby reducing the statistical uncertainty. Using this method, the yield of uncorrelated Υ+J/ψ in the kinematic range ($p_T^{\mu\mu} < 30$ GeV, $\mathrm{y}^{\mu\mu} < 2.4$) is measured to be $1325 \pm 378(\mathrm{stat.}) \pm 437(\mathrm{sys.})$, which is a statistically significant signal of over 3σ. We compare our result to theoretical predictions from a model of correlated and uncorrelated production based on double-parton scattering, and to Glauber Monte Carlo simulations. We find that the model and simulations are consistent with our result within systematic uncertainties. The methods used in this first measurement of Υ+J/ψ in heavy-ion collisions may be useful for future analyses with greater quantities of data.

Chapter 1

Theoretical Background

1.1 Standard Model

The Standard Model of particle physics is the preeminent theory describing the electromagnetic, strong, and weak forces. This model is the culmination of work from many scientists over more than half a century, and is the most successful model to date for the fundamental forces it covers. It has been supported by numerous experiments, most recently the discovery of the Higgs boson [35, 36]. The Standard model is not all-encompassing: it does not explain some phenomena such as dark matter and dark energy, and notably it entirely excludes the fundamental force of gravity. Despite this, the Standard Model is a remarkable achievement that describes a vast portion of known interactions in our universe.

The Standard Model establishes a set of fundamental particles, shown in the chart in Fig. 1.1. They are divided into two categores: Fermions, with half-integer spin; and bosons, with integer spin. The fermions are further subdivided into quarks and leptons. Quarks are the only fundamental fermions to feel the strong force. They also interact via the electromagnetic force (known as Quantum Electrodynamics or QED in the Standard Model) as well as the weak force. There are six "flavors" of quark: up (u), down (d), strange (s), charm (c), bottom (b), and top (t), and also their corresponding antiquarks with opposite electric charge. The masses of quarks vary greatly, from 2 MeV for the u to 173 GeV for t. The next category is the leptons, which are fundamental fermions that do not interact by the strong force. They are the electron (e^-), muon (μ^-), tau (τ^-), their positively-charged antiparticles, and also three neutrinos ν_e, ν_μ, and ν_τ. Electrons are the most common lepton that we are familiar with, as they surround the nuclei of atoms in everyday matter. The muon and tau are similar to the electron, but much more massive and unstable. Charged leptons interact through QED and the weak force, while neutrinos interact through only the weak force. There are five fundamental bosons in the Standard Model. The first four are force carriers for the fundamental forces: gluons (g) mediate the strong force, the photon (γ) is a massless particle that propagates the electromagnetic force, and the W and Z bosons carry the weak force. Lastly, the Higgs boson (H) is responsible for how all the fundamental particles obtain their mass.

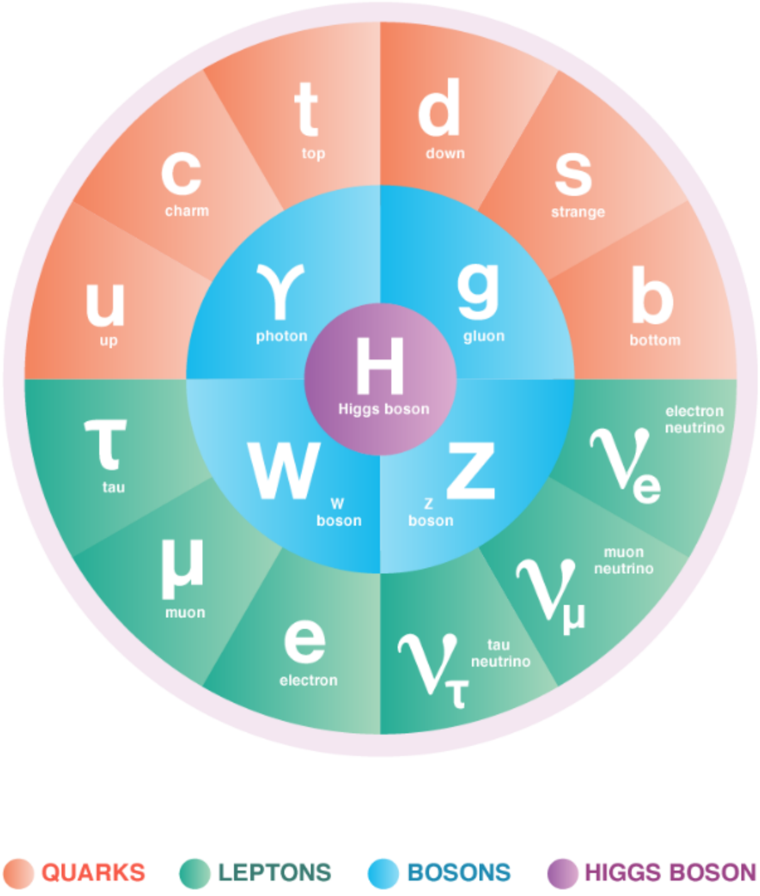
t
top
d
down
c
charm
s
strange
u
up
b
bottom
γ
photon
g
gluon
H
Higgs boson
τ
tau
W
W boson
Z
Z boson
ν_e
electron neutrino
μ
muon
ν_μ
muon neutrino
e
electron
ν_τ
tau neutrino
QUARKS
LEPTONS
BOSONS
HIGGS BOSON

Figure 1.1. Chart of the fundamental particles of the Standard Model [1].

This thesis will focus on the interactions of quarks and gluons, which will be further described in the following sections. Muons will also play a key role in the experimental method, as we search for unstable particles made of $c\bar{c}$ and $b\bar{b}$ which decay into muon pairs.

1.2 Quark-Gluon Plasma

In the Standard Model, the strong force is described by Quantum Chromodynamics (QCD). This force governs the behavior of quarks and gluons. In addition to electric charge (+2/3 for u, c, and t, -1/3 for d, s, and b), quarks also possess a "color" charge. There are three different color charges, arising because QCD is invariant under SU(3) symmetry [37, 38]. To distinguish the three types of charge they were given the names red, green, and blue; or for antiquarks, the colors are antired, antigreen, and antiblue. This naming scheme is the source of the name Chromodynamics in QCD, and has led the strong force to also be called the color force. Gluons are the fundamental force-carrier boson for the strong force, and they possess color themselves. Having color charge notably means that gluons interact with each other, unlike the neutral photon that mediates the electromagnetic force. Another consequence of SU(3) symmetry is that there are eight different gluons, each of them a different superposition of color and anticolor states [38].

A significant feature of QCD is color confinement. The magnitude of the interaction between colored particles increases with the distance between them, which causes the particles to bind together into colorless objects called hadrons. The allowed colorless states in QCD lead to two categories of hadrons: baryons, which are a bound state of three quarks; and mesons, which are a bound state of a quark and antiquark. If the quarks are pulled apart from each other, the potential energy from the strong force increases so much that, out of this energy, new quarks and gluons can be produced to bind with the quarks what were pulled apart such that they are once again bound into a hadron and the fields are "confined." This state of matter is what makes up the universe today, with baryons making up the nuclei of all atoms in the form of protons (uud) and neutrons (udd). Light mesons (pions) serve as a long-range mediator of the strong force between hadrons and thereby bind the atomic nucleus together.

However, hadronic matter is not the only phase of QCD matter. At very high energy density, the system undergoes a phase transition to a different form of matter called the quark-gluon plasma (QGP). In the QGP phase, the quarks and gluons are deconfined and interact freely without binding into hadrons. This can be thought of as analogous to an electromagnetic plasma, where electrons dissociate from nuclei to travel freely and interact throughout the medium. Figure 1.2 illustrates the phase transition between hadronic matter and QGP in a lattice QCD calculation [2]. There is an increase in ϵ/T^4 with rising T, where ϵ is the energy density and T is the temperature of the system. This corresponds to a proportional increase in the number of degrees of freedom in the system, arising from individual quarks and gluons that are no longer bound within hadrons. The rise is steepest at a temperature of approximately 154 MeV, indicating that the phase transition occurs around this temperature. Because there is no discontinuity, this rise is characteristic of a crossover transition, and so $T_c = 154$ MeV is called the "crossover temperature" of the QGP.

The nature of the phase transition from hadron gas to QGP varies. Lattice QCD calculations are at a baryon chemical potential of $\mu_B = 0$, which corresponds to zero net baryon density (number of baryons minus antibaryons per unit volume of space). Depending on the net baryon density in the system, the transition could be first-order or crossover [39]. A first-order phase transition is characterized by a discontinuity in the relevent thermodynamic variable, while a crossover is a smooth transition with no discontinuity as seen in the lattice calculation in Fig. 1.2. The phases of QCD matter and the different phase transitions are shown in Fig. 1.3. Ordinary nuclear matter at room temperature (about 2.5×10^{-3} eV) is in the hadronic phase. At extremely high baryon density, more exotic phases of QCD matter such as color superconductors may exist [40].

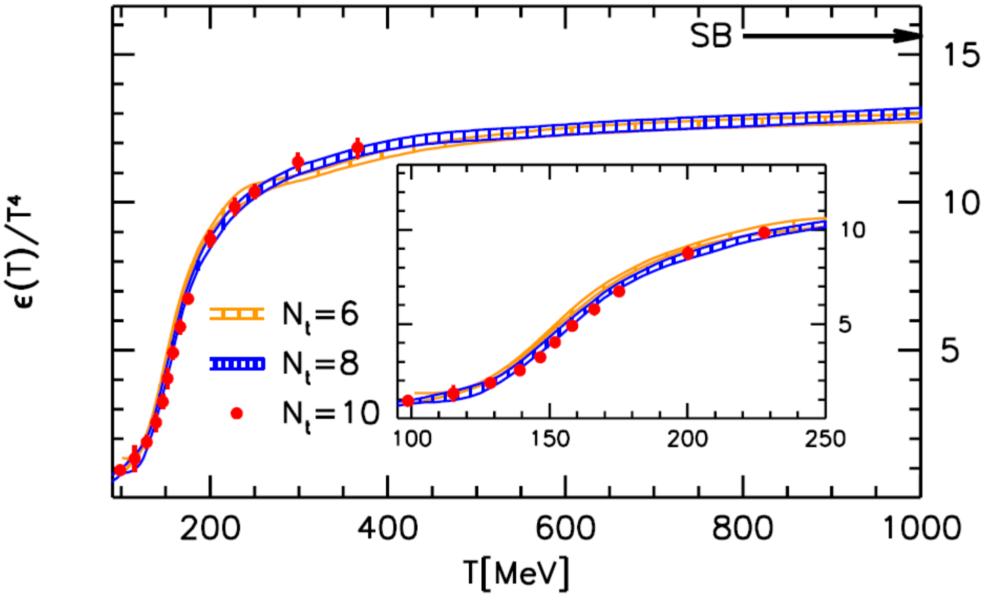

Figure 1.2. Results of lattice QCD calculations with several lattice sizes (N_t), using 2+1 flavors (u, d, and s) and realistic quark masses [2]. The horizontal axis represents the temperature T of the system, and the vertical axis represents the ratio of energy density ϵ over T^4. The inset panel shows the temperature range 100–250 MeV of the same plot for greater detail in that region.

Heavy-ion collisions are used to probe the QCD phase space. The matter in these high-energy collisions thermalizes to produce QGP, with the exact location in phase space depending on the collision that produced it. At the Large Hadron Collider (LHC), high-energy collisions of lead nuclei produce QGP at very high temperature and relatively low net-baryon density. This QGP, located near the vertical axis of Fig. 1.3, would then go through a crossover transition with properties very close to those studied with lattice QCD. At the Relativistic Heavy Ion Collider (RHIC), collisions are produced with various parameters to probe different regions of phase space and search for the critical point [41]. This thesis uses data from $\mathrm{Pb}+\mathrm{Pb}$ collisions at the LHC. The following section will describe heavy-ion collisions in further detail.

1.3 Heavy-ion collisions

In a relativistic heavy-ion collision, the energy from two colliding nuclei traveling near the speed of light is converted into an expanding fireball of dense color matter

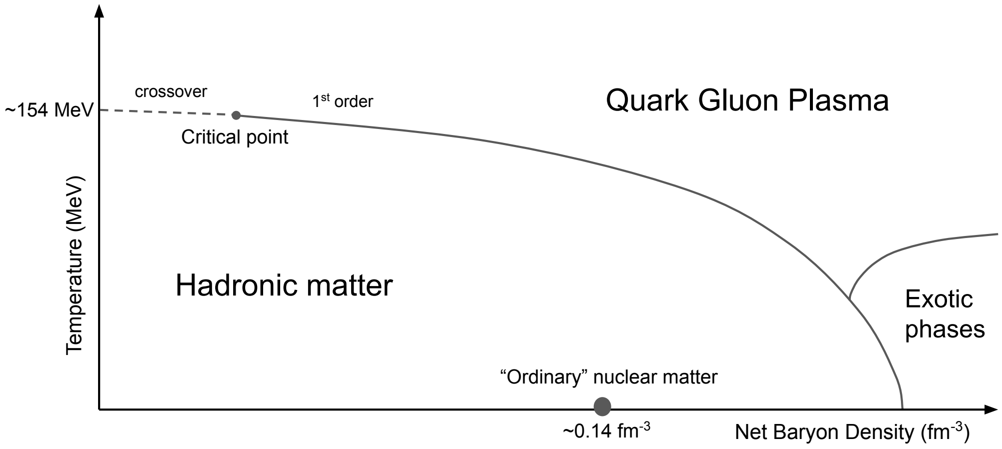

Figure 1.3. Phase diagram of QCD matter. The vertical axis represents the temperature of the system, and the horizontal axis represents the net baryon density (number of baryons minus antibaryons per unit volume of space). The lower left region is the hadronic matter or hadron gas phase, in which quarks and gluons are confined, and the upper region is the QGP phase, where the quarks and gluons are deconfined. The solid line separating these two phases indicates a first-order phase transition, while the dashed line indicates a crossover transition. The critical point between these two types of transition is located at approximately $T \approx 154$ MeV. The far right region is where QCD matter may take more exotic phases. For reference, ordinary nuclear matter such as protons and neutrons are indicated on the diagram at room temperature, approximately $(2.5 \times 10^{-3}\ eV)$.

and energy. This fireball evolves through several stages, as illustrated in Fig. 1.4. First, the system reaches thermal equilibrium and forms the QGP in less than 1 fm/c ($\sim 3 \times 10^{-24}$ s). The QGP then expands and cools. As it reaches the crossover temperature $T_c \approx 154$ MeV, the quarks and gluons begin to hadronize. For collisions at the LHC this is a crossover phase transition, so hadronization occurs gradually over a temperature range. The timescale for hadronization is on the order of ~ 10 fm/c. The system, now a hadron gas, continues expanding and cooling. Soon after hadronization it reaches the stage of chemical freezeout, where inelastic collisions between the hadrons cease. At this point, all particle identities are fixed except for electromagnetic and weak decays. After further expansion, approximately 20–30 fm/c since the initial collision, the system reaches kinetic freezeout, where elastic collisions cease as well. At this point the momenta of outgoing particles are fixed, and they continue to travel outward to the various particle detectors surrounding the collision point.

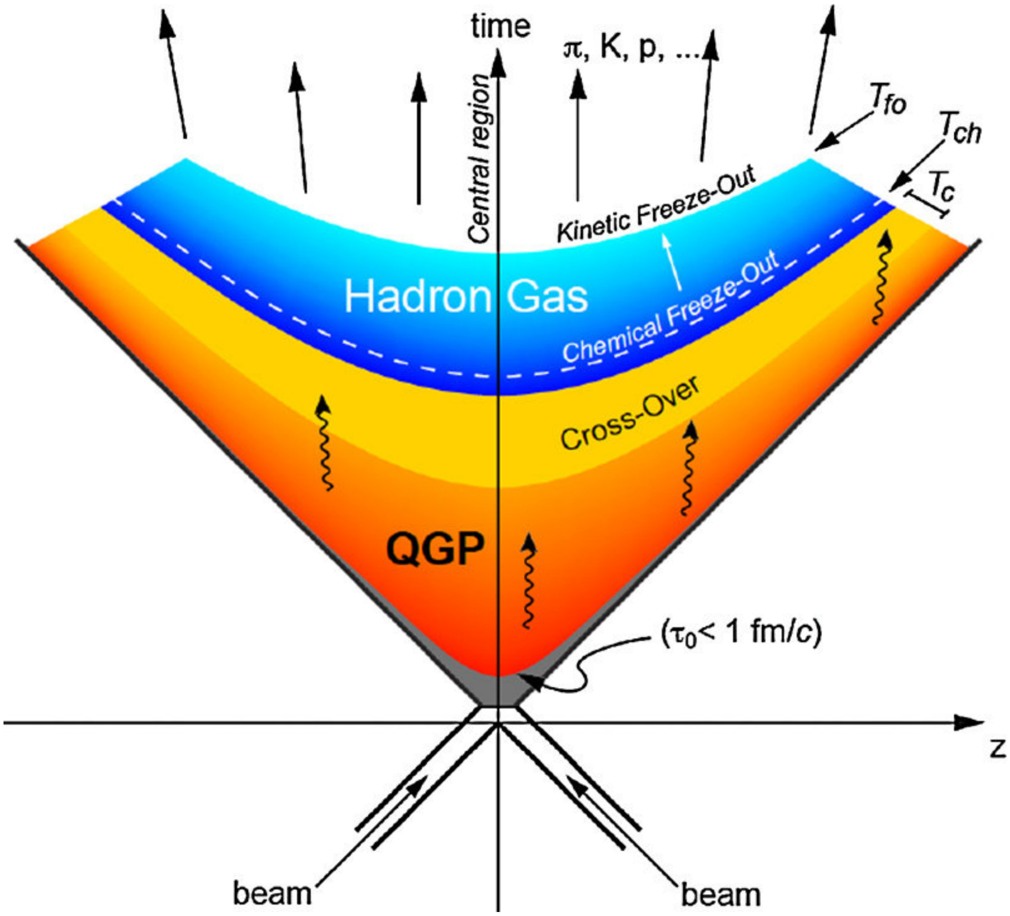
time
π, K, p, ...
Central region
T_{fo}
T_{ch}
T_c
Kinetic Freeze-Out
Hadron Gas
Chemical Freeze-Out
Cross-Over
QGP
(τ_0< 1 fm/c)
z
beam
beam

Figure 1.4. Space-time schematic of a heavy-ion collision at the LHC [3]. The horizontal axis represents distance along the axis of the colliding beams, and the vertical axis represents time. The fireball thermalizes into a QGP at time $\tau_0 < 1$ fm/c. The QGP hadronizes over T_c, which is a range of temperatures because this system is undergoing a crossover transition. Chemical freezeout occurs at temperature T_{chem} and kinetic freezeout at T_{kin}. Arrows indicate particles emitted during the fireball's evolution, including photons and various hadrons.

1.4 Heavy quarkonia

Quarkonia are mesons, bound states consisting of a quark and antiquark of the same flavor, typically the heavier quarks b and c. These two families of quarkonia are known as bottomonia ($b\bar{b}$) and charmonia ($c\bar{c}$). Top quarks do not form quarkonia, as they decay too rapidly.

Heavy quarkonia are useful tools for studying the QGP in heavy-ion collisions. The coupling constant of QCD decreases with increasing energy, and heavy quarkonia have high enough mass that they can be studied using perturbation theory. Their high mass, especially for the Υ, also means that their production is dominated by initial hard-scattering in the collision rather than thermal production [42], and the formation time for a $q\bar{q}$ to form a quarkonium state is $\lesssim 0.1$ fm/c [43]. In addition, these quarkonia have long enough lifespans (> 1000 fm/c) to outlast the QGP before they decay. This means they experience the full evolution of the QGP and can be used to probe its properties. Finally, quarkonia have a significant decay mode to muon pairs, which can then be measured by appropriate detectors. Section 2.2 will discuss detectors in more detail. Masses and dimuon branching ratios for relevent quarkonia are shown in Table 1.1.

Table 1.1. Mass and dimuon branching ratio for relevent quarkonia [34].

State	Mass (MeV/c^2)	Dimuon branching ratio (%)
Υ(1S)	$9460.40 \pm 0.09 \pm 0.04$	2.48 ± 0.04
J/ψ	3096.900 ± 0.006	5.961 ± 0.033

This thesis studies two quarkonia, the Υ(1S) and the J/ψ, which are the ground states of bottomonium and charmonium respectively. Figure 1.5 displays the bottomonium (left) and charmonium (right) families with their excited states. As seen in the figure, higher mass quarkonium states can decay to lower mass states and contribute to their final yields. These processes are referred to as "feed-down". The Υ(4S) and higher excited states of bottomonium that are above the $B\bar{B}$ threshold in mass instead decay strongly to $B\bar{B}$, where the B is a meson consisting of a b or $\bar{b}$ quark and another light quark or antiquark. Likewise, excited states of charmonium above the $D\bar{D}$ threshold decay strongly to $D\bar{D}$, where the D is a meson consisting of a c or $\bar{c}$ quark and another light quark or antiquark. These strong decays are energetically forbidden below their respective mass thresholds, but above the threshold they occur very rapidly due to the strength of the strong force. Therefore, they do not contribute to feed-down to the lower quarkonium states.

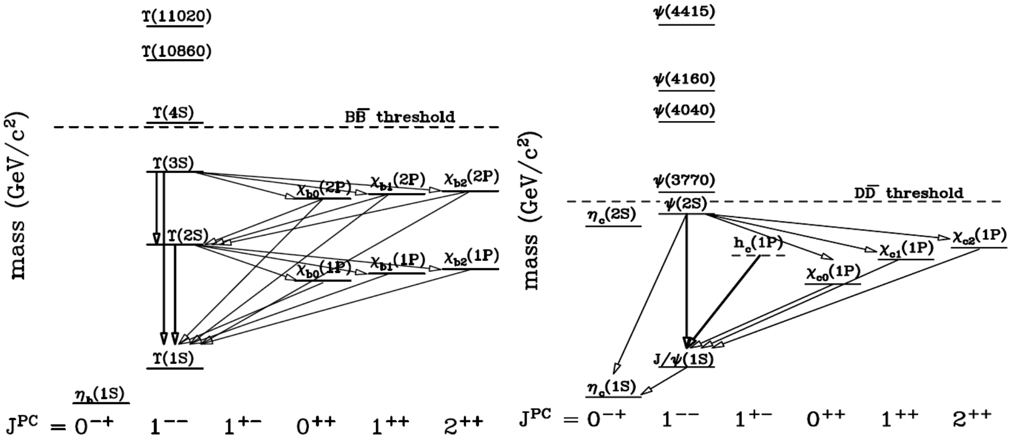
Υ(11020)
Υ(10860)
Υ(4S)
$B\bar{B}$ threshold
Υ(3S)
χ_{b0}(2P)
χ_{b1}(2P)
χ_{b2}(2P)
Υ(2S)
χ_{b0}(1P)
χ_{b1}(1P)
χ_{b2}(1P)
Υ(1S)
η_b(1S)
mass (GeV/c²)
J^{PC} = 0^{-+} 1^{--} 1^{+-} 0^{++} 1^{++} 2^{++}
ψ(4415)
ψ(4160)
ψ(4040)
ψ(3770)
$D\bar{D}$ threshold
η_c(2S)
ψ(2S)
h_c(1P)
χ_{c0}(1P)
χ_{c1}(1P)
χ_{c2}(1P)
J/ψ(1S)
η_c(1S)
mass (GeV/c²)
J^{PC} = 0^{-+} 1^{--} 1^{+-} 0^{++} 1^{++} 2^{++}

Figure 1.5. Diagram of bottomonia (left) and charmonia (right) states [4]. The vertical axis represents mass and the horizontal axis denotes the quantum numbers of the quarkonium state. Arrows indicate decay channels between states. The $B\bar{B}$ threshold (left) indicates at what mass a bottomonium is energetically permitted to decay to $B\bar{B}$, while the $D\bar{D}$ (right) threshold indicates a similar threshold to decay into $D\bar{D}$ for charmonia.

1.5 Nuclear Modification

One phenomenon that has been studied in quarkonium is the suppression of their yields in heavy-ion collisions relative to $p + p$ collisions [5, 6, 44]. Figure 1.6 illustrates this suppression as measured for the Υ family in Pb + Pb (left) and $p +$ Pb (right) collisions. We see that Υ yields are significantly lower than would otherwise be expected without suppression, especially in Pb + Pb. Measurements of the ratio of yields in Pb + Pb and $p +$ Pb collisions versus $p + p$ collisions, referred to as nuclear modification factors R_{PbPb} and R_{pPb} respectively, are shown in Fig. 1.7. These measurements show numerically the suppression in Υ compared to $p + p$. Moreover, they also indicate that excited states of quarkonia exhibit progressively greater suppression.

There are several mechanisms by which the presence of a medium may cause suppression of quarkonia. Some suppression is from interaction with the QGP

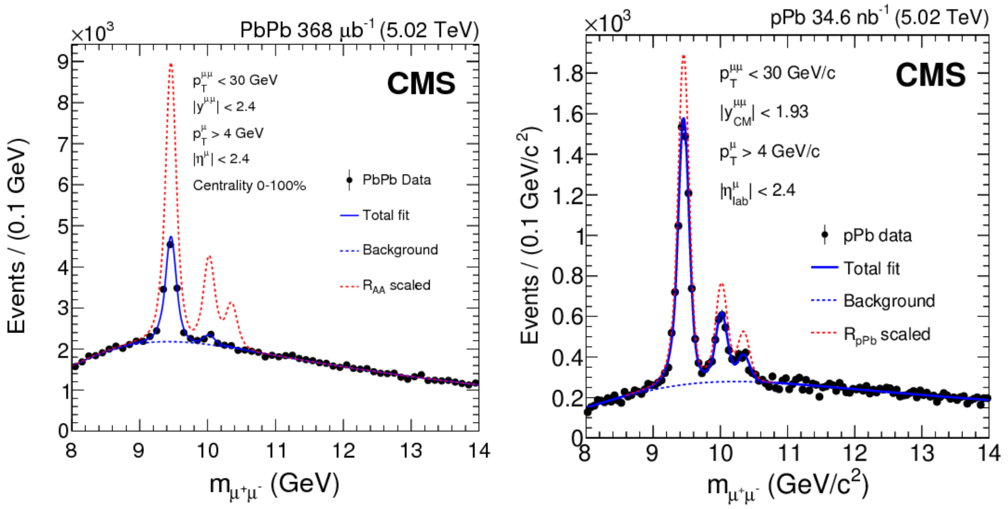

Figure 1.6. Dimuon invariant mass distributions in Pb+Pb (left) [5] and p+Pb (right) [6] collisions. The black dots are data points, and the dashed red lines are the expected distributions assuming that there is no suppression of Υ yields.

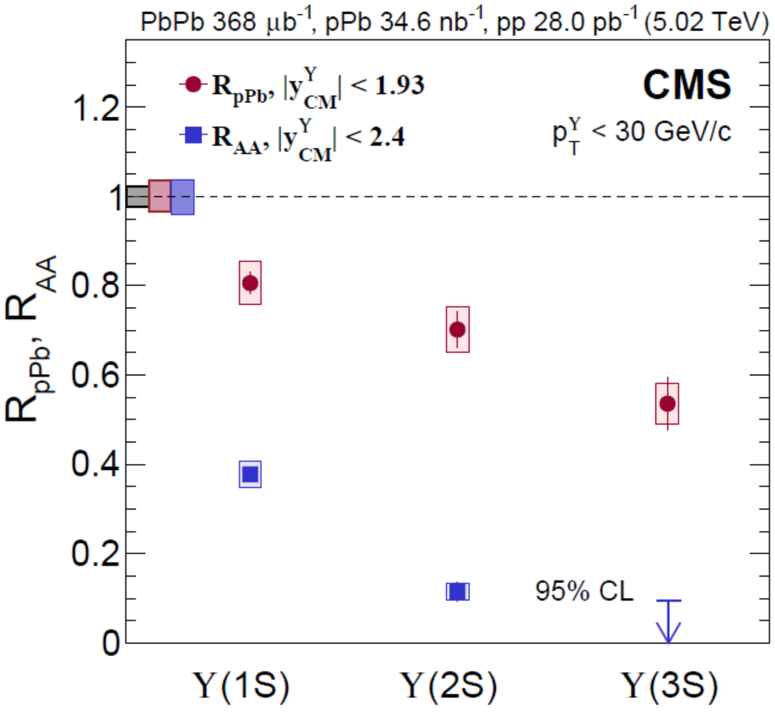

Figure 1.7. Nuclear modification factors.

effects, while some is caused by the presence of the nucleus itself. These will be described further below. Since p + Pb collisions are not expected to produce significant QGP, comparing both Pb+Pb and p+Pb helps to separate the different sources of suppression.

1.5.1 QGP effects

One model proposed to explain the suppression of quarkonia in a QGP is color screening [45], analogous to Debye screening in electromagnetism. This model suggests that when a $c\bar{c}$ (or $b\bar{b}$) pair is within a QGP medium, the color field of the plasma "screens" the quark and antiquark from each other, preventing them from binding to form a quarkonium.

At a temperature of $T = 0$, the potential of a $q\bar{q}$ bound state is modeled with a Cornell potential,

$$V\left(r\right) = \sigma r - \frac{\alpha}{r}, \tag{1.1}$$

where r is the distance between the quark and the antiquark, $\sigma \simeq 0.192$ GeV^2 is the strength of the linear term, and $\alpha = 0.471$ is the strength of the Coulomb term [7]. In the presence of a medium with nonzero temperature, both terms of the potential are modified. The modified potential can be written as

$$V\left(r, T\right) = \sigma r_D \left(1 - e^{-r/r_D}\right) - \left(\frac{\alpha}{r_D} + \frac{\alpha}{r} e^{-r/r_D}\right), \tag{1.2}$$

in which $r_D(T)$ is the temperature-dependent Debye radius [7]. The Debye radius here is parameterized as

$$r_D^{-1}\left(T\right) = T\left[2\pi\alpha_s \frac{2N_c + N_f}{6}\right]^{1/2}, \tag{1.3}$$

where $N_c = 3$ is the number of QCD colors, $N_f = 3$ is the number of QCD flavors, and α_s is the coupling constant of the strong force, which at the Υ(1S) mass is ~ 0.2 [7]. When the Debye radius is small enough compared to the binding radius of the quarkonium state, the q and $\bar{q}$ are screened from each other, preventing the state from forming. The effect of screening on the wave functions of Υ states is visualized in Fig. 1.8. Notably, the excited states are affected more strongly by screening. This leads to a sequence in which a QGP medium of increasing temperature "melts" the states in order, starting with Υ(3S), then (2S), then (1S).

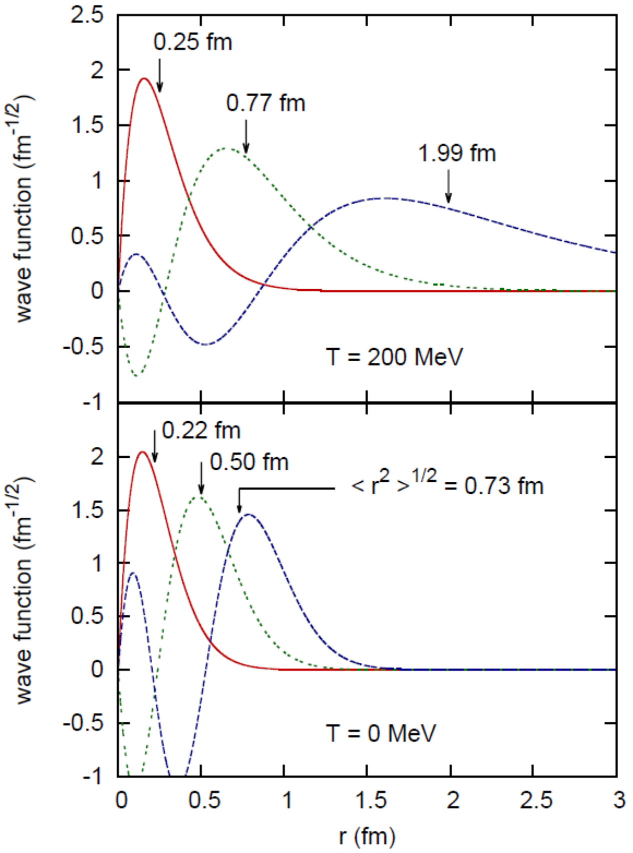

Figure 1.8. Radial wave functions of Υ(1S), (2S), and (3S) states (red solid, blue dashed, and green dotted lines respectively.) calculated from the screened Cornell potential for $T = 0$ MeV (lower) and $T = 200$ MeV (upper) [7]. The RMS radius is labeled for each state.

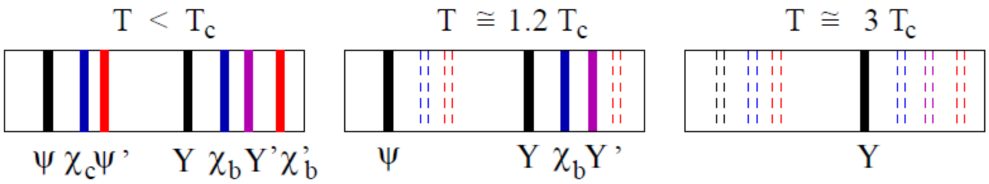

Figure 1.9. Diagram of quarkonia states as a thermometer of the QGP [8]. As the temperature of the QGP rises above the critical temperature T_c, quarkonium states progressively melt and disappear.

Sequential melting of quarkonia can thereby be used as a thermometer to measure the temperature of the QGP, as illustrated by the simplified cartoon in Fig 1.9.

There have also been studies that consider color screening in more detail by examining both real and imaginary portions of the potential [9]. Graphs of these real and imaginary parts of the potential are shown in Fig. 1.10 for various temperatures, from purple (coolest) to red (hottest). The plot of the real part of the potential (left) shows the linear term flattening as the temperature rises, allowing the q and $\bar{q}$ to separate further and increasing the radius of the quarkonium as seen in Fig. 1.8. The right plot of Fig. 1.10 shows the imaginary part of the potential, which affects the width of the quarkonium state and correspondingly its lifetime. It is also related to gluo-dissociation where gluons break up the quarkonium state [9], leading to another mechanism of quarkonium suppression.

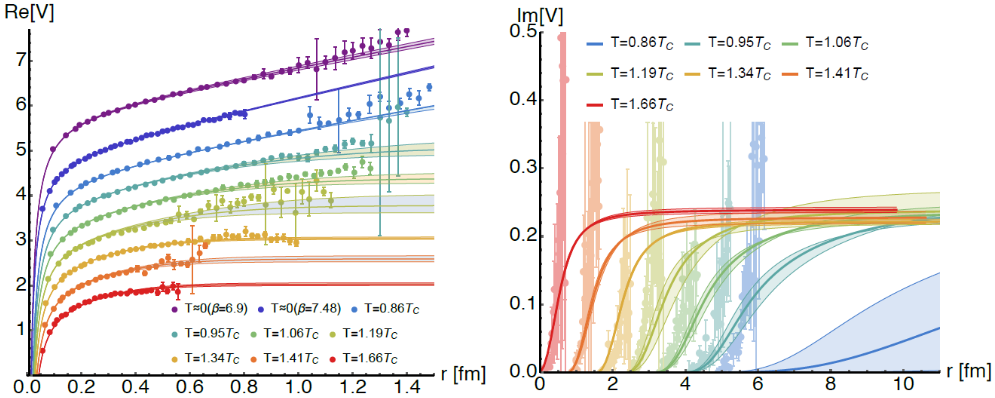

Figure 1.10. Real (left) and imaginary (right) parts of the $q\bar{q}$ potential in a QGP medium of various temperatures. [9].

In addition to color screening, quarkonia yields may be influenced by effects known as regeneration and recombination [46]. This refers to formation of quarkonia after the initial hard scattering from $q\bar{q}$ pairs present in the QGP close enough in phase space to bind together. These could be uncorrelated q and $\bar{q}$ produced thermally in the plasma [47], or they might be from the dissociation of former quarkonia. This process leads to an enhancement in the quarkonium yield. Statistical recombination is much less significant for Υ than for J/ψ, as there are fewer $b\bar{b}$ present in the QGP [48].

1.5.2 Cold nuclear matter effects

Even without the formation of a QGP, the presence of a nucleus in a heavy-ion collision can influence the yield of quarkonia. Referred to as cold nuclear matter (CNM) effects, there are several mechanisms by which this can happen.

The first CNM effect is shadowing and anti-shadowing, which refers to the modification of parton distribution functions within a nucleus [49]. A parton distribution function indicates what fraction of a nucleon's momentum is carried by each parton within it, as seen for a proton in Fig. 1.11 (left). The proton does not only consist of three quarks, uud, but also numerous gluons and sea quarks. The valence uud quarks of the proton are exhibited in Fig. 1.11 by the u and d curves, where the u PDF is approximately twice as large as the d PDF, and they both peak at $x \approx 1/3$. Meanwhile, the sea quarks and gluons tend to carry small x. Gluons are extremely dominant at small x, so much that the distribution is divided by 10 to fit on the plot.

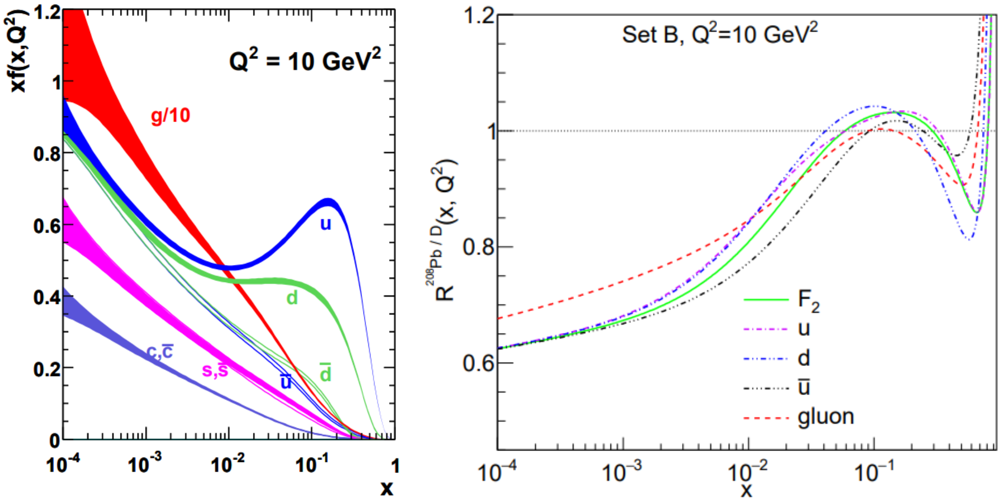

Figure 1.11. Left: Parton distribution function of a proton [10]. The horizontal axis is the momentum fraction x, and the vertical axis is the value of the distribution function multiplied by x. The u and d are valence quarks, g is the gluon distribution, and the rest are sea quarks. The gluon distribution is divided by 10 to fit in the plot. Right: Modification of parton distribution functions in a ^{208}Pb nucleus compared to a deuteron.

The right plot of Fig. 1.11 shows an example of modifications to the parton distribution functions in a ^{208}Pb nucleus relative to those in a deuteron. The effect at small x, where the ratio is < 1, is called shadowing. At medium x where the modification is > 1, the effect is called anti-shadowing. The local minimum at large x is called the EMC effect, named as such because it was first discovered by the European Muon Collaboration (EMC) [50]. Shadowing is considered an "initial-state" effect, as it affects partons from the colliding nucleons before they hadronize into a new quarkonium.

Two more CNM mechanisms are energy loss by particles travelling though the nucleus [51] and interactions with comovers [52]. As opposed to shadowing, comover interaction is a "final-state" effect, while energy loss can be both initial- and final-state.

1.6 Double quarkonia

In rare cases, multiple quarkonia may be produced in a single collision. Processes that produce two quarkonia can be categorized into two types: single parton scattering (SPS) and double parton scattering (DPS). In SPS for proton-proton collisions, a single parton from each of the two colliding protons take part in the process, where those two partons interact to produce two quarkonia. In DPS, two partons from each colliding proton take part in the process, such that the four partons scatter to produce the two quarkonia in the final state. Figure 1.12 illustrates these two processes. In heavy ion collisions multiple nucleons may participate from each nucleus, which expands the possibilities for DPS processes. There are three contributions to DPS in these collisions, illustrated in Fig. 1.13, each with cross sections that scale differently as described by [53] and briefly summarized below.

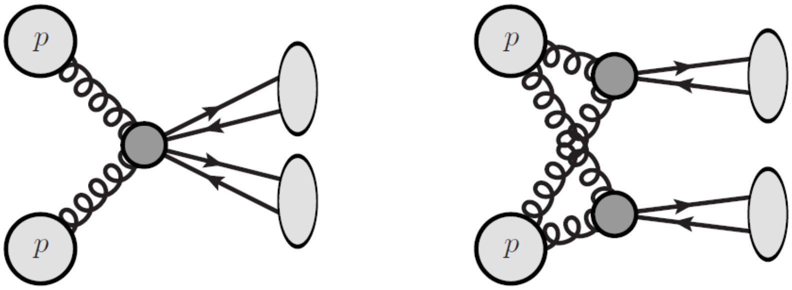

Figure 1.12. Diagram of SPS (left) and DPS (right) in a proton-proton collision [11]. In SPS, one parton from each proton interact in a single scattering process (dark circle) to produce two final-state particles. In DPS, two partons from each proton interact in two seperate scattering processes that each produce one final-state particle.

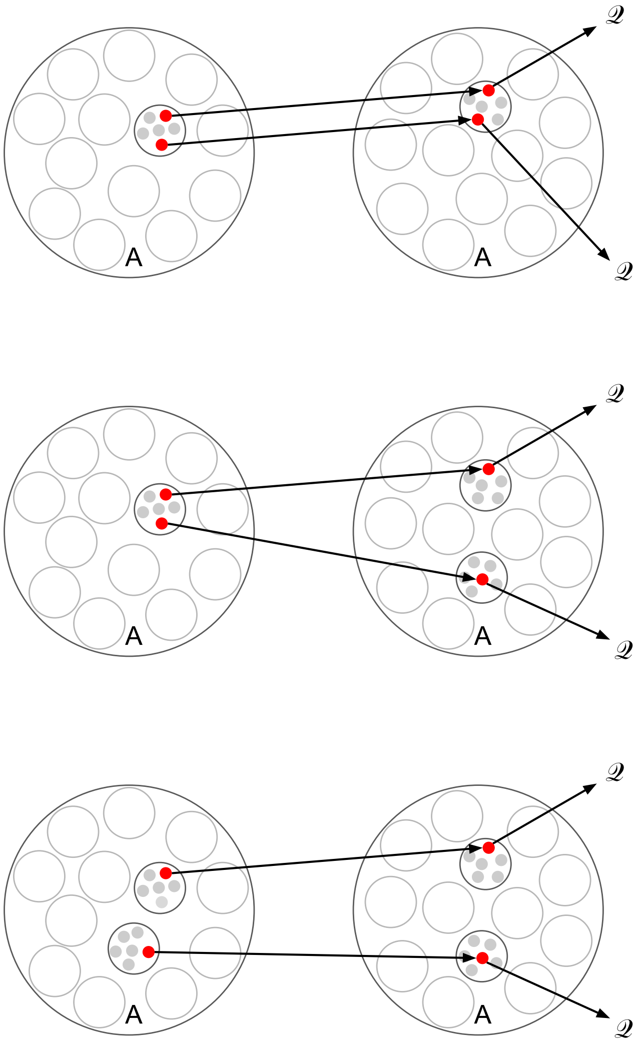

Figure 1.13. Sketch of three different DPS processes in a collision between two large nuclei containing A nucleons, each resulting in the production of two quarkonia. Upper: two partons from one nucleon interact with two partons from another nucleon. Middle: two partons from one nucleon interact with two partons from two different nucleons. Lower: two partons from two nucleons interact with two partons from two different nucleons.

In the first case, two partons from one nucleon interact with two partons from another nucleon, as shown in Fig. 1.13 (upper). The cross section from this interaction scales with the A of the colliding nuclei, as

$$\sigma^{\mathrm{DPS},1}_{AA\to ab} = A^2 \cdot \sigma^{\mathrm{DPS}}_{NN\to ab}, \tag{1.4}$$

where $\sigma^{\mathrm{DPS}}_{NN\to ab}$ is the cross section in a nucleon-nucleon collision such as $p+p$.

In the second case, two partons from one nucleon interact with two partons from two different nucleons, as shown in Fig. 1.13 (middle). For central, head-on collisions of large nuclei in which $A-1\approx A$, the cross section of this interaction is approximately

$$\sigma^{\mathrm{DPS},2}_{AA\to ab}\approx 2A\cdot\sigma^{\mathrm{DPS}}_{NN\to ab}\cdot\sigma_{\mathrm{eff,pp}}\cdot T_{\mathrm{AA}}\left(0\right), \tag{1.5}$$

where $\sigma_{\mathrm{eff,pp}}$ is a normalization cross section that has been experimentally measured [54, 55, 56], and $T_{\mathrm{AA}}\left(0\right)$ is the nuclear overlap function [4, 57] at an impact parameter of $b=0$.

Finally, in the third case, two partons from two nucleons interact with two partons from two different nucleons, as shown in Fig. 1.13 (lower). The cross section of this interaction is approximately

$$\sigma^{\mathrm{DPS},2}_{AA\to ab}\approx\frac{A^2}{2}\cdot\sigma^{\mathrm{DPS}}_{NN\to ab}\cdot\sigma_{\mathrm{eff,pp}}\cdot T_{\mathrm{AA}}\left(0\right), \tag{1.6}$$

under the same assumptions as the previous case.

The total DPS cross section can be described using the “pocket formula” from [53],

$$\sigma^{\mathrm{DPS}}_{AA\to ab}=\frac{m}{2}\frac{\sigma^{\mathrm{SPS}}_{NN\to a}\cdot\sigma^{\mathrm{SPS}}_{NN\to b}}{\sigma_{\mathrm{eff,AA}}}, \tag{1.7}$$

where the DPS contributions of the three interactions from above are contained in the normalization factor

$$\sigma_{\mathrm{eff,AA}}=\frac{1}{A^2\left[\sigma^{-1}_{\mathrm{eff,pp}}+\frac{2}{A}T_{\mathrm{AA}}\left(0\right)+\frac{1}{2}T_{\mathrm{AA}}\left(0\right)\right]}. \tag{1.8}$$

The relative contributions of the three terms in the denominator are $1:4:200$. The dominant third term, which is present only in collisions of heavy nuclei on heavy nuclei, represents quarkonia pairs produced by independent nucleon-nucleon interactions and therefore indicates that uncorrelated double-quarkonia would dominate relative to correlated production in $\mathrm{Pb}+\mathrm{Pb}$ collisions. The inclusion of the third term also suggests that DPS may be significantly enhanced in $\mathrm{Pb}+\mathrm{Pb}$ collisions as compared to $p+p$ collisions, potentially leading to a nuclear modification factor of double quarkonia much greater than unity. This is tempered by the suppression of quarkonia in heavy-ion collisions, as described in Sec. 1.5, which would reduce double-quarkonia yields. Neither of these possibilies have yet been tested experimentally, as there have been no measurements of double quarkonia in collisions of heavy ions. This thesis will serve as a first measurement of simultaneous $\Upsilon+J/\psi$ production in $\mathrm{Pb}+\mathrm{Pb}$ collisions.

Chapter 2

Experimental facilities

2.1 The LHC at CERN

The Large Hadron Collider (LHC), operated by the European Center for Nuclear Research (CERN), is the world's largest particle accelerator. Located on the border of France and Switzerland and buried undergrand at an average depth of 100 m, it extends into both countries with its 27 km circumference. Figure 2.1 shows an aerial photo of the LHC and surrounding countryside.

The LHC is a type of accelerator known as a Synchrotron, which directs charged particles around a circular ring while accelerating them to higher energy. It is capable of colliding both protons and also heavy ions such as lead at greater energies than any other collider, in great quantities. The LHC has achieved center-of-mass collision energies of $\sqrt{s} = 13.6$ TeV for $p+p$ collisions with an integrated luminosity of 63.7 fb^{-1}, and $\sqrt{s_{NN}} = 5.02$ TeV for $\mathrm{Pb}+\mathrm{Pb}$ collisions with an integrated luminosity of 1.6 nb^{-1}. These quantities will be discussed further below in this section.

Operation of the LHC begins with the particle source, most commonly protons or lead ions. Protons are ionized from a bottle of hydrogen gas, while lead ions are extracted from isotropically pure solid lead that is vaporized and ionized. See Fig. 2.2 for photos of the ion sources. The particles are then sent through the CERN accelerator complex, a series of sequentially larger accelerators that boost

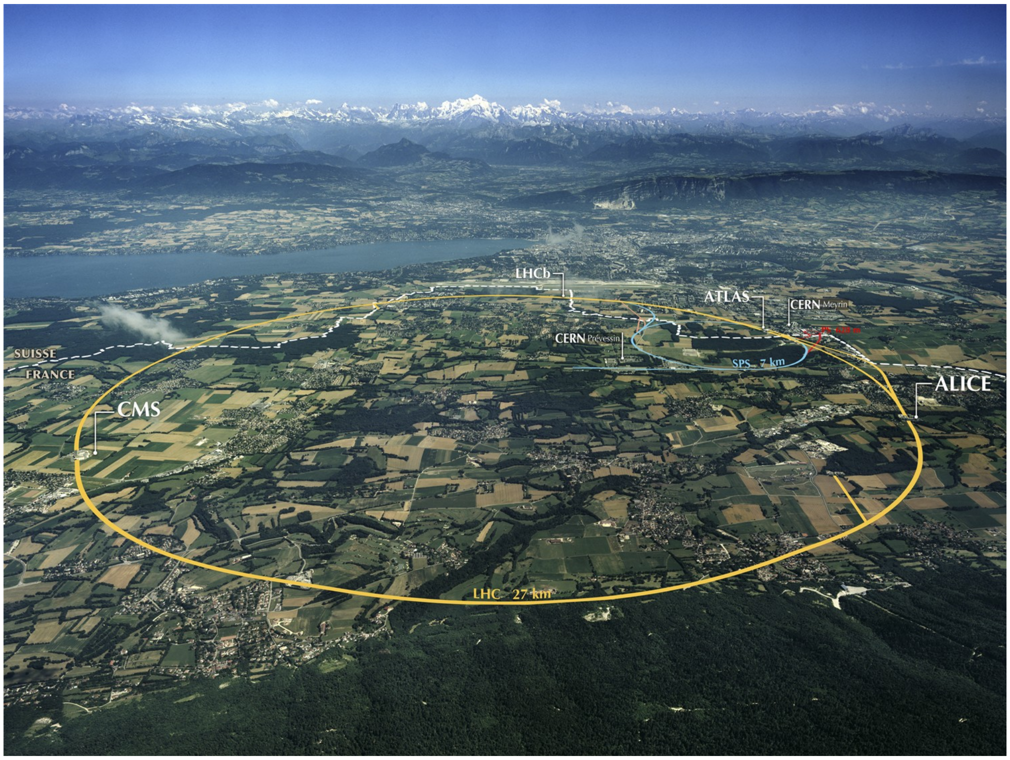

Figure 2.1. An aerial photo of the location where the LHC is buried [12]. The LHC ring is drawn in yellow, and smaller accelerators in the complex are in blue and red. The dashed white line indicates the border between France and Switzerland. Also labeled are the two main CERN laboratory sites, as well as the sites for the four main experiments.

the particles to higher and higher energies. A schematic of the accelerator complex is shown in Fig. 2.3.

The protons are directed through

- LINAC2, a linear accelerator that accelerates them to 50 MeV;
- the Proton Synchrotron Booster (PSB), which accelerates the protons to 1.4 GeV;
- the Proton Synchrotron (PS), which accelerates them to an energy of 26 GeV;
- the Super Proton Synchrotron (SPS), which accelerates to 450 GeV;
- the LHC, which accelerates the protons to a maximum of 6.5 TeV, or lower if desired.

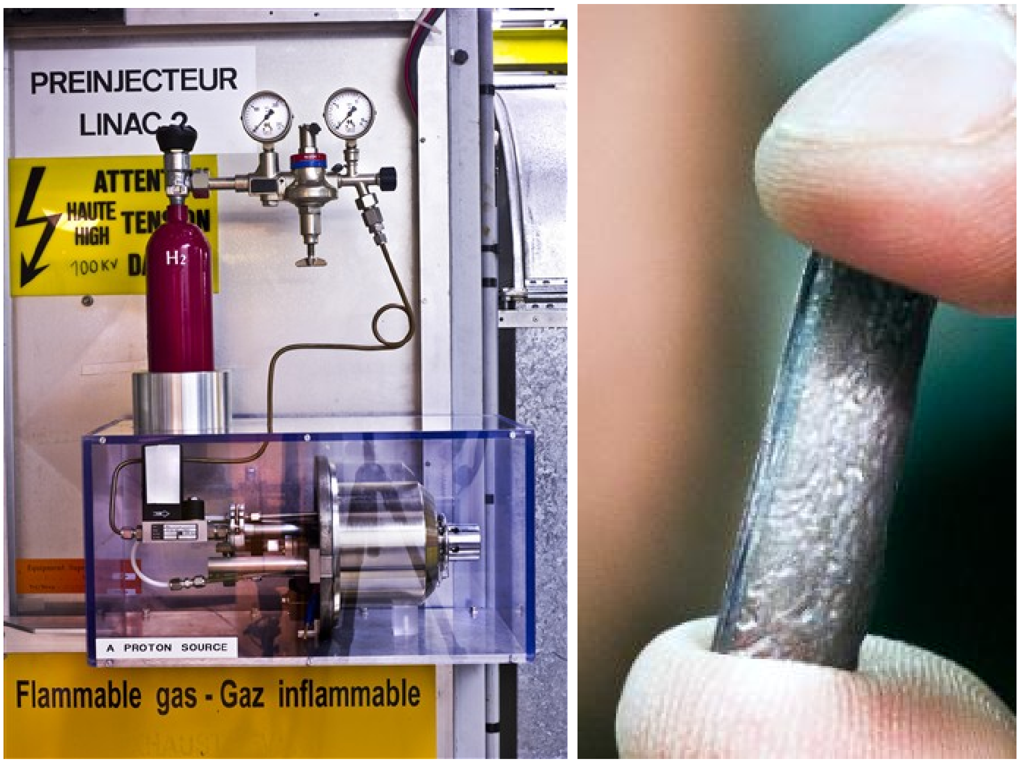
PREINJECTEUR
LINAC 2
HAUTE
HIGH
100 KV
H2
A PROTON SOURCE
Flammable gas - Gaz inflammable

Figure 2.2. Left: Proton source for the LHC [13]. The hydrogen bottle has a capacity of 750 ml, enough to supply the LHC for 200,000 years [14]. Right: Block of isotropically pure lead, used as a source of lead ions in the LHC [15]. One block is 2 cm long and 500 mg. The LHC consumes about 2 mg of lead per hour to produce lead ion beams [16].

Lead ions follow a similar sequence through

- LINAC3, which accelerates them to 4.2 MeV per nucleon;
- the Low Energy Ion Ring (LEIR), which further accelerates the lead ions to 72 MeV per nucleon;
- the Proton Synchrotron (PS), which accelerates them to an energy of 5.9 GeV per nucleon;
- the Super Proton Synchrotron (SPS), which accelerates to 177 GeV per nucleon;
- the LHC, which accelerates the lead ions to a maximum of 2.51 TeV per nucleon, or lower if desired.

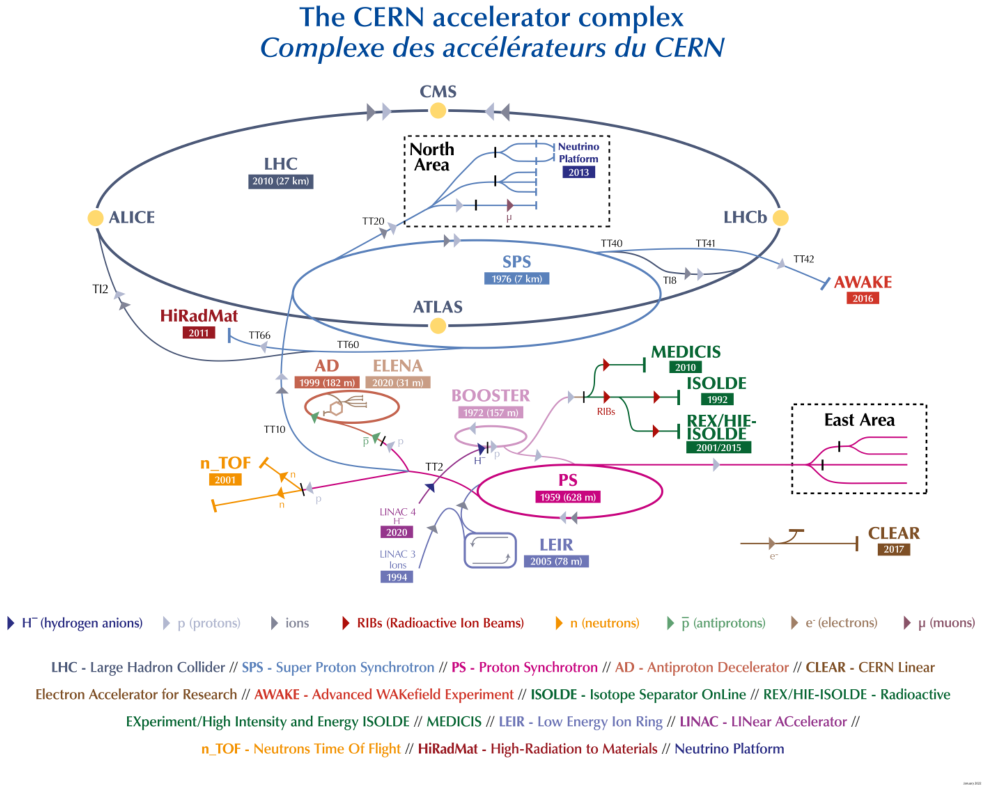
The CERN accelerator complex
Complexe des accélérateurs du CERN
CMS
North Area
Neutrino Platform
2013
LHC
2010 (27 km)
ALICE
LHCb
TT20
TT40
TT41
TT42
TI8
AWAKE
2016
SPS
1976 (7 km)
TI2
HiRadMat
2011
TT66
ATLAS
TT60
AD
1999 (182 m)
ELENA
2020 (31 m)
BOOSTER
1972 (157 m)
MEDICIS
2010
ISOLDE
1992
RIBs
REX/HIE-ISOLDE
2001/2015
East Area
TT10
n_TOF
2001
TT2
PS
1959 (628 m)
LINAC 4
2020
LINAC 3
Ions
1994
LEIR
2005 (78 m)
CLEAR
2017
H⁻ (hydrogen anions)
p (protons)
ions
RIBs (Radioactive Ion Beams)
n (neutrons)
p̄ (antiprotons)
e⁻ (electrons)
μ (muons)
LHC - Large Hadron Collider // SPS - Super Proton Synchrotron // PS - Proton Synchrotron // AD - Antiproton Decelerator // CLEAR - CERN Linear Electron Accelerator for Research // AWAKE - Advanced WAKefield Experiment // ISOLDE - Isotope Separator OnLine // REX/HIE-ISOLDE - Radioactive EXperiment/High Intensity and Energy ISOLDE // MEDICIS // LEIR - Low Energy Ion Ring // LINAC - LINear ACcelerator // n_TOF - Neutrons Time Of Flight // HiRadMat - High-Radiation to Materials // Neutrino Platform

Figure 2.3. A schematic of the CERN accelerator complex [17]. The labels on the individual accelerators show their year of first operation and their length or circumference in meters. The key accelerators used for producing heavy-ion collisions are LINAC3, the LEIR, the PS, the SPS, and LHC.

These numbers are for Run 2 of the LHC, which took place from 2015 to 2018. The accelerator complex has gone through numerous upgrades over time, most recently during Long Shutdown 2 between 2018 and 2022. For instance, LINAC2 was replaced in 2020 with the new LINAC4 (as seen in Fig. 2.3), which boosts protons to 160 MeV prior to injection to the PSB, and the maximum proton energy in the LHC has risen to 6.8 TeV. This and many other upgrades take effect in Run 3 of the LHC, which began in 2022.

Lead ions have a lower maximum energy than protons due to their charge-to-mass ratio. The LHC uses ^{208}Pb, with 82 positively-charged protons and 126 neutrally-charged neutrons. Since both nucleons have similar mass but only protons interact with magnetic fields, this means that the lead ions will only experience approximately $82/208 \approx 40\%$ of the acceleration that a proton would. With less acceleration to keep them bent in a circular path, the lead ions cannot be raised to as high an energy as protons. In general, the center-of-mass collision energy per nucleon pair $\sqrt{s_{NN}}$ in a heavy ion collision compared to the collision energy $\sqrt{s}$ of a $p+p$ collision with the same LHC magnetic field strength is

$$\sqrt{s_{NN}} = \sqrt{s}\sqrt{\frac{Z_1 Z_2}{A_1 A_2}}, \tag{2.1}$$

where Z_1 and Z_2 are the number of protons in each nucleus and A_1 and A_2 are the total number of nucleons (protons + neutrons) in each nucleus. During Run 2 the $p+p$ collision energy of the LHC was $\sqrt{s} = 13$ TeV, so its maximum collision energy for Pb+Pb would have been (13 TeV) $\cdot$ 82/208 = 5.12 TeV. However, it was instead decided to lower the collision energy to match the previous $p+$Pb collision energy from 2013. The LHC collision energy for $p+p$ in 2013 was $\sqrt{s} = 8$ TeV, so the corresponding energy for $p+$Pb was (8 TeV) $\cdot\sqrt{82/208} = 5.02$ TeV. Therefore, the collision energy for Pb+Pb collisions during Run 2 in 2018 was also 5.02 TeV.

The LHC itself consists two parallel beam pipes that form the 27 km ring. Around this ring are located 1,232 superconducting dipole magnets, each 15 m long and weighing 35 tons, which produce strong magnetic fields of up to 8.3 T to bend charged particles around the ring. The nominal field strength of 8.3 T corresponds a beam energy of 7 TeV which the LHC was designed to reach, though it has not yet attained this energy during operation as of this writing. Photos of a dipole magnet are shown in Figs. 2.4 and 2.5, taken while I was at CERN in 2018. An additional 474 quadrupole magnets of similar size are used to focus the charged particles into tight beams. The beams are accelerated by 16 radio-frequency (RF) cavities, which over a time of approximately 20 minutes gradually ramp up the beams from their injection energy coming from the SPS to their final maximum energy. The beams are not uniform, but rather divided into pulses or "bunches". For proton beams, these bunches consist of about 10^{11} protons each, while for lead ion beams the bunches contain about 10^8 lead ions. At interaction points where the opposing beams cross paths, pairs of bunches from the two beams cross every 25 ns.

ROCLA
ROBOTRUCK
FW
CERN
1241
w.cern.ch
Accel

Figure 2.4. Photo of UC Davis graduate students and LHC dipole magnet (blue cylinder) at the magnet test facility at CERN in 2018. From left to right: Ota Kukral, Santona Tuli, Graham Waegel, and Jared Jay.

There are four interaction points around the LHC ring where the beams cross to produce collisions. These locations house detectors for the four major collaborations at CERN: the Compact Muon Solenoid (CMS) experiment, A Toroidal LHC ApparatuS (ATLAS), A Large Ion Collider Experiment (ALICE), the Large Hadron Collider beauty (LHCb) experiment. This thesis uses data gathered by the CMS experiment in 2018. The CMS detector will be described in further detail below in Sec. 2.2.

The ability of the accelerator to produce particle interactions is characterized by the quantity $\mathcal{L}$, called luminosity [58]. This quantity is defined as the proportion between the rate of collisions dN/dt (written as dR/dt in Ref. [58]) and the cross section σ of the interaction,

$$\frac{dN}{dt} = \mathcal{L} \cdot \sigma, \tag{2.2}$$

which therefore gives luminosity the units of $\mathrm{cm}^{-2}\mathrm{s}^{-1}$. An especially useful quantity

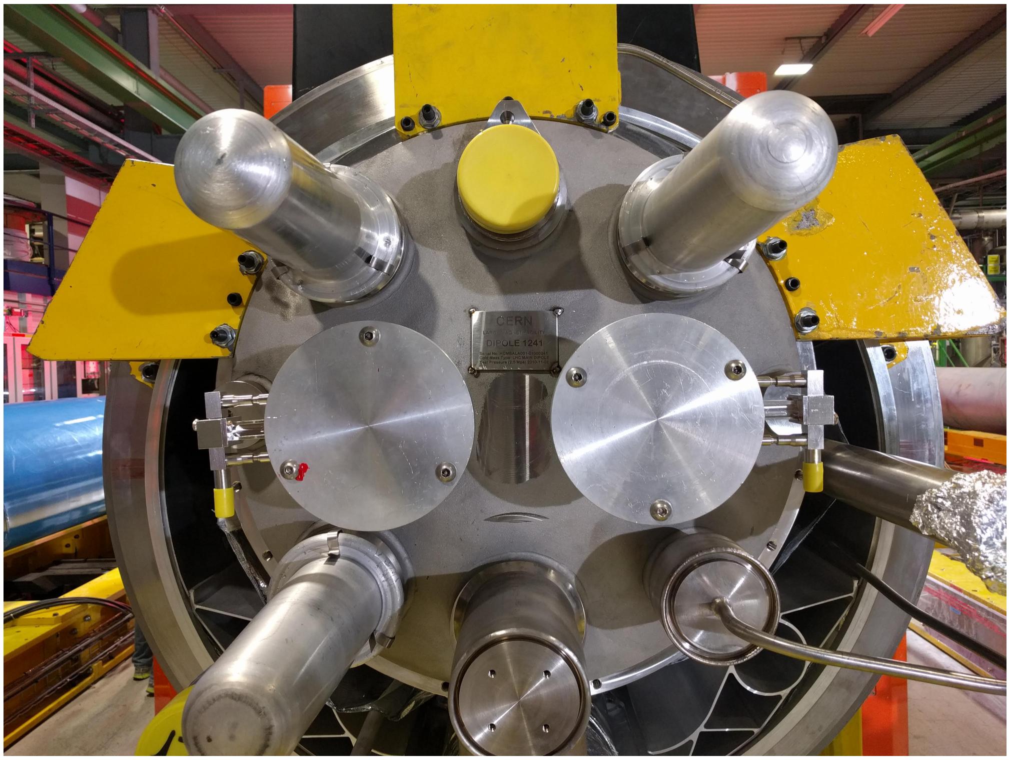

Figure 2.5. Photo of LHC dipole magnet at the magnet test facility at CERN in 2018, viewed from one end. The two capped pipes in the center are the parallel beam pipes through which the particles travel.

for characterizing datasets is the integrated luminosity $\mathcal{L}_{\text{int}}$, defined as the integral of luminosity over time

$$\mathcal{L}_{\text{int}} = \int_{t_1}^{t_2} \mathcal{L}\left(t\right) dt, \tag{2.3}$$

where the interval of integration is over the times at which collision data is taken. The integrated luminosity is typically expressed in units of nb^{-1}, where the "barn" is defined as

$$1\text{b} = 10^{-24}\text{cm}^2. \tag{2.4}$$

This integrated quantity can be used to calculate the total number of occurances of a particular interaction. For instance, the total number of $p+p$ collisions N in a dataset would be

$$N_{pp} = \mathcal{L}_{\text{int}} \cdot \sigma_{pp}^{\text{inel}}, \tag{2.5}$$

where $\sigma_{pp}^{\text{inel}}$ is the total inelastic $p+p$ cross section. Note that not every proton in a bunch crossing collides; the protons are so small relative to the beam width that only a small fraction interact, and the majority pass through unaffected.

Along with the integrated luminosity, another important characteristic of datasets collected by the LHC is the collision energy. For $p+p$ collisions this is denoted by $\sqrt{s}$, the center-of-mass collision energy, while for $\mathrm{Pb}+\mathrm{Pb}$ collisions it is denoted as $\sqrt{s_{NN}}$, the center-of-mass collision energy per nucleon-nucleon interaction.

The dataset analyzed in this thesis is of Pb+Pb collisions at $\sqrt{s_{NN}} = 5.02$ TeV, and has an integrated luminosity of 1.6 nb^{-1}. Using a glauber model to estimate the $\mathrm{Pb}+\mathrm{Pb}$ hadronic cross section as $\sigma_{\mathrm{PbPb}} = 7$ b, we can then calculate

$$N_{\mathrm{PbPb}} = \mathcal{L}_{\mathrm{int}} \cdot \sigma_{\mathrm{PbPb}} = 1.6\mathrm{nb}^{-1} \cdot 7\mathrm{b} = 1.1 \times 10^{10}. \tag{2.6}$$

The total number of $\mathrm{Pb}+\mathrm{Pb}$ collisions in this dataset is approximately 1.1×10^{10}.

2.2 The CMS detector

The Compact Muon Solenoid (CMS) detector is one of the detectors operated at CERN, located at Point 5 of the LHC near Cessy, France, in a cavern 100 m underground. A photograph of the detector is shown in Fig. 2.6. It is a large general-purpose detector, 28.7 m long and 15 m tall and with a mass of 14,000 metric tons. The name of the detector comes from three sources: it is very dense and compact, despite its size; it is designed to measure muons with great precision; and it features the most powerful solenoid magnet for its size ever made.

The CMS detector is built in a cylindrical shape, with many components layered inside each other to measure different aspects of the collisions that occur at the center. Figure 2.7 shows a cutaway diagram of the detector and its various components, and Fig. 2.8 illustrates paths that different particles could take through a cross section of the detector. Starting from the collision point at the center of the detector (left side of the Fig. 2.8), the particles first pass through the inner tracker, which records tracks of charged particles positions as they pass through. Next they reach the electromagnetic calorimeter (ECAL), where the electron (red line) and photon (dashed blue line) stop and produce showers, which can be detected by the calorimeter to measure their energy. The hadron (green line) keeps going to

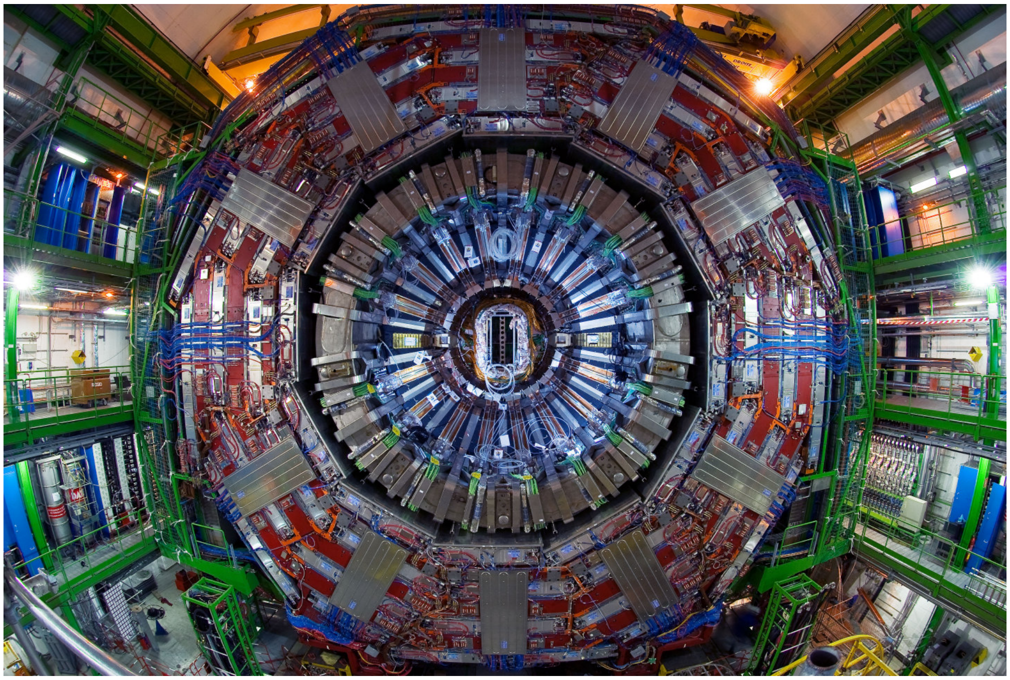

Figure 2.6. Photo of a cross section of the CMS detector [18].

the hadronic calorimeter (HCAL), where it similarly is stopped and produces a shower. Finally, the muon (light blue line) passes through all these components. The curvature inverts after passing through the solenoid, as the direction of the magnetic field is reversed. Muons are the only charged particles to reach and pass through the muon detectors. Neutrinos (not pictured) also pass through the entire detector.

The following sections will introduce the coordinate system commonly used for measurements with the CMS detector, and further describe the components of the detector. A complete description of the CMS detector can be found in Ref. [22].

2.2.1 Coordinate system

Due to the cylindrical geometry of the CMS detector, it naturally follows that cylindrical coordinates are the most convenient method of representing spatial positions of particles, tracks, or other objects in the detector. These cylindrical coordinates are the transverse distance r from the beam line, the azimuthal angle ϕ, and the distance z from the interaction point parallel to the beam axis.

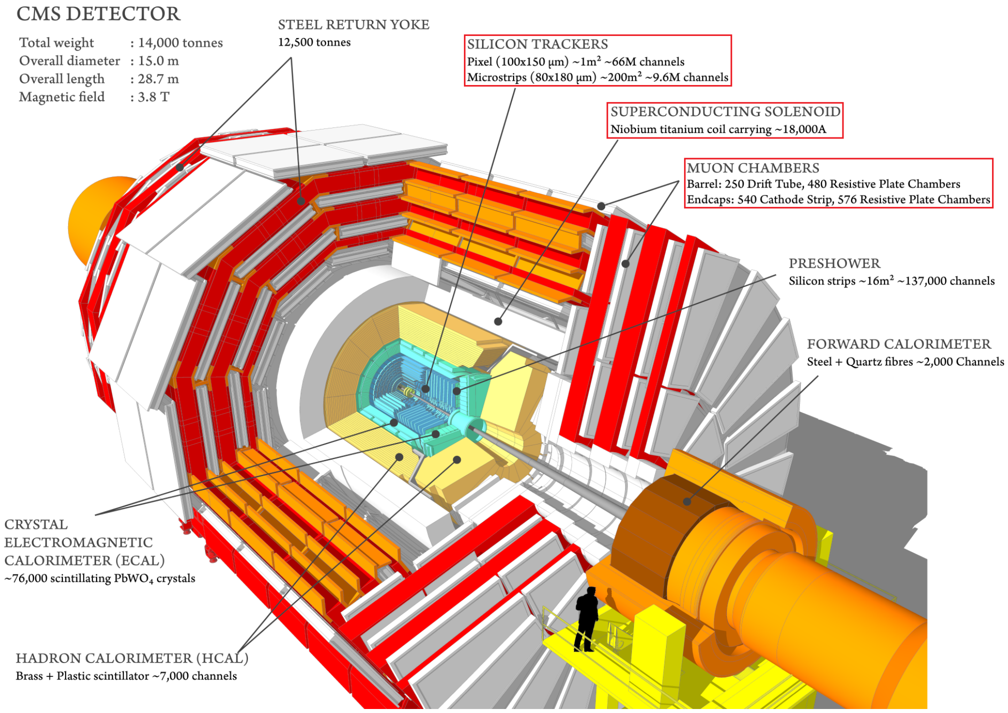
CMS DETECTOR
Total weight : 14,000 tonnes
Overall diameter : 15.0 m
Overall length : 28.7 m
Magnetic field : 3.8 T
STEEL RETURN YOKE
12,500 tonnes
SILICON TRACKERS
Pixel (100x150 μm) ~1m² ~66M channels
Microstrips (80x180 μm) ~200m² ~9.6M channels
SUPERCONDUCTING SOLENOID
Niobium titanium coil carrying ~18,000A
MUON CHAMBERS
Barrel: 250 Drift Tube, 480 Resistive Plate Chambers
Endcaps: 540 Cathode Strip, 576 Resistive Plate Chambers
PRESHOWER
Silicon strips ~16m² ~137,000 channels
FORWARD CALORIMETER
Steel + Quartz fibres ~2,000 Channels
CRYSTAL ELECTROMAGNETIC CALORIMETER (ECAL)
~76,000 scintillating PbWO₄ crystals
HADRON CALORIMETER (HCAL)
Brass + Plastic scintillator ~7,000 channels

Figure 2.7. Diagram of the CMS detector [19], with a cutaway to show the internal components. Key components for this thesis are highlighted in red boxes: the silicon trackers, muon chambers, and solenoid.

Particles in the detector are very commonly characterized by their momentum, which is represented by a different special coordinate system. The transverse momentum p_T is the component of momentum along the plane transverse to the beam axis, and ϕ is the azimuthal angle of the momentum vector in the transverse plane.

The third component, for the longitudinal direction, can be represented several ways. The most direct is θ, which is the angle from between the momentum vector and the positive direction of the beam axis. However, for relativistic particles a different representation is more convenient. Longitudinal momentum is often expressed using a quantity known as rapidity. The rapidity y of a particle is defined as

$$y = \frac{1}{2} \ln \frac{E + p_z c}{E - p_z c}, \tag{2.7}$$

where E is the total energy of the particle, p_z is the longitudinal momentum (parallel to the beam line), and c is the speed of light. For particles with small momen-

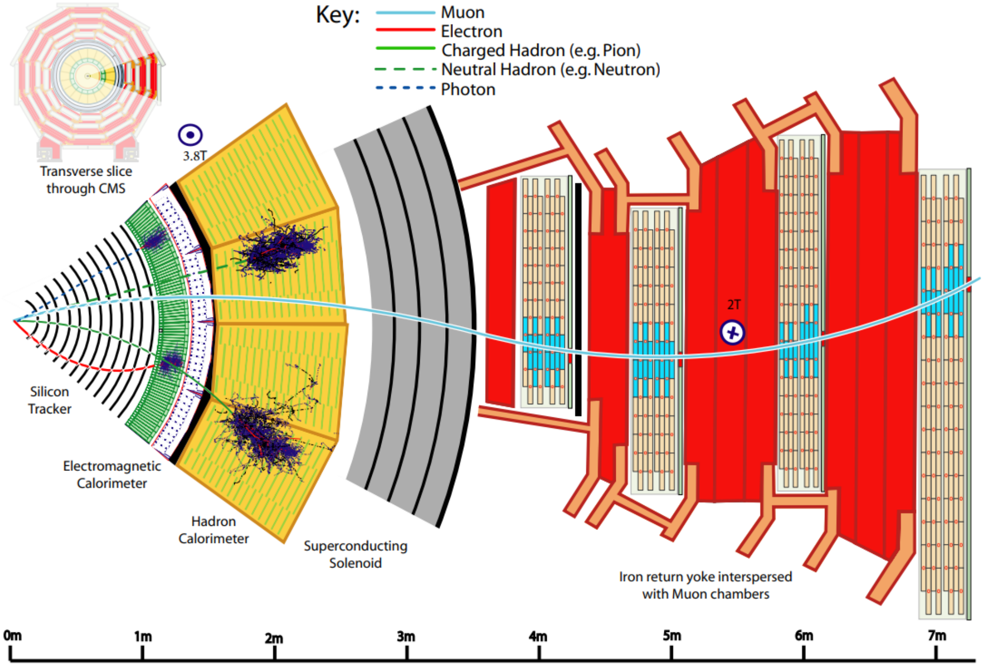
Key:
Muon
Electron
Charged Hadron (e.g. Pion)
Neutral Hadron (e.g. Neutron)
Photon
3.8T
Transverse slice through CMS
Silicon Tracker
Electromagnetic Calorimeter
Hadron Calorimeter
Superconducting Solenoid
2T
Iron return yoke interspersed with Muon chambers
0m
1m
2m
3m
4m
5m
6m
7m

Figure 2.8. Diagram of CMS detector cross section. [20]. From the inside out: all particles pass through the silicon tracker; the electron (red line) and photon (dashed blue line) stop and produce showers in the electromagnetic calorimeter; the charged and neutral hadrons (solid and dashed green lines) stops and produce showers in the hadronic calorimeter, and the muon (light blue line) travels all the way out to and through the muon detectors.

tum, the rapidity is approximately equal to β (velocity divided by c). Rapidity is a useful measure for relativistic particles because it is additive under Lorentz boosts. However, rapidity does not directly correspond to the spatial dimensions of the detector. We instead look to a similarly defined quantity η, called pseudorapidity, which is defined as

$$\eta = \frac{1}{2}\ln\frac{|\mathbf{p}| + p_z c}{|\mathbf{p}| - p_z c} = -\ln\left(\tan\left(\frac{\theta}{2}\right)\right). \tag{2.8}$$

This quantity η is directly related to the geometric angle θ, as illustrated in Fig. 2.9. Being purely geometric also makes η particularly useful for describing unidentified particles, as it does not depend on the particle's mass. Pseudorapidity and rapidity are very similar for high momentum particles, and in the limit $|\mathbf{p}| \gg mc$ they become identical. Because of this, the pseudorapidity η is the most commonly used coordinate to represent the longitudinal component of momentum for particles inside the CMS detector. In total, the conversion of the 3-momentum of a particle between Cartesian coordinates and the detector coordinates p_T, ϕ, and η is

$$\begin{aligned} p_x &= p_T \cos \phi, \\ p_y &= p_T \sin \phi, \\ p_z &= p_T \sinh \eta. \end{aligned} \tag{2.9}$$

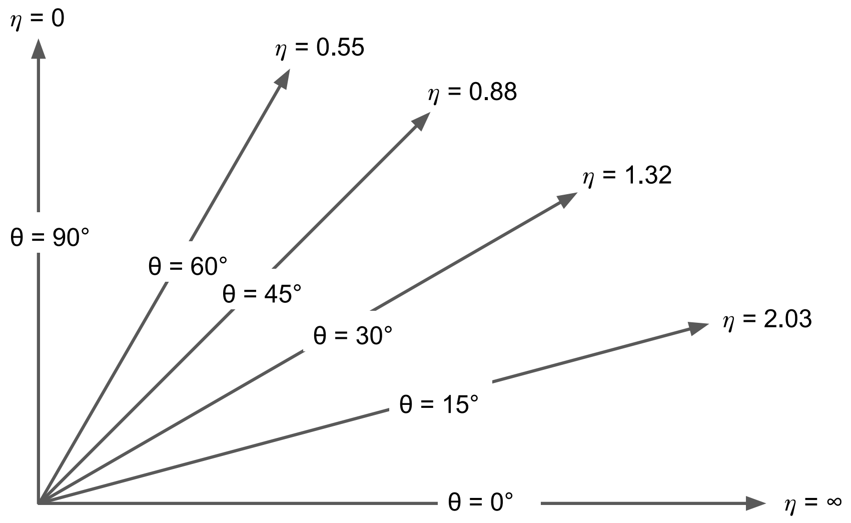

Figure 2.9. Examples of the relation between pseudorapidity η and the angle θ from the beam axis. The angle $\theta = 0$ is parallel to the beam axis, corresponding to $\eta = \infty$, and the angle $\theta = 90°$ is perpendicular to the beam axis, corresponding to $\eta = 0$.

2.2.2 Solenoid magnet

The superconducting solenoid is the central feature of the CMS detector. At 12.5 m long, an internal diameter of 6.3 m, and 12,000 tons, it is the largest and most powerful superconducting magnet ever built. It is capable of producing a magnetic field of up to 4.0 T, though typically it is operated 3.8 T. To accomplish this, the solenoid is built with 4 winding layers of niobium-titantium conductor reinforced with aluminum alloy. The magnet is cryogenically cooled to a temperature of 4.5 K for superconductivity, permitting a current of 18,500 amps through the coils. In addition to the solenoid magnet itself, The CMS detector incorporates an iron return yoke with an outer diameter of 14 m. This yoke helps maintain a strong and uniform field outside the solenoid, which aids in detection of muons in the outer region. The iron yoke itself weighs 10,000 tons, which comprises the majority of the weight of the solenoid system and the CMS detector as as whole.

The purpose of the strong magnetic field is to bend the trajectories of particles, which aids in momentum measurement, tracking, and particle identification. Charged particles traveling in a uniform magnetic field are bent in a circular path within a plane perpendicular to the field. The radius R of this curved path is

$$R = \frac{p_T}{qB} \tag{2.10}$$

where p_T is the momentum of the particle in the transverse plane, q is the charge of the particle, and B is the strength of the magnetic field. Thus, by knowing the strength of the field and the charge of the particle, and measuring the radius of the particle's curved path, the transverse momentum p_T of the particle can be determined. This measurement also relies on good tracking systems to precisely measure the particle's location along its path.

2.2.3 Silicon tracker

The silicon tracker is the innermost component of the CMS detector, located closest to the interaction point, as seen in Figs. 2.7 and 2.8. The purpose of this component is to record the precise positions of particles emitted by the collisions in 3D space. By combining multiple points recorded from a single particle, the particle's track through the detector can be reconstructed. In combination with the solenoid, which causes particles to follow curved trajectories, this allows for precise momentum measurements as described in the previous section.

The silicon detectors operate using ionization. Charged particles passing through excite electrons in the silicon, which leave a positively-charged hole behind. An electric field applied through the detector causes these electron-hole pairs to move towards the positive and negative electrodes respecively, thereby generating a small electric current. This current can be read as an electronic signal, thereby registering the passage of the charged particle.

The tracker is made of multiple layers, allowing it to record the location of a particle several times as it passes through. The three innermost layers are the silion pixel detectors, which have the greatest precision. They contain 65 million pixels in total, each with dimensions 100 μm × 150 μm. Outside these are the silicon strip detectors, beginning with four inner barrel (TIB) layers assembled in shells. These are capped by two inner endcaps (TID), each composed of three small disks. On the outside of the TIB and TID are six more layers of the outer barrel (TOB), which itself has two endcaps (TEC). See Fig 2.10 for a schematic of the silicon detector layers. The coverage of the tracking system extends over the pseudorapidity range $|\eta| < 2.5$.

Due to intense radiation in the innermost region of the detector, the tracking system and associated electronics are cooled to -20 °C. This minimizes disorder in the silicon and prevents spreading of any damage caused by the radiation.

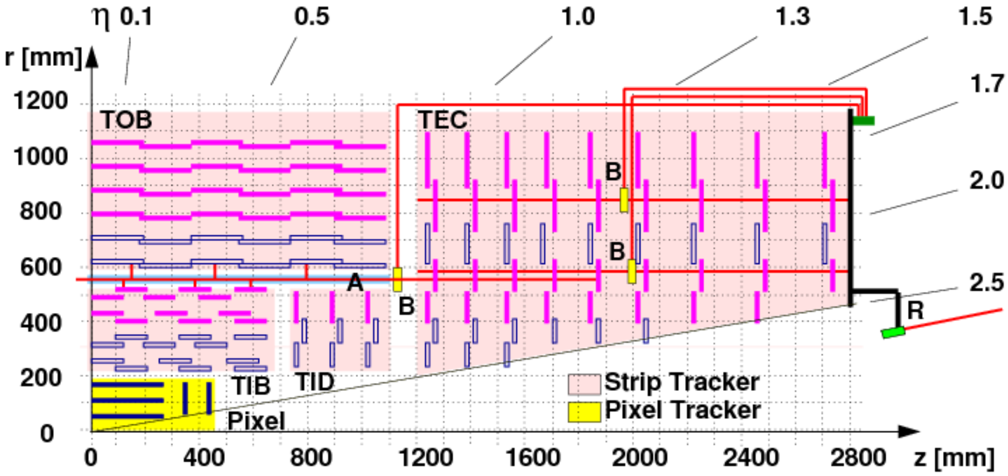

Figure 2.10. Schematic of one quadrant of the CMS silicon tracker system [21]. The lower left corner of the figure is the collision point at the center of the detector. The x axis represents longitudinal distance along the beamline, and the y axis represents radial distance from the beam. Pseudorapidity values are displayed at the top and right of the figure. The pixel tracker and all parts of the strip tracker are seen: the inner barrel (TIB), the inner endcap (TID), the outer barrel (TOB) and the outer endcap (TEC). Components marked A and B are alignment tubes and beam splitters for a laser alignment system used to calibrate the position of the detector.

2.2.4 Calorimeters

In addition to tracking, it is also important that the CMS detector is able to measure the energy of particles produced in collisions. To do this, the detector contains two different calorimeters: the electromagnetic calorimeter (ECAL) for measuring electrons and photons, and the hadronic calorimeter (HCAL) for measuring hadrons. These calorimeters must be very dense in order to stop particles completely while being compact enough to fit inside the solenoid.

The ECAL consists of lead-tungstate ($PbWO_4$) crystals with attached photodetectors. Each crystal is 230 mm long, with a cross section of 22×22 mm^2 at the front face and 26×26 mm^2 at the rear face. The crystals act as a scintillator, a material that absorbs energy from ionizing particles and emits light in response. High-energy electrons or photons that enter the crystal produce "showers" via Bremsstrahlung radiation and pair-production: the high-energy electrons undergoing Bremsstrahlung produce high-energy photons, which then pair produce electrons and positron, which radiate further, and so on. Lead tungstate was chosen for its high Z in order to maximize cross sections for the showering processes, and also for its fast scintillation rate in order to keep up with the LHC's very fast collision rate. The photodetectors serve to measure the photons resulting from the showers and therefore the energy from the original particle. Figure 2.11 shows a $PbWO_4$ crystal with attached photodetector (left), and a module of 1700 of these crystals (right).

The ECAL is made of a barrel section and two endcaps. The barrel covers the pseudorapidity range $|\eta| < 1.479$, using 61,200 $PbWO_4$ crystals that weigh a total of 67 tons. The endcaps cover the range $1.479 < |\eta| < 3.0$ using a total of 7324 crystals, weighing 24 tons.

The HCAL lies between the ECAL and the solenoid. The purpose of this calorimeter is to measure the energy of hadrons, which requires stopping them completely before they penetrate all the way through. With the limited space inside the solenoid, this means the HCAL must be made from a very dense, high-

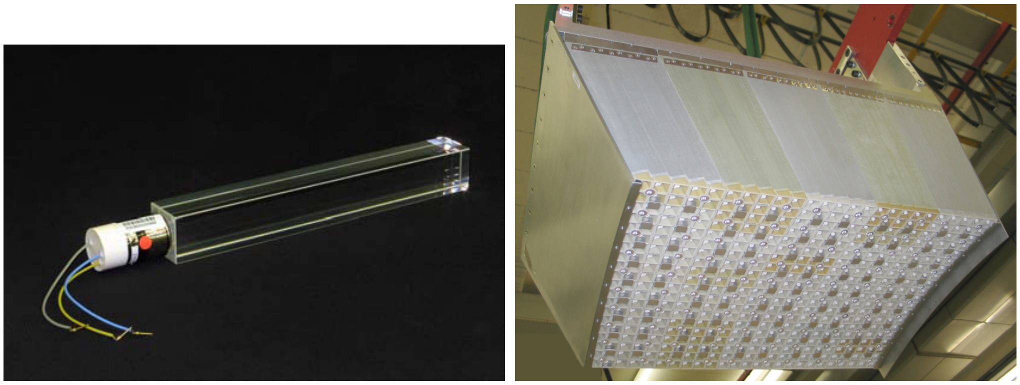

Figure 2.11. Left: Photo of polished $PbWO_4$ crystal with attached photodetector. Right: ECAL module containing 1700 crystals [22].

A material to maximize nuclear interactions with outgoing hadrons. The material selected for this was brass, an alloy of 70% copper (average $A = 63.6$) and 30% zinc (average $A = 65.5$). A large portion of this brass was collected from over a million World War 2 cartridge shells from the Russian navy. Layers of this brass absorber are alternated with layers of plastic scintillator. Hadrons interact with the nuclei in the brass absorber to create showers of secondary particles, which then produce light in the scintillator. The light is collected by wavelength-shifting fibers and brought to photodiodes for signal processing.

A schematic of the HCAL is shown in Fig. 2.12. This calorimeter is divided into four major parts. First, the barrel (HB) is made from 36 azimuthal wedges of brass absorber plates and scintillator, weighing 26 tons each, and covers the pseudorapidity range $|\eta| < 1.3$. The HB alone cannot fully stop all hadrons in the range it covers, so several more layers are placed outside the solenoid to form the outer calorimeter (HO). Two endcaps (HE), made of another 36 wedges, cover the range $1.3 < |\eta| < 3.0$. Finally, two forward calorimeters (HF) extend the pseudorapidity range to $|\eta| < 5.2$.

The HF calorimeters are designed differently than the other parts of the HCAL. Their location at very large pseudorapidity experiences much higher particle flux, so this calorimeter must be more resistant to radiation. Therefore, it is instead built from grooved steel absorber plates, with quartz fibers running through the grooves to carry the signal for readout. The HF calorimeters are used for the minimum-bias trigger for heavy-ion collisions, and to define the centrality of the collisions.

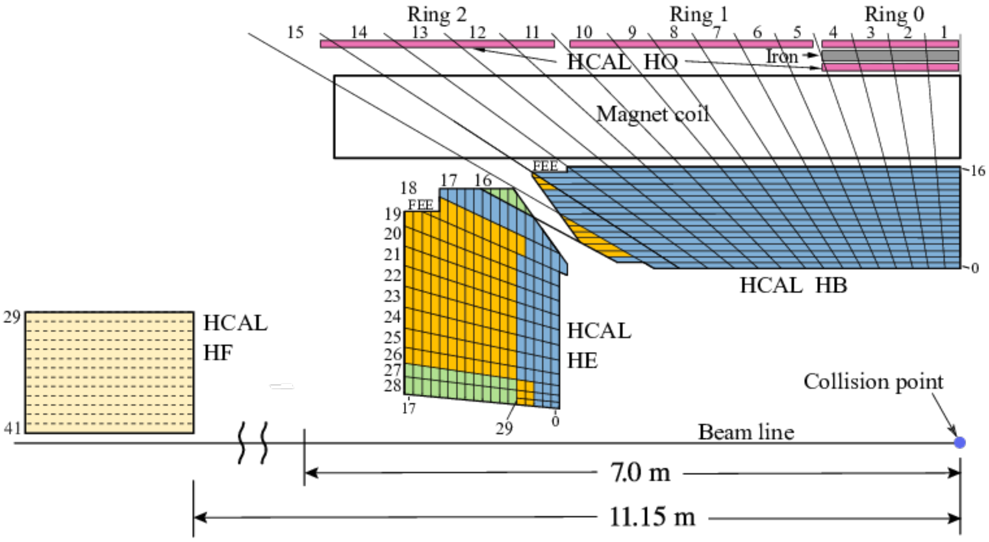

Ring 2
Ring 1
Ring 0
15
14
13
12
11
10
9
8
7
6
5
4
3
2
1
HCAL HO
Iron
Magnet coil
FEE
16
0
HCAL HB
18
17
16
FEE
19
20
21
22
23
24
25
26
27
28
17
29
0
HCAL HE
29
41
HCAL HF
Collision point
Beam line
7.0 m
11.15 m

Figure 2.12. Schematic of one quadrant of the CMS hadronic calorimeter [23]. The blue dot in the lower right is the collision point at the center of the detector. The x axis represents longitudinal distance along the beam line, and the y axis represents radial distance from the beam (not labeled). All four parts of the HCAL are shown: the barrel (HB), the the endcap (HE), the forward calorimeter (HF) located farther down the beam line, and the outer calorimeter (HO) located outside the solenoid magnet. The HB is located between the radii of 1.78 m and 2.88 m around the beam line.

2.2.5 Muon system

The muon detectors are the outermost components of the CMS detector and the only components other than the yoke that lie outside the solenoid. These detectors are solely for the detection of muons, which is ensured because muons are the only charged particle that can reach them. All other particles are stopped in the calorimeters: electrons and photons are stopped in the ECAL, while hadrons are stopped in the HCAL. Muons are similar to electrons, but with 200 times the mass they pass through the ECAL and all other components with little energy loss, allowing them to reach all the way out to the muon chambers.

There are three types of muon detectors arranged in different regions. The barrel region contains 250 drift tube (DT) chambers that cover the pseudorapidity range $|\eta| < 1.2$, and the endcaps contain 540 cathode strip chambers (CSCs) covering the range $0.9 < |\eta| < 2.4$. In addition, 610 resistive plate chambers (RPCs) are located in both the barrel and endcap regions, interspersed between DT and CSC layers respectively, covering a total pseudorapidity range of $|\eta| < 1.6$. The layout of the muon system is illustrated in Fig. 2.13.

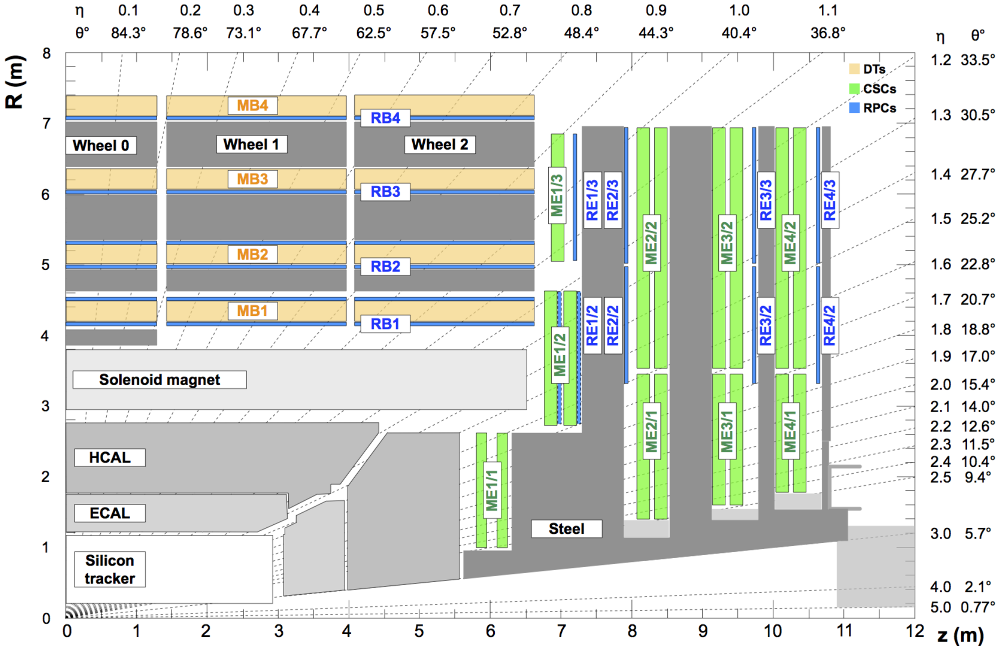
η θ°
0.1 84.3°
0.2 78.6°
0.3 73.1°
0.4 67.7°
0.5 62.5°
0.6 57.5°
0.7 52.8°
0.8 48.4°
0.9 44.3°
1.0 40.4°
1.1 36.8°
η θ°
1.2 33.5°
1.3 30.5°
1.4 27.7°
1.5 25.2°
1.6 22.8°
1.7 20.7°
1.8 18.8°
1.9 17.0°
2.0 15.4°
2.1 14.0°
2.2 12.6°
2.3 11.5°
2.4 10.4°
2.5 9.4°
3.0 5.7°
4.0 2.1°
5.0 0.77°
R (m)
z (m)
0
1
2
3
4
5
6
7
8
9
10
11
12
DTs
CSCs
RPCs
MB4
MB3
MB2
MB1
RB4
RB3
RB2
RB1
Wheel 0
Wheel 1
Wheel 2
ME1/3
ME1/2
ME1/1
RE1/3
RE2/3
RE1/2
RE2/2
ME2/2
ME2/1
ME3/2
ME3/1
RE3/3
RE3/2
ME4/2
ME4/1
RE4/3
RE4/2
Solenoid magnet
HCAL
ECAL
Silicon tracker
Steel

Figure 2.13. Diagram of the muon system layout in one quadrant of the CMS detector [24] with DTs are highlighted in yellow, CSCs in green, and RPCs in blue. The interaction point where collisions occur is in the lower left corner of the figure. The x axis represents longitudianal distance along the beamline, and the y axis represents radial distance from the beam. The angle θ from the beam and equivalent η are displayed at the top and right of the figure.

Drift tubes are rectangular tubes of CO_2 and Ar gas, with a straight wire running through it that acts as an anode. When a muon passes through the tube, it ionizes the gas and creates free electrons that drift toward the positively charged anode wire due to the electric field it creates. Upon reaching the wire, the electrons produce a readable electric signal. Because the drift velocity is constant, the signal from the electrons reaching the wire can be timed to determine the location where the muon crossed the chamber. See Fig. 2.14 for an illustration of a DT. Each DT chamber consists of two or three superlayers, each with four layers of DTs. The middle superlayer is oriented to measure the position coordinate of muons along the beam axis and the other superlayers measure the coordinate perpendicular to the beam axis. Combined, the DT chamber can record a three-dimensional track of passing muons. Figure 2.15 shows a diagram of these layers. Four concentric rings of these chambers form the four DT stations of the barrel, with 60 chambers in each of the three inner stations and 70 in the outermost station. A transverse cross section of the barrel is shown in Fig. 2.16.

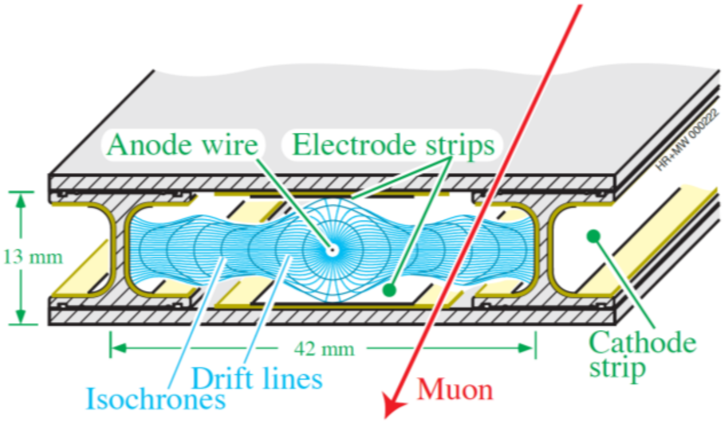
Anode wire
Electrode strips
HR-MW 000222
13 mm
42 mm
Cathode strip
Drift lines
Isochrones
Muon

Figure 2.14. Diagram of a drift tube [22], illustrating a muon passing through (red arrow) and inducing a signal.

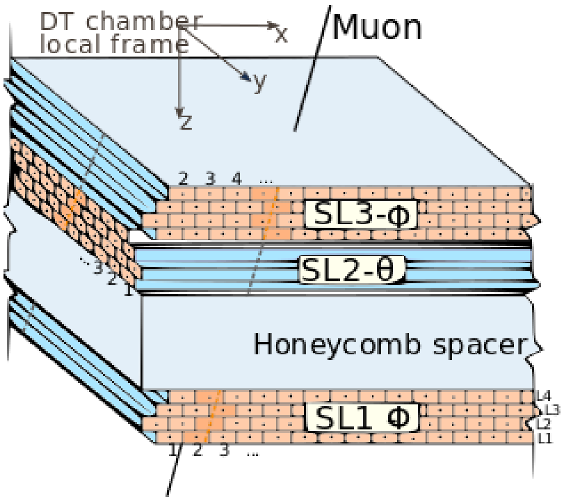
DT chamber local frame
x
y
z
Muon
2 3 4 ...
SL3-Φ
SL2-θ
... 3 2 1
Honeycomb spacer
L4
L3
L2
L1
SL1 Φ
1 2 3 ...

Figure 2.15. Diagram of a DT chamber [25]. There are three superlayers of four layers each, with the middle superlayer oriented perpendicularly to the outer two.

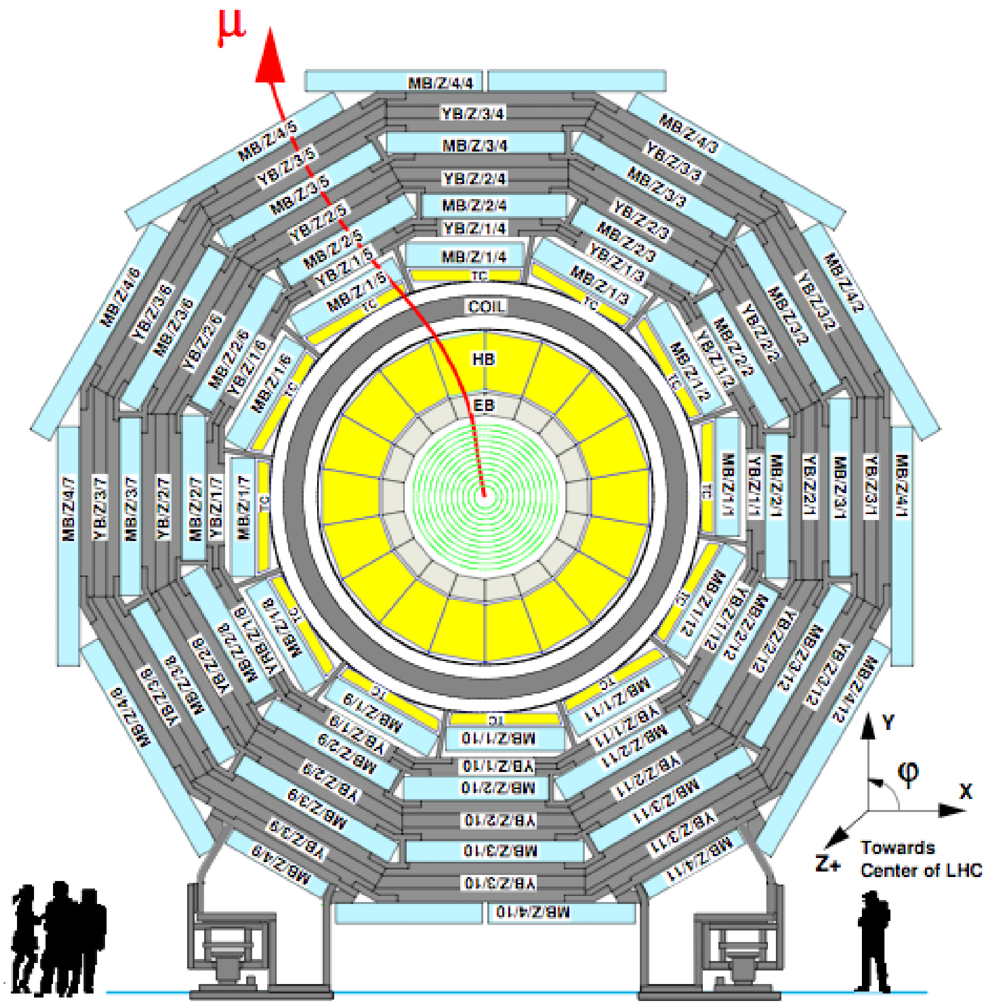
μ
MB/Z/4/4
YB/Z/3/4
MB/Z/3/4
YB/Z/2/4
MB/Z/2/4
YB/Z/1/4
MB/Z/1/4
TC
COIL
HB
EB
MB/Z/4/5
YB/Z/3/5
MB/Z/3/5
YB/Z/2/5
MB/Z/2/5
YB/Z/1/5
MB/Z/1/5
MB/Z/4/3
YB/Z/3/3
MB/Z/3/3
YB/Z/2/3
MB/Z/2/3
YB/Z/1/3
MB/Z/1/3
MB/Z/4/6
YB/Z/3/6
MB/Z/3/6
YB/Z/2/6
MB/Z/2/6
YB/Z/1/6
MB/Z/1/6
MB/Z/4/2
YB/Z/3/2
MB/Z/3/2
YB/Z/2/2
MB/Z/2/2
YB/Z/1/2
MB/Z/1/2
MB/Z/4/7
YB/Z/3/7
MB/Z/3/7
YB/Z/2/7
MB/Z/2/7
YB/Z/1/7
MB/Z/1/7
MB/Z/1/1
YB/Z/1/1
MB/Z/2/1
YB/Z/2/1
MB/Z/3/1
YB/Z/3/1
MB/Z/4/1
MB/Z/4/8
YB/Z/3/8
MB/Z/3/8
YB/Z/2/8
MB/Z/2/8
YB/Z/1/8
MB/Z/1/8
MB/Z/1/12
YB/Z/1/12
MB/Z/2/12
YB/Z/2/12
MB/Z/3/12
YB/Z/3/12
MB/Z/4/12
MB/Z/1/9
YB/Z/1/9
MB/Z/2/9
YB/Z/2/9
MB/Z/3/9
YB/Z/3/9
MB/Z/4/9
MB/Z/1/10
YB/Z/1/10
MB/Z/2/10
YB/Z/2/10
MB/Z/3/10
YB/Z/3/10
MB/Z/4/10
MB/Z/1/11
YB/Z/1/11
MB/Z/2/11
YB/Z/2/11
MB/Z/3/11
YB/Z/3/11
MB/Z/4/11
Y
φ
X
Z+
Towards
Center of LHC

Figure 2.16. Transverse cross section of the DT barrel region [22]. The four concentric DT stations are highlighted in blue.

Cathode strip chambers contain arrays of positively charged anode wires crossed with negatively charged cathode wires within a volume of gas. The gas in these chambers is a mixture of Ar, CO_2, and CF_4. When muons pass through the chamber, they ionize the gas. The free electrons travel to the anode wires, while the ionized gas atoms travel to the cathode wires, each causing an electrical signal when they arrive. Because the two types of wires are oriented perpendicularly, this provides two-dimensional coordinates to determine where the muon crossed the chamber. Each CSC has 7 trapezoidal panels with 6 gas-filled gaps between them, as shown in Fig. 2.17. Each station consists of either 36 or 72 of these chambers that form a complete azimuthal ring around the beamline. Figure 2.18 shows a photo of a complete CSC endcap.

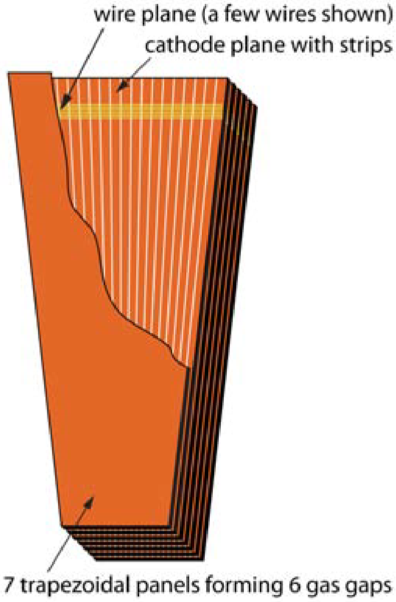
wire plane (a few wires shown)
cathode plane with strips
7 trapezoidal panels forming 6 gas gaps

Figure 2.17. Diagram of CSC [22] showing the trapezoidal panels, anode wires, and cathode strips.

Resistive plate chambers are a third type of gaseous detector. They consist of two parallel plates, one of them a positively charged anode and the other a negatively charged cathode. The plates are made of a high-resistivity plastic and are separated by a thin volume of gas. Muons passing through the chamber ionize the gas, then the free electrons travel to the anode plate and the ionized gas atoms travel to the cathode plate, leading to an electrical signal readout. A diagram of the layout of an RPC is shown in Fig. 2.19. The RPCs have coarser spatial resolution than the DTs and CSCs, but good time resolution and very fast responses on the order of a nanosecond. They are designed for these fast responses times in order to act as a basis for the muon triggers.

Similar to the inner tracker, repeated hits from muons passing through multiple layers in the muon detectors allow the track of the muon to be resconstructed. The magnetic field from the solenoid is approximately 2 T in the region of the muon detectors, which will cause the reconstructed track to bend (though in

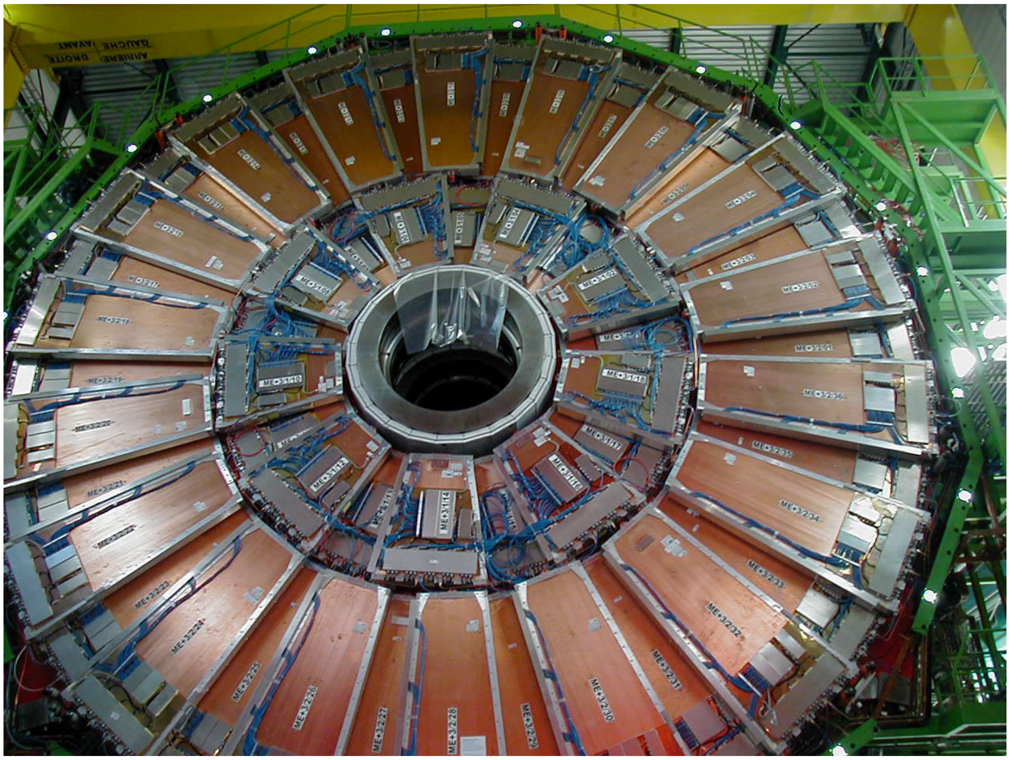

Figure 2.18. Photo of CSC endcap. [22].

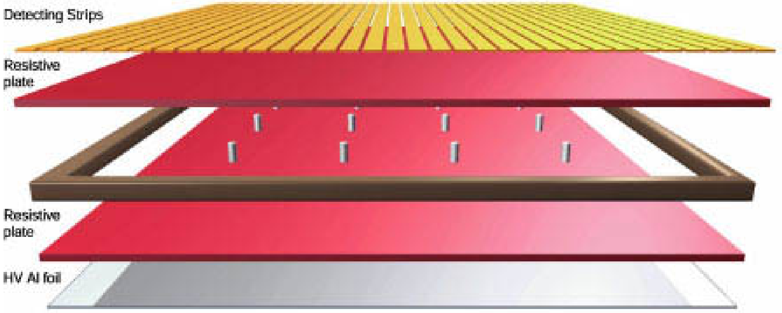

Figure 2.19. Diagram of resistive plate chamber [26].

the opposite direction as inside the solenoid, due to the direction of the field). This allows the momentum of the muon to be measured, though with worse resolution compared to that of the more precise inner tracking system. Therefore, tracks reconstructed in the muon detector are matched with tracks reconstructed in the inner tracker, combining the inner tracker's precision with the positive muon identification of the muon detectors. It is this combination of the muon system, silicon trackers, and solenoid that allows the CMS detector to measure muons with greater precision than any other experiment. For example, the measured width of the $\Upsilon(1S)$ resonance is $\sim$70 MeV, for a mass resolution of approximately 70 MeV / 9.4 GeV $\approx$ 0.7% at the Υ mass.

Figure 2.20 shows an event display of an Υ candidate that decayed to two muons. The red lines are the reconstructed muon tracks and the red wireframes represent the muon chambers that registered hits used to reconstruct the muon tracks. The yellow lines are other tracks registered by the silicon tracker in the same event and the green squares represent energy deposited in the calorimeters. This event is the first Υ candidate seen in the 2018 Pb + Pb dataset, selected by me while on-site at CERN monitoring event displays of the incoming data stream.

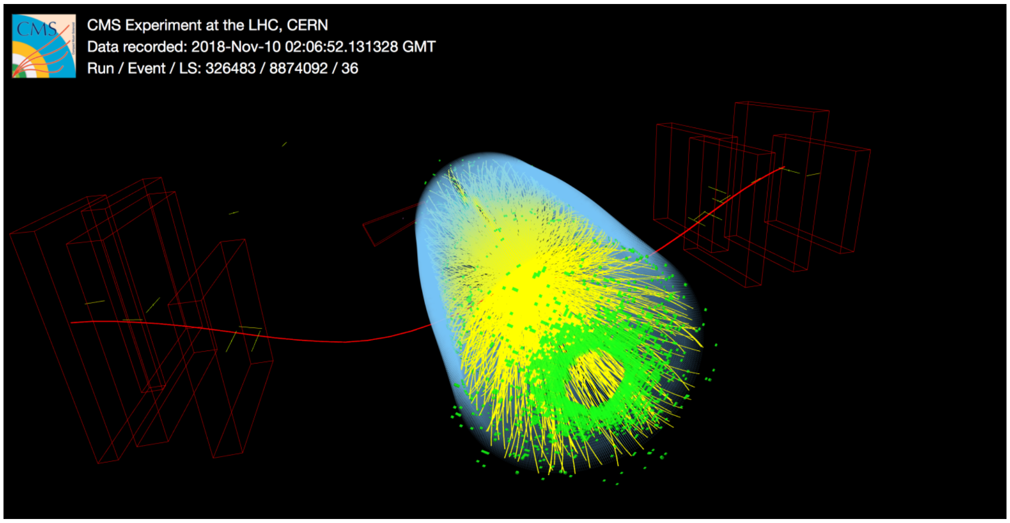
CMS
CMS Experiment at the LHC, CERN
Data recorded: 2018-Nov-10 02:06:52.131328 GMT
Run / Event / LS: 326483 / 8874092 / 36

Figure 2.20. Event display of an Υ decay candidate in the CMS detector. [27]. The red lines are the reconstructed muon tracks, and the red wireframes are the muon chambers that registered muon tracks. The yellow lines are other tracks registered by the silicon tracker in the same event, and the green squares represent energy deposits in the calorimeters. Event selected by me during 2018 Pb + Pb data taking at CERN.

2.2.6 Trigger system

The quantity of data collected by the CMS detector is far too great to store in its entirety. Raw collision data is on the order of 1 MB of digital storage per collision event, and with bunch crossings occuring at a rate of 40 Mhz the amount of storage required would quickly become untenable. Therefore, a trigger system is used to rapidly analyze incoming data and save only events of specific interest, immediately discarding the rest.

The trigger system consists of two tiers [59]. The first tier, known as the L1 trigger, is a fast hardware trigger using custom processor chips to decide within 4 μs whether to accept or reject each event. Figure 2.21 shows a diagram of the L1 trigger system. Data from the ECAL and HCAL are combined in the regional calorimeter trigger, then sent to the global calorimeter trigger and then the global trigger. For instance, the minimum-bias trigger for heavy-ions requires simultaneous energy deposits of at least 3 GeVon both sides of the HF calorimeter. Meanwhile, muon candidates are selected using tracks calculated from DT, CSC, and RPC data. The global muon trigger chooses the best 4 muons and sends them to the global trigger. Finally, the global trigger evaluates the muon candidates and calorimeter data based on a menu of algorithms or “trigger paths”. Any muons satisfying the requirements of a trigger path are forwarded to the next tier of the trigger system.

The second tier of the trigger system is the high-level trigger (HLT), run on a farm of approximately 30,000 standard computer processors as of 2018. While the L1 has access to only coarse data from the calorimeters and muon detectors, and none from the silicon tracker, the HLT runs a version of the full event reconstruction software. The HLT computes “HLT paths”, algorithms similar to the trigger paths used in the L1 trigger. HLT paths are much more complex, including sequences of reconstruction algorithms to reconstruct objects from detector data, and filters to apply selections on those objects and data. These paths become increasingly sophisticated as they progress, and are cut off at any point of failure to save processing time. Any event that passes a complete HLT path is sent for permanent storage.

Muon algorithms in the HLT are composed of two steps: level-2 (L2), which uses information from the muon detectors only, and level-3 (L3) which also combines measurements from the silicon tracker. In the L2 stage, muon tracks are reconstructed from hits in the DT and CSC segments using a Kalman filter technique [60]. Various filters are applied to the reconstructed L2 muons, most commonly on their p_T or the number muon chamber hits used for reconstruction.

The L3 stage leverages the precision of the CMS silicon tracker for improved resolution. Full reconstruction is not performed due to time and processing constraints; instead, tracks are seeded by muon candidates from the L2 stage. Simple reconstruction algorithms are run first, progressing to more complicated ones only if the initial algorithms fail to reconstruct. Energy deposits from the ECAL and HCAL are also examined in a cone around the L3 candidate to isolate the muon. After successful reconstuction, the L3 muons are then filtered according to various criteria, most commonly their p_T, their track goodness-of-fit (χ^2), or their impact parameter. Some HLT paths may require multiple reconstructed muons in a single event.

Finally, any event that passes the full trigger process, from L1 through HLT, is sent for permanent storage. Information on which trigger paths were satisfied is included for each event. The specific trigger used for this thesis will be discussed in Sec. 3.3.

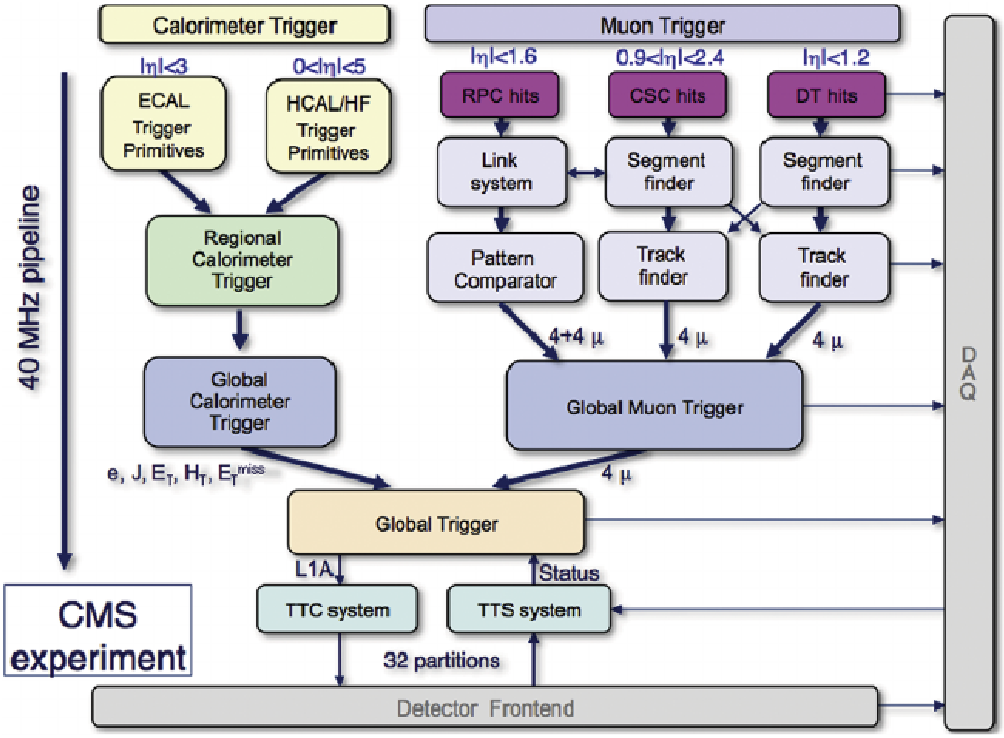
Calorimeter Trigger
Muon Trigger
$|\eta|<3$
$0<|\eta|<5$
$|\eta|<1.6$
$0.9<|\eta|<2.4$
$|\eta|<1.2$
ECAL Trigger Primitives
HCAL/HF Trigger Primitives
RPC hits
CSC hits
DT hits
Link system
Segment finder
Segment finder
Regional Calorimeter Trigger
Pattern Comparator
Track finder
Track finder
4+4 μ
4 μ
4 μ
40 MHz pipeline
Global Calorimeter Trigger
Global Muon Trigger
D A Q
e, J, E_T, H_T, E_T^{miss}
4 μ
Global Trigger
L1A
Status
CMS experiment
TTC system
TTS system
32 partitions
Detector Frontend

Figure 2.21. Diagram of the L1 trigger system of CMS. [28]. Data from the ECAL and HCAL are combined in the regional calorimeter trigger, then sent to the global calorimeter trigger and then the global trigger. The global muon trigger selects muon candidates using data from the DTs, CSCs, and RPCs. The global trigger combines the calorimeter and muon triggers and uses a menu of trigger paths to decide whether to accept or reject the event. For heavy ions, the minimum-bias trigger is based on the HF calorimeter.

Chapter 3

Data selection and simulated samples

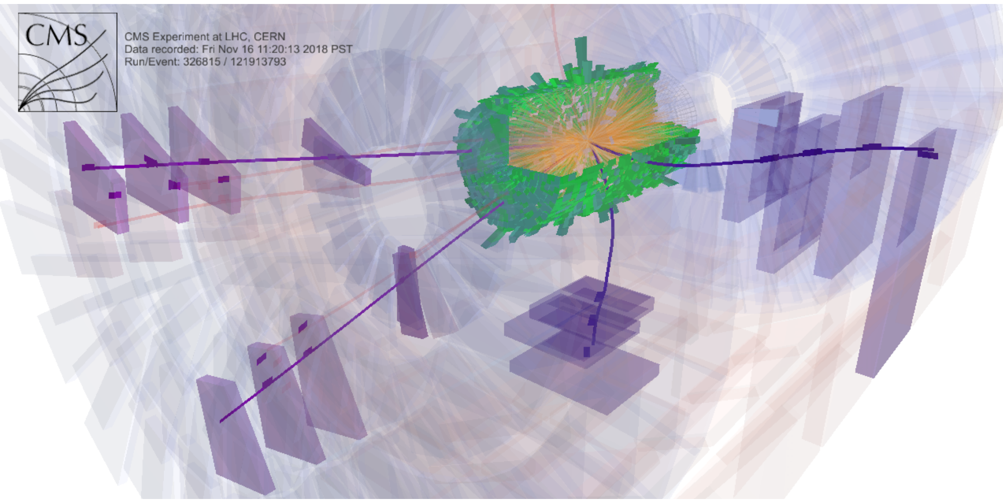
CMS
CMS Experiment at LHC, CERN
Data recorded: Fri Nov 16 11:20:13 2018 PST
Run/Event: 326815 / 121913793

Figure 3.1. Event display of an Υ+J/ψ double-quarkonia candidate. The yellow and orange lines represent tracks in the inner tracker. The green blocks represent energy deposited in the calorimeter, with a segment removed from this display for visibility. The large transparent segments are the muon detectors. The muons from the Υ candidate are highlighted in purple and the muons from the J/ψ candidate are highlighted in blue, with a more noticeable curvature due to their lower p_T. Figure produced by me using Fireworks software [29].

3.1 Dataset

This analysis uses data from Pb + Pb collisions at an energy of $\sqrt{s_{NN}} = 5.02$ TeV collected by CMS at the LHC in November and December of 2018. The quantity of data recorded corresponds to an integrated luminosity of 1.6 nb^{-1}.

Collision data at CMS is stored in multiple tiers. The first tier is named RAW, and contains the detector data and trigger results. Reconstruction algorithms then process this information to produce candidates for physics objects such as muons. This, along with a subset of RAW data, is stored in another data tier named RECO. Finally, there is the Analysis Object Data (AOD) tier that is a subset of RECO easily accessible for direct use by analyses, containing high-level objects and summaries of RECO data [61]. The AOD dataset used in this thesis is shown in Table 3.1

Table 3.1. Dataset for $\mathrm{Pb}+\mathrm{Pb}$ 2018 5.02 TeV collisions.

Type	Dataset
Double Muon	/HIDoubleMuon/HIRun2018A-04Apr2019-v1/AOD

For quarkonia analyses, a further step is taken to process the AOD data into a compact and more easily readable "Onia" tree format, named for "quark-onia". These trees are named as such because they are made to contain information on reconstructed muons and dimuons, triggers, and other global event information most relevant to studies of quarkonia. The Onia trees used in this analysis are stored in the following location at CERN's Open Storage (EOS) service:

> /eos/cms/store/group/phys_heavyions/dileptons/Data2018/PbPb502TeV/
> TTrees/ReReco/AOD/DoubleMuon/ReReco_Oniatree_addvn_part*.root

These 'DoubleMuon' Onia trees are typically used for quarkonia and B meson analyses. Specific selections made on this dataset for this thesis are described in Sec 3.3.

3.2 Monte Carlo

Monte Carlo (MC) simulations are used to estimate the performance of the detector. The detector can fail to record particles for several reasons, including physical coverage, unsuccessful track reconstruction, and others, described further in

Sec 4.2. The fraction of particles produced in a collision that the detector does not record can be estimated by simulating both the collision events and the detector response.

This analysis uses two MC samples officially produced by CMS, one for Υ and one for prompt J/ψ. Both samples consist of their respective bottomonia or charmonia events simulated in PYTHIA8.212 Tune CP5 [62], which are then embedded into simulated $\mathrm{Pb}+\mathrm{Pb}$ backgrounds generated by HYDJET1.9, tune Drum5F [63]. The CMS detector response is simulated using GEANT4 [64], and the full sequence of triggers and reconstruction algorithms is run over these simulated events. The completed samples are stored in a format named AODSIM, or Analysis Object Data Simulation. This format is equivalent to the AOD format used for real data. The samples used in this thesis are shown in Table 3.2. There are two samples for Υ which are added together for a greater total sample size.

Table 3.2. Monte Carlo samples for $\mathrm{Pb}+\mathrm{Pb}$ 2018 5.02 TeV collisions.

Process	Sample
Upsilon	/Upsilon1S_pThat-2_TuneCP5_HydjetDrumMB_5p02TeV_Pythia8/HINPbPbAutumn18DR-mva98_103X_upgrade2018_realistic_HI_v11_ext1-v1/AODSIM
Upsilon	/Upsilon1S_pThat-2_TuneCP5_HydjetDrumMB_5p02TeV_Pythia8/HINPbPbAutumn18DR-mva98_103X_upgrade2018_realistic_HI_v11-v1/AODSIM
J/ψ	/JPsi_pThat-2_TuneCP5_HydjetDrumMB_5p02TeV_Pythia8/HINPbPbAutumn18DR-mva98_103X_upgrade2018_realistic_HI_v11-v1/AODSIM

3.3 Selections

Muon candidates are selected according to particular criteria. The first important selection is the trigger, which is used both to help identify Υ candidates and to dintiguish between Υ and J/ψ candidates. The invariant mass distributions for three triggers relevant to quarkonia are shown in Fig 3.2 [30]. They are

- HLT_HIL1DoubleMuOpen_v1 (inclusive double-muon trigger),
- HLT_HIL3Mu0NHitQ10_L2Mu0_MAXdR3p5_M1to5_v1 (J/ψ-region trigger),

- HLT_HIL3Mu2p5NHitQ10_L2Mu2_M7toinf_v1 (Υ-region trigger).

From Fig 3.2 we can already see the resonance peaks for the J/ψ, the Υ, and the Z boson in the invariant-mass distributions of all three triggers. Two of these triggers feature mass gates to focus on regions surrounding particular resonances. Event counts for these triggers drop rapidly outside these respective regions, although notably not to zero: The Υ-region trigger still contains events at masses lower than its threshold. This will be discussed later in Sec. 3.4.1. We may also note from the figure that all three triggers have comparable event counts, despite the inclusive double-muon trigger being more permissive and therefore much higher frequency. This is because some triggers have 'prescales' that are used reduce the amount of data to a manageable level by discarding events periodically: e.g., a trigger with a prescale of 3 would discard two out of every three events. Here, the inclusive double-muon trigger has a large prescale so that the event count is comparable to the others.

For this analysis we choose to use the Υ-region trigger, which is notably gated to high mass. This trigger requires one muon from the pair to individually pass a level-2 (L2) trigger and the other muon to pass a level-3 (L3) trigger, and then requires this L2-L3 pair to have an invariant mass of at least 7 GeV. The L2 muons are reconstructed from track fits in the outer muon spectrometer and have a minimum p_T threshold of 2 GeV. The L3 muons also require at least 10 high-quality hits in the inner tracker, and have a minimum p_T threshold of 2.5 GeV. The full invariant-mass spectrum of all dimuons in the Υ-region trigger is shown in yellow on Fig 3.2 [30]. For the purpose of this double-dimuon analysis we consider dimuons that pass this trigger to be Υ candidates and those that do not to be potential J/ψ candidates.

Next there are acceptance cuts corresponding to the geometrical limitations of the CMS detector. As noted in Sec.[TODO: Detector chapter], the geometrical coverage for muons in the CMS detector extends to a pseudorapidity of 2.4 in both directions, so we have only muons within the range $|\eta^{\mu}| < 2.4$. There is also a

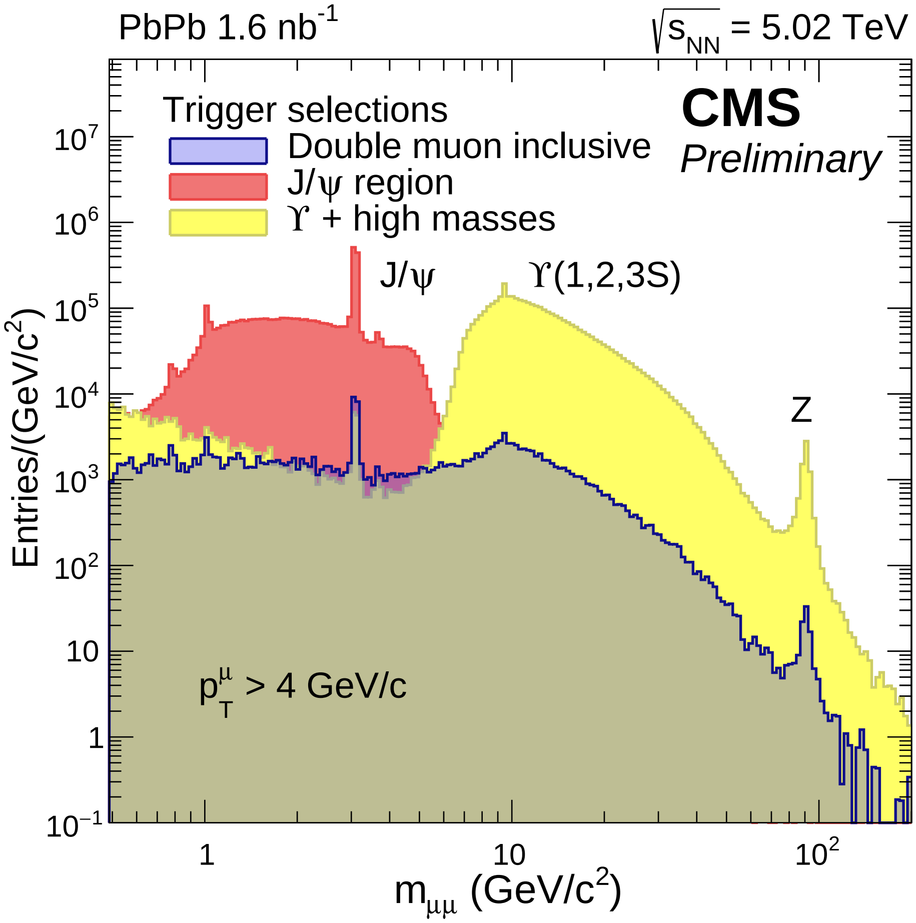

Figure 3.2. Invariant mass distributions of dimuons in Pb + Pb 2018 data for various triggers: The ϒ-region trigger (yellow) the J/ψ-region trigger (red), and the inclusive double-muon trigger (blue) [30].

minimum transverse momentum necessary for muons to be detected, or else they will only spiral inside the detector without reaching the barrel. We apply two different p_T cuts: for muons that are reconstructed as arising from decay of ϒ candidates, we apply a flat cut at $p_T^\mu > 3.5$ GeV, visible in Fig. 3.3 (left) as the red line. Muons from J/ψ candidate decays are instead required to be within the acceptance region given in Ref. [31] for untriggered muons, also defined below in Sec. 4.2. This cut is displayed as the green line in Fig. 3.3 (right). This analysis uses a single integrated analysis bin of $p_T^{\mu\mu} < 30$ GeV and $|y^{\mu\mu}| < 2.4$, within which all dimuons are required to fall.

Muons are also subject to several additional selections in order to identify them

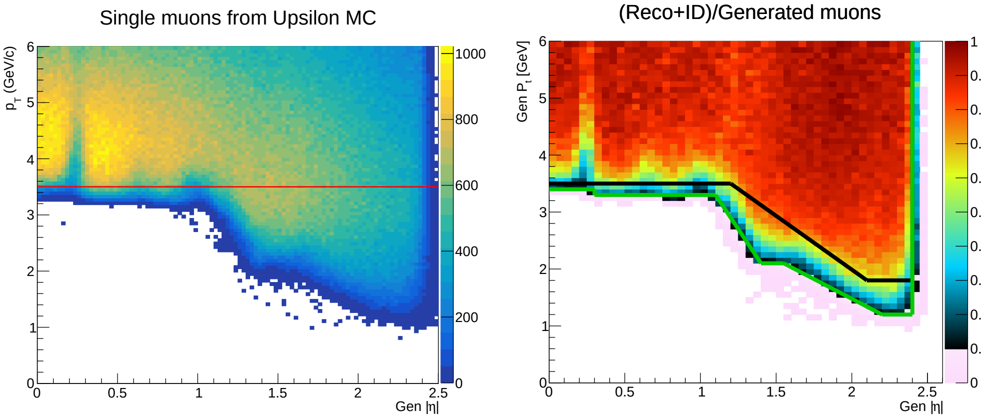

Figure 3.3. Plots of single muons from simulations of quarkonium decays. The horizontal and vertical axes on both plots represent the η and p_T of the muons, respectively. Left: Transverse momentum and $|\eta|$ of single muons from MC simulated Υ decays, with the acceptance cut shown as the red line. Color from blue to yellow indicates muon count. Right: Single muon acceptance×efficiency from MC simulated J/ψ decays [31]. The acceptance cut for 2018 Pb + Pb data is displayed as the green line, located below the black line. The black line represents older acceptance cuts used for 2015 Pb+Pb data. Color from blue to red indicates the ratio of reconstructed muons passing acceptance and efficiency selections divided by the generated muons, where a value of 1 means they agree perfectly.

with higher confidence. This analysis uses a set of cuts called HybridSoft. There exist other sets of muon identification cuts used by CMS: The strictest set of cuts, called Tight Muon ID, and the loosest, called Soft Muon ID. HybridSoft falls between these two, providing good background rejection without sacrificing too much efficiency. The HybridSoft cuts require

- at least 6 valid hits in the silicon strip layers,
- at least one valid hit in the silicon pixel detectors,
- that the distance of closest approach between the muon and the event vertex must be less than 20 cm in the longitudinal (z-axis) direction and less than 0.3 cm in the transverse plane,
- that the muon is reconstructed as both a ‘tracker muon’ and a ‘global muon’. A tracker muon is a muon that is reconstructed “inside-out”, first in the

> silicon tracker and then matched to the muon detectors; while a global muon is reconstructed “outside-in”, first in the muon detectors and then matched to the silicon tracker. A muon that is reconstructed only in the muon detectors and not the tracker is called a stand-alone muon.

In addition to the HybridSoft muon ID cuts above, we also require additional cuts on the dimuon candidates. As we are looking for muons from quarkonium decays, we require that the muons in a pair have opposite charges, and also that the probability they share a common vertex is greater than 1%.

3.4 Double dimuons

Because the goal of this analysis is to measure double-quarkonia production, we want to find and consider independent pairs of dimuons. To this end, we select only collision events containing at least four muons (two positive and two negative) that pass the muon selections described above. For each collision event satisfying this, all dimuons surviving the selections are arranged into pairs of every possible combination. Any dimuon pair that shares one or more muons between them is discarded, as it could not possibly be from two separate quarkonium decays. These steps leave us with a dataset of only independent dimuon pairs, as desired. Then, in addition, we require that at least one dimuon in the pair satisfies the mass-gated trigger; that is, that there is at least one Υ candidate in the pair. If both dimuons satisfy the trigger, then the dimuon with greater invariant mass is chosen as the Υ candidate and the dimuon with the lesser mass as the J/ψ candidate.

Examples of various dimuon combinations and how they are added or excluded are shown in Fig 3.4 for events with two positive muons (blue circles) and two negative muons (red circles) that pass selections. The lines connecting the muons, labeled 1 through 4, represent opposite-sign dimuons that satisfy the vertex probability selection. Purple lines indicate dimuons that pass the mass-gated trigger and green lines indicate dimuons that do not pass the trigger. The “pairs added” cells show which dimuon pairs in each case satisfy all requirements and would be added to the final dataset. The color of these cells indicate which dimuon is categorized as a Υ candidate, denoted by m_1, and which is categorized as a J/ψ candidate, denoted by m_2. The cells are grey when both dimuons pass the trigger; as noted above, they are categorized by mass in this case.

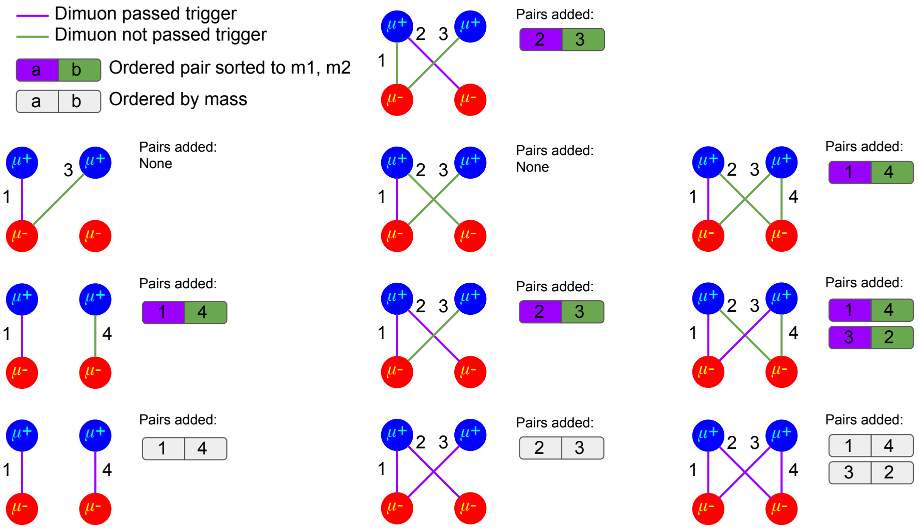

Figure 3.4. Examples of dimuon pair combinations for events with two positive muons (blue circles) and two negative muons (red circles) that pass selections. The lines connecting the muons, labeled 1 through 4, represent opposite-sign dimuons that satisfy the vertex probability selection. Purple lines indicate dimuons that pass the mass-gated trigger and green lines indicate dimuons that do not pass the trigger. The "pairs added" cells show which dimuon pairs in each case satisfy all requirements and would be added to the final dataset, with the color indicating which dimuon is sorted into the m_1 category (purple) and which is sorted into the m_2 category (green). Grey-colored cells denote that the dimuons of that pair will be sorted into the m_1 and m_2 categories according to their mass.

After all these selections are complete, the invariant mass distributions of the two categories are shown in Fig. 3.5. We can see that the effect of the mass threshold at 7 GeV in the trigger is visible, but that some low-mass dimuons also do pass the trigger and some high-mass dimuons do not. There is no visible Υ peak in the not-triggered dimuons (green), suggesting that all Υ candidates are being captured by the trigger as desired. Moreover, since pairs in which both dimuons pass the trigger have the lower-mass dimuon sorted into the not-triggered category, the lack of an Υ peak here also means that we do not see any sign of Υ+Υ pairs in

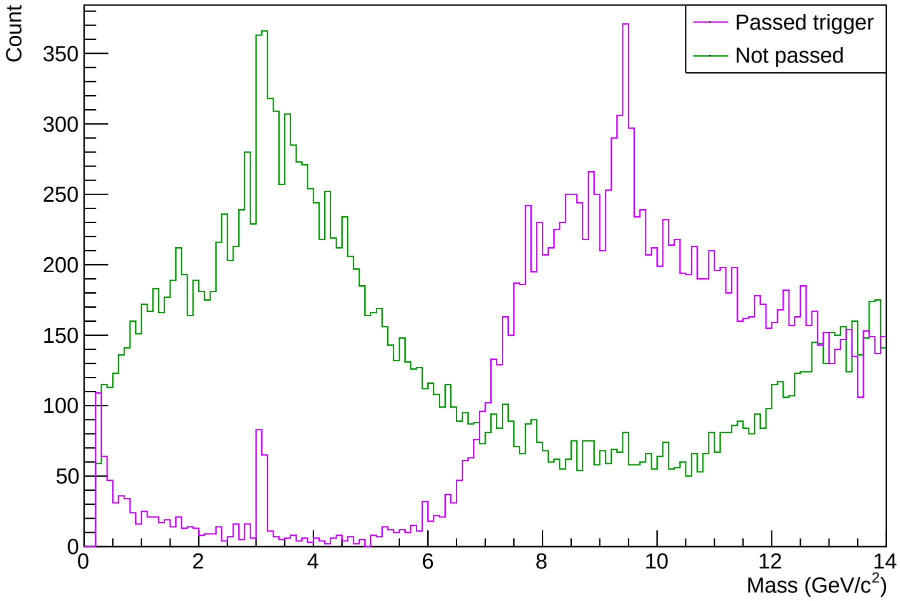

Figure 3.5. Invariant mass distribution of paired dimuons. The dimuon in the pair that passed the trigger (Υ candidate) is in purple, and the dimuon in the pair that did not pass the trigger (J/ψ candidate) is in green. If both dimuons in a pair passed the trigger, the higher mass dimuon is purple and the lower mass dimuon is green.

this data. However, among the triggered dimuons (purple) we do see a visible J/ψ resonance. We hypothesize this is due to the construction of the Onia tree used in this analysis and not an issue with the trigger itself, which we will describe in more detail below in Sec. 3.4.1. The extraneous dimuons should not have a significant effect on this analysis.

The paired dimuon invariant masses are next arranged into a two-dimensional dataset, with the masses of Υ candidates, m_1, on one axis and the masses of J/ψ candidates, m_2, on the other axis, as displayed in Fig. 3.6. Our region of interest is the lower-right quadrant, where we can see a peak at the expected locations of the dual Υ and J/ψ mass resonances. We will select the range 6–14 GeV and 2–4 GeV respectively on the triggered and not-triggered axes for the signal extraction process described next in Section 4.1.

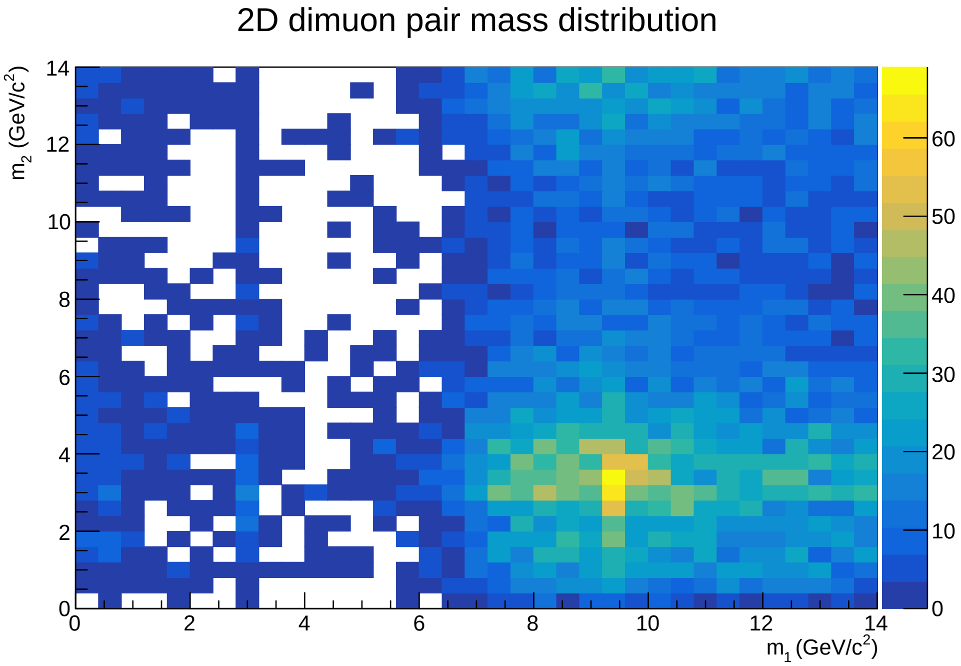

Figure 3.6. Invariant mass distribution of paired dimuons. The mass of the dimuon in the pair that passed the trigger (Υ candidate) is on the horizontal axis labeled m_1 and the mass of the dimuon in the pair that did not pass the trigger (J/ψ candidate) is on the vertical axis labeled m_2. If both dimuons in a pair passed the trigger, the higher-mass dimuon is on the horizontal axis and the lower-mass dimuon is on the vertical axis.

3.4.1 Triggers in Onia trees

We noted an excess of low-mass dimuons passing the mass-gated trigger as seen in Fig. 3.5. We hypothesize that this excess is due to the Onia tree used in this analysis. As mentioned earlier in this chapter, Onia trees are produced from a higher data tier called AOD. The AOD contains all the necessary information on the muons seen by the detector, but muon pairs (dimuons) are a more specific concept that is not present in this tier. It is during production of the Onia trees that dimuons are constructed, by taking all possible pairs of muons in each given event.

As part of making the dimuons in the Onia tree, the trigger status of each dimuon is assigned. For single-muon triggers, the dimuon is flagged as passing the trigger if either of its constituent muons pass the trigger. For double-muon triggers, the dimuon is flagged as passing the trigger if both of its constituent muons pass the trigger. However, this causes an issue with the mass-gated trigger used for this analysis: during production of the Onia tree only the individual muon triggers are considered, and not any pairwise kinematic information. It is possible to pair together two muons that each pass the mass-gated trigger—that is, they are both part of a dimuon with invariant mass greater than 7 GeV—but when paired with each other, form a dimuon with invariant mass below 7 GeV.

Figure 3.7 illustrates an example of the situation. In this example, an event has four muons and three dimuons that pass selections. The pairwise invariant mass of the two muons on the left and the two muons on the right are each greater than 7 GeV, and the diagonal pairing in the center is less than 7 GeV. In trigger processing all four muons were seen as part of a pair with invariant mass greater than 7 GeV, so the individual trigger status of each of the four muons stored in the AOD is that they passed the mass-gated trigger. Later during Onia tree production the center dimuon is assigned the status of passing the trigger despite having invariant mass less than 7 GeV, since both constituent muons are individually flagged as having passed the trigger.

This issue cannot be resolved with the current Onia trees used for this analysis as they do not contain the neccesary information. However, while these additional passing dimuons may increase the amount of background, our choice to sort pairs of dimuons that both pass the trigger by high and low mass means that any J/ψ sorted in the "passing trigger" category will be paired with lower mass dimuons, and therefore we will not be losing any potential Υ+J/ψ pairs. In addition, triggered dimuons of low mass will be ignored, as we are focused on the mass region of the Υ. Extraneous dimuons from this issue therefore should not have a significant effect on this analysis.

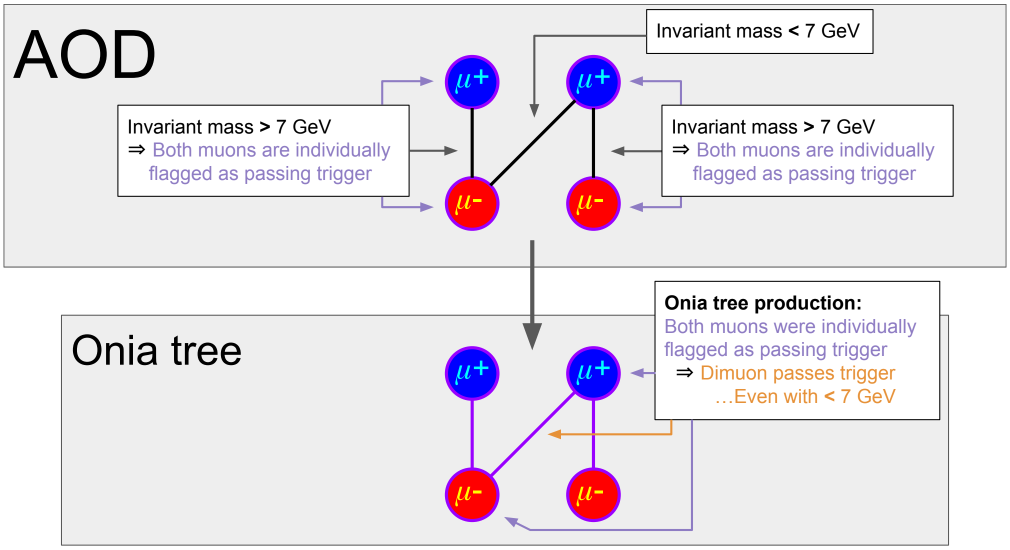
AOD
Invariant mass < 7 GeV
Invariant mass > 7 GeV
⇒ Both muons are individually flagged as passing trigger
Invariant mass > 7 GeV
⇒ Both muons are individually flagged as passing trigger
μ+
μ+
μ-
μ-
Onia tree
Onia tree production:
Both muons were individually flagged as passing trigger
⇒ Dimuon passes trigger
…Even with < 7 GeV
μ+
μ+
μ-
μ-

Figure 3.7. Illustration of dimuon trigger assignment for the case of an event with four muons and three dimuons passing selections. The pairwise invariant mass of the two muons on the left and the two muons on the right are each greater than 7 GeV, and the diagonal pairing in the center is less than 7 GeV. The individual trigger status of each of the four muons stored in the AOD is that they passed the mass-gated trigger. In the Onia tree the center dimuon is marked as passing the trigger despite having invariant mass less than 7 GeV, since both constituent muons are individually flagged as having passed the trigger.

Chapter 4

Analysis

4.1 Signal extraction

The raw yield of double quarkonia is extracted through multiple steps, beginning with unbinned maximum-likelihood fits of both Υ and J/ψ data. These preliminary one-dimensional fits obtain shape parameters for the probability density functions (PDFs) that are then used for a subsequent two-dimensional fit of Υ+J/ψ candidate dimuon pairs. The results of the two-dimensional fit are then used to calculate the final double-quarkonia yields.

The signal PDF used for both Υ and J/ψ is a sum of two Crystal Ball [65] functions. This function is a Gaussian that smoothly transitions to a power law at low mass, given by

$$\mathrm{CB}\left(x,\bar{x},n,\alpha,\sigma\right) = N \cdot \begin{cases} \exp\left(-\frac{(x-\bar{x})^2}{2\sigma^2}\right) & \text{for } \frac{x-\bar{x}}{\sigma} > -\alpha \\ A \cdot \left(B - \frac{x-\bar{x}}{\sigma}\right)^{-n} & \text{for } \frac{x-\bar{x}}{\sigma} < -\alpha \end{cases} \tag{4.1}$$

where

$$\begin{aligned} A &= \left(\frac{n}{|\alpha|}\right)^n \exp\left(-\frac{|\alpha|^2}{2}\right), \\ B &= \frac{n}{|\alpha|} - |\alpha|. \end{aligned} \tag{4.2}$$

The power law feature of this function helps to describe radiative energy loss. This energy loss could be from bremsstrahlung radiation by the muons in the detector or from radiative next-to-leading-order decay processes where a muon from the dimuon decay radiates a photon, thereby reducing the invariant mass of the muon pair. The two Crystal Balls used are constrained to the same shape, differing only by width. This accounts for differing resolution in different regions of the detector, as the resolution determines the width of the signal. The resulting Double Crystal Ball (DCB) is then

$$\begin{aligned}\mathcal{S}\left(m_{\mu\mu}; m_0, n, \alpha, \sigma, f, x\right) = f \cdot \mathrm{CB}_1\left(m_{\mu\mu}; m_0, n, \alpha, \sigma\right) + \\ (1-f) \cdot \mathrm{CB}_2\left(m_{\mu\mu}; m_0, n, \alpha, x \cdot \sigma\right)\end{aligned} \tag{4.3}$$

where $m_{\mu\mu}$ is the dimuon invariant mass, m_0 is the most probable value of the PDF, n, α, and σ are the shape parameters of the Crystal Balls, f is the fraction of one Crystal Ball relative to the other, and x is the relative width of CB_2 with respect to the width of CB_1.

In addition, because the quantity of data used for the one-dimensional fits is sufficient to resolve the $\Upsilon(2\mathrm{S})$ and $\Upsilon(3\mathrm{S})$ resonance peaks, two more double-CB functions are added, of the form

$$\begin{aligned}&\mathcal{S}_{\Upsilon(\mathrm{nS})}\left(m_{\mu\mu}; m_{\Upsilon(1\mathrm{S})}, n, \alpha, \sigma, f, x\right) \\ &\quad = \mathcal{S}_{\Upsilon(1\mathrm{S})}\left(m_{\mu\mu}; m_{\Upsilon(1\mathrm{S})} \cdot \frac{m^{\mathrm{PDG}}_{\Upsilon(\mathrm{nS})}}{m^{\mathrm{PDG}}_{\Upsilon(1\mathrm{S})}}, n, \alpha, \sigma \cdot \frac{m^{\mathrm{PDG}}_{\Upsilon(\mathrm{nS})}}{m^{\mathrm{PDG}}_{\Upsilon(1\mathrm{S})}}, f, x\right),\end{aligned} \tag{4.4}$$

where $\mathcal{S}_{\Upsilon(1\mathrm{S})}$ is the same as $\mathcal{S}$ for the $\Upsilon(1\mathrm{S})$. The additional CB functions for the excited states are constrained to use the same shape parameter values as for the ground state. To reduce the number of fit parameters, the means of the excited states are set to be equal to the m_0 of the ground state, multiplied by the ratio of their world-average measured masses. As the widths are expected to rise with increasing mass, the widths of the excited states are likewise set to the width of the ground state multiplied by the same mass ratios. The total signal PDF for the three $\Upsilon(\mathrm{nS})$ states combined is then

$$\begin{aligned}&\mathcal{S}_{\Upsilon}\left(m_{\mu\mu}; N_{\Upsilon(1\mathrm{S})}, N_{\Upsilon(2\mathrm{S})}, N_{\Upsilon(3\mathrm{S})}, m_{\Upsilon(1\mathrm{S})}, n, \alpha, \sigma, f, x\right) \\ &\quad = N_{\Upsilon(1\mathrm{S})} \cdot \mathcal{S}_{\Upsilon(1\mathrm{S})}\left(m_{\mu\mu}\right) + N_{\Upsilon(2\mathrm{S})} \cdot \mathcal{S}_{\Upsilon(2\mathrm{S})}\left(m_{\mu\mu}\right) + N_{\Upsilon(3\mathrm{S})} \cdot \mathcal{S}_{\Upsilon(3\mathrm{S})}\left(m_{\mu\mu}\right).\end{aligned} \tag{4.5}$$

The background PDFs each consist of an error function and a decaying exponential, given by

$$\mathcal{B}\left(m_{\mu\mu};\mu,\sigma,\lambda\right)=\exp\left(-\frac{m_{\mu\mu}}{\lambda}\right)\cdot\frac{1+\mathrm{Erf}\left(\frac{m_{\mu\mu}-\mu}{\sqrt{2}\sigma}\right)}{2}\ . \tag{4.6}$$

Sources of background include combinatorics and dimuons from the Drell-Yan process and $c\bar{c}$ and $b\bar{b}$ production. The exponential in the PDF describes the combinatorial background, which is the dominant background component. The error function accounts for the rise in the background at low mass caused by the p_T restriction on the muons and, in the case of the Υ, the mass-gated trigger.

For the one-dimensional fits, the combined PDFs are the sum of signal and background. The PDF for Υ is

$$\begin{aligned}\mathcal{F}_{\mathrm{1D},\Upsilon}=&\mathcal{S}_{\Upsilon}\left(m_{\mu\mu};N_{\Upsilon(\mathrm{1S})},N_{\Upsilon(\mathrm{2S})},N_{\Upsilon(\mathrm{3S})},m_{\Upsilon(\mathrm{1S})},n,\alpha,\sigma,f,x\right)\\&+N_{\mathrm{bkg}}\cdot\mathcal{B}\left(m_{\mu\mu};\mu,\sigma,\lambda\right)\end{aligned} \tag{4.7}$$

and the PDF for J/ψ is

$$\mathcal{F}_{\mathrm{1D,J}/\psi}=N_{\mathrm{sig}}\cdot\mathcal{S}\left(m_{\mu\mu};m_0,n,\alpha,\sigma_0,f,x\right)+N_{\mathrm{bkg}}\cdot\mathcal{B}\left(m_{\mu\mu};\mu,\sigma,\lambda\right). \tag{4.8}$$

Using these PDFs we perform two independent one-dimensional fits of the Υ and the J/ψ data, as shown in Fig. 4.1. After the one-dimensional fits to Υ and J/ψ are completed, we fix the shape parameters of the signal PDFs and denote them as $\mathcal{S}_{\Upsilon}$ and $\mathcal{S}_{\mathrm{J}/\psi}$.

We then proceed to the two-dimensional fits. At this stage the amount of data remaining has decreased drastically, from 7×10^5 and 2×10^6 for the 1D datasets of Υ and J/ψ down to 26,000 pairs in the 2D dataset. Because of this the $\mathcal{S}_{\Upsilon(\mathrm{2S})}$ and $\mathcal{S}_{\Upsilon(\mathrm{3S})}$ signal components for the excited states of the Υ are now dropped, as the data in the 2D dataset are insufficient to resolve these additional resonance peaks. From these fixed signal PDFs and the two background PDFs, the final combined

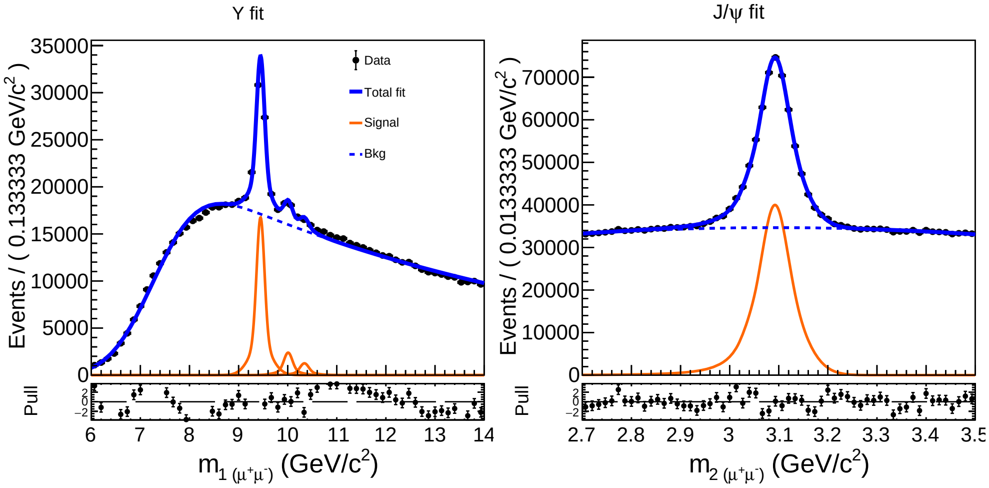

Figure 4.1. Invariant mass plots of one-dimensional fits of the Υ (left) and the J/ψ (right).

PDF for the two-dimensional fit is

$$\begin{aligned}\mathcal{F}_{\rm 2D}\left(m_1, m_2; N_{\Upsilon,{\rm J}/\psi}, N_{\Upsilon,{\rm bkg}}, N_{{\rm J}/\psi,{\rm bkg}}, N_{\rm bkg,bkg}, \mu_1, \sigma_1, \lambda_1, \mu_2, \sigma_2, \lambda_2\right) = \\ N_{\Upsilon,{\rm J}/\psi} \cdot \mathcal{S}_{\Upsilon}\left(m_1\right) \times \mathcal{S}_{{\rm J}/\psi}\left(m_2\right) \\ + N_{\Upsilon,{\rm bkg}} \cdot \mathcal{S}_{\Upsilon}\left(m_1\right) \times \mathcal{B}\left(m_2; \mu_2, \sigma_2, \lambda_2\right) \\ + N_{{\rm J}/\psi,{\rm bkg}} \cdot \mathcal{S}_{{\rm J}/\psi}\left(m_2\right) \times \mathcal{B}\left(m_1; \mu_1, \sigma_1, \lambda_1\right) \\ + N_{\rm bkg,bkg} \cdot \mathcal{B}\left(m_1; \mu_1, \sigma_1, \lambda_1\right) \times \mathcal{B}\left(m_2; \mu_2, \sigma_2, \lambda_2\right).\end{aligned} \tag{4.9}$$

In this fitting model m_1 and m_2 are the two independent axes of Υ and J/ψ candidate invariant masses, respectively, considered over the ranges 6–14 GeV for m_1 and 2–4 GeV for m_2. The four terms are the four fitting components that each account for different pairings of signal and background, illustrated in Fig. 4.2. The parameter $N_{\Upsilon,J/\psi}$ is the raw total number of Υ+J/ψ pairs (corresponding to the upper left panel of Fig. 4.2), $N_{\Upsilon,\rm bkg}$ is the number of Υ paired with background dimuons (upper right panel), $N_{J/\psi,\rm bkg}$ is the number of J/ψ paired with background dimuons (lower left), and $N_{\rm bkg,bkg}$ is the number of purely background dimuon pairs (lower right). The remaining parameters define the shape of the background as in Eq. 4.6. This two-dimensional fit is shown in Fig. 4.3. Projections of this fit onto each of the two axes are seen in Fig. 4.4.

The total yield of Υ+J/ψ is given by the signal component of the two-dimensional

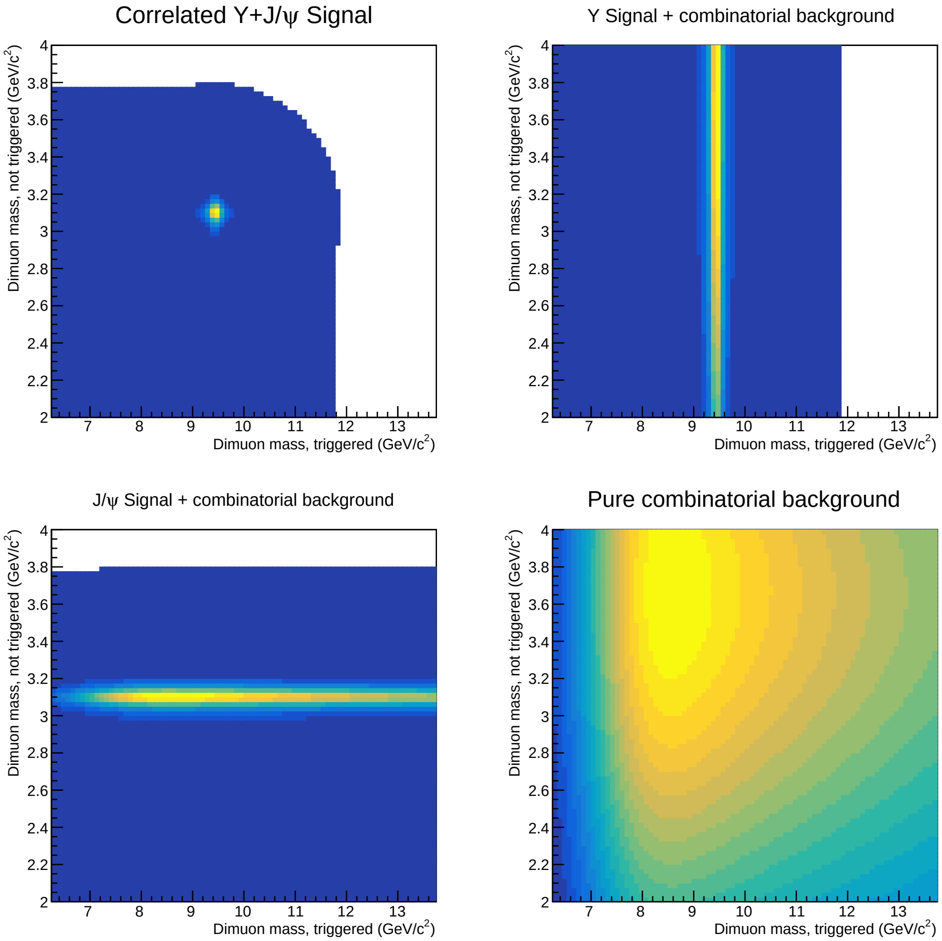

Figure 4.2. Components of two-dimensional fit to dimuon pairs in data: pure signal component of Υ+J/ψ pairs (upper left panel), ridge component of Υ paired with background dimuons (upper right), ridge component of J/ψ paired with background dimuons (lower left), and pure background component of background dimuons paired with other background dimuons (lower right).

fit. This total includes two types of simultaneous production: correlated (produced in the same nucleon-nucleon interaction) and uncorrelated (produced in separate nucleon-nucleon interactions). The correlated component is expected to be very small, less than 1% of the uncorrelated component, so we will consider it to be negligible. The uncorrelated Υ+J/ψ yield alone can also be calculated by instead using the ridge and background components of the two-dimensional fit, rather than the signal component itself. Assuming that the probability of each dimuon in a pair coming from an Υ or J/ψ respectively is independent, the probability P_{DQ} of

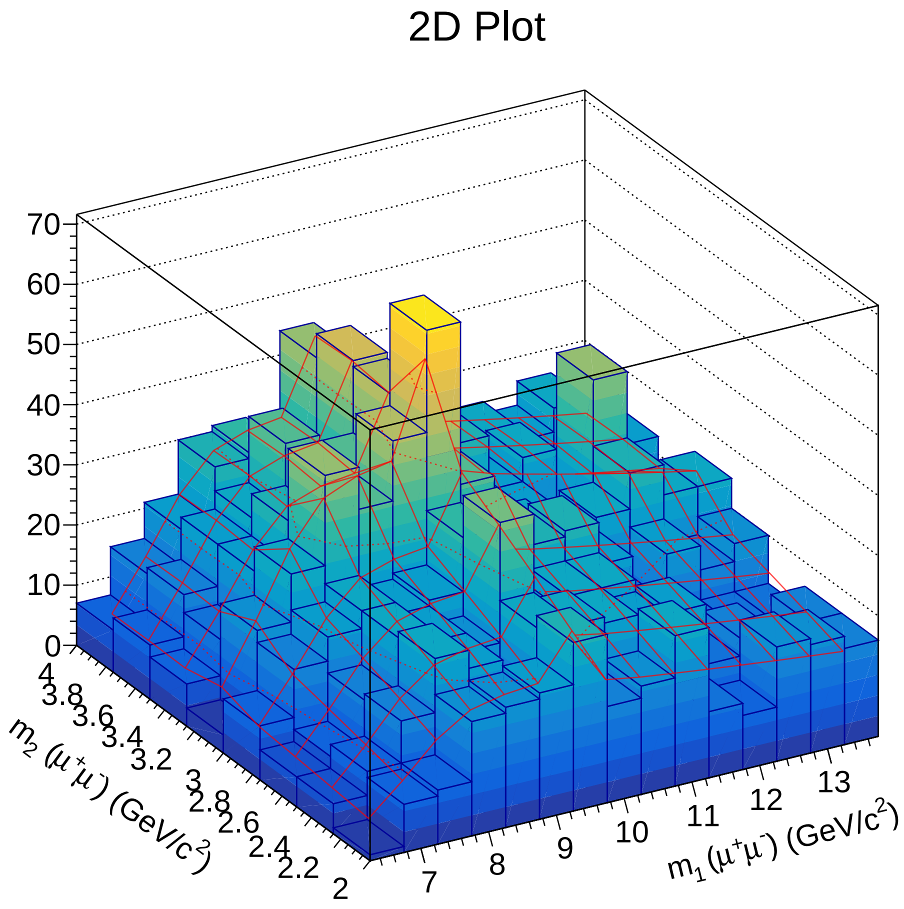

Figure 4.3. Two-dimensional fit of dimuon pairs in data. The bars represent data and the red wireframe represents the fitted model.

double quarkonia production can be written as

$$P_{\mathrm{DQ}} = P_{\Upsilon} P_{J/\psi} = \frac{N_{\Upsilon}^{\mathrm{true}}}{N_{\mathrm{total}}^{\mathrm{true}}} \frac{N_{J/\psi}^{\mathrm{true}}}{N_{\mathrm{total}}^{\mathrm{true}}}, \tag{4.10}$$

so that the total number $N_{\mathrm{DQ}}^{\mathrm{true}}$ of double-quarkonia productions is

$$N_{\mathrm{DQ}}^{\mathrm{true}} = N_{\mathrm{total}}^{\mathrm{true}} P_{\mathrm{DQ}} = \frac{N_{\Upsilon}^{\mathrm{true}} N_{J/\psi}^{\mathrm{true}}}{N_{\mathrm{total}}^{\mathrm{true}}}. \tag{4.11}$$

The notation 'true' is used to indicate that the counts are prior to any losses to acceptance or efficiency. To account for these losses, we can introduce the correction factors a_{Υ}, ε_{Υ}, $a_{J/\psi}$ $\varepsilon_{J/\psi}$ to represent the Υ and J/ψ acceptance and efficiency factors. The background dimuons may have their own factors, which we will represent here with a_{Bkg1} and ε_{Bkg1} for Υ background and with a_{Bkg2} and

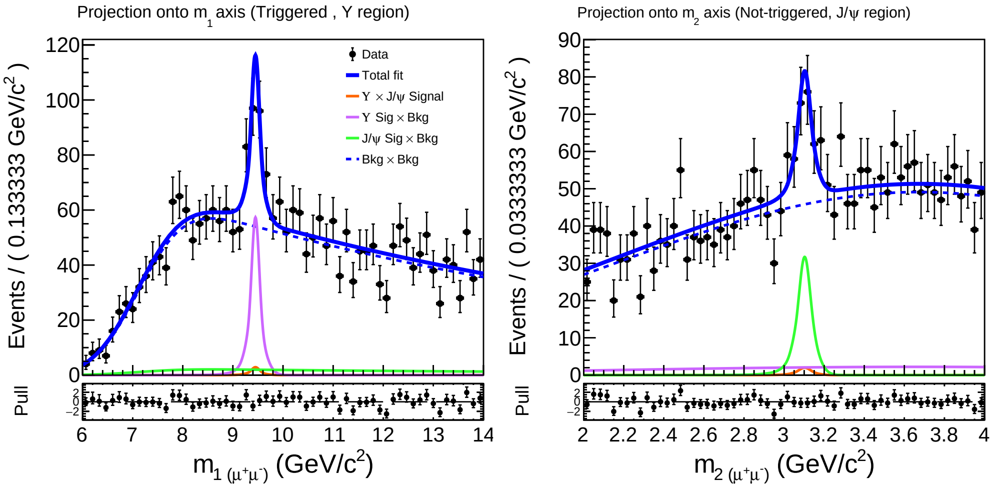

Figure 4.4. Projections of two-dimensional fit of dimuon pairs in data. The left panel shows the projection onto the Υ axis and the right panel shows the projection onto the J/ψ axis.

ε_{Bkg2} for J/ψ background. Because the quantities in Eq. 4.11 above each include dimuons from multiple sources, they must be split into separate terms so that the appropriate correction factors can be applied. The quantity $N_{\Upsilon}^{\text{true}}$ includes both Υ that are paired with background dimuons, which we denote as $N_{\Upsilon,\text{bkg}}^{\text{true}}$, and also Υ that are paired with J/ψ, denoted $N_{\text{DQ}}^{\text{true}}$, so we will rewrite it as

$$N_{\Upsilon}^{\text{true}} = N_{\Upsilon,\text{bkg}}^{\text{true}} + N_{\text{DQ}}^{\text{true}}. \tag{4.12}$$

Similarly, we will rewrite

$$N_{J/\psi}^{\text{true}} = N_{J/\psi,\text{bkg}}^{\text{true}} + N_{\text{DQ}}^{\text{true}}. \tag{4.13}$$

The total count $N_{\text{total}}^{\text{true}}$ we will write out as all four possible pairings,

$$N_{\text{total}}^{\text{true}} = N_{\text{DQ}}^{\text{true}} + N_{\Upsilon,\text{bkg}}^{\text{true}} + N_{J/\psi,\text{bkg}}^{\text{true}} + N_{\text{bkg,bkg}}^{\text{true}}. \tag{4.14}$$

With these substitutions, we now have

$$N_{\text{DQ}}^{\text{true}} = \frac{\left(N_{\Upsilon,\text{bkg}}^{\text{true}} + N_{\text{DQ}}^{\text{true}}\right)\left(N_{J/\psi,\text{bkg}}^{\text{true}} + N_{\text{DQ}}^{\text{true}}\right)}{N_{\text{DQ}}^{\text{true}} + N_{\Upsilon,\text{bkg}}^{\text{true}} + N_{J/\psi,\text{bkg}}^{\text{true}} + N_{\text{bkg,bkg}}^{\text{true}}}. \tag{4.15}$$

Next, we include the correction factors. Each "true" term in Eq. 4.15, which represents counts before efficiency and acceptance losses, is rewritten as the quantity post-losses and then corrected by acceptance and efficiency factors. Each term has two factors of a and ε in the denominator, corresponding to the two sources of dimuons for that term. We leave $N_{\mathrm{DQ}}^{\mathrm{true}}$ as-is with no substitutions or correction factors, because it is the variable we wish to solve for. After rewriting with the correction factors, we have

$$N_{\mathrm{DQ}}^{\mathrm{true}} = \frac{\left(\frac{N_{\Upsilon,\mathrm{bkg}}}{a_{\Upsilon}\varepsilon_{\Upsilon}\ a_{\mathrm{bkg2}}\varepsilon_{\mathrm{bkg2}}} + N_{\mathrm{DQ}}^{\mathrm{true}}\right)\left(\frac{N_{J/\psi,\mathrm{bkg}}}{a_{J/\psi}\varepsilon_{J/\psi}\ a_{\mathrm{bkg1}}\varepsilon_{\mathrm{bkg1}}} + N_{\mathrm{DQ}}^{\mathrm{true}}\right)}{N_{\mathrm{DQ}}^{\mathrm{true}} + \frac{N_{\Upsilon,\mathrm{bkg}}}{a_{\Upsilon}\varepsilon_{\Upsilon}\ a_{\mathrm{bkg2}}\varepsilon_{\mathrm{bkg2}}} + \frac{N_{J/\psi,\mathrm{bkg}}}{a_{J/\psi}\varepsilon_{J/\psi}\ a_{\mathrm{bkg1}}\varepsilon_{\mathrm{bkg1}}} + \frac{N_{\mathrm{bkg,bkg}}^{\mathrm{true}}}{a_{\mathrm{bkg1}}\varepsilon_{\mathrm{bkg1}}\ a_{\mathrm{bkg2}}\varepsilon_{\mathrm{bkg2}}}} \tag{4.16}$$

Solving for $N_{\mathrm{DQ}}^{\mathrm{true}}$, the final equation is

$$N_{\mathrm{DQ}}^{\mathrm{true}} = \frac{N_{\Upsilon,\mathrm{Bkg}}\ N_{J/\psi,\mathrm{Bkg}}}{a_{\Upsilon}\varepsilon_{\Upsilon}\ a_{J/\psi}\varepsilon_{J/\psi}\ N_{\mathrm{bkg,bkg}}}, \tag{4.17}$$

where $N_{\mathrm{DQ}}^{\mathrm{true}}$ is the yield of uncorrelated Υ+J/ψ, $N_{\Upsilon,\mathrm{Bkg}}$ is the yield of the Υ ridge, $N_{J/\psi,\mathrm{Bkg}}$ is the yield of the J/ψ ridge, $N_{\mathrm{bkg,bkg}}$ is the yield of the background component, and a_{Υ}, ε_{Υ}, $a_{J/\psi}$, and $\varepsilon_{J/\psi}$ are the acceptance and efficiency correction factors for Υ and J/ψ. The statistical uncertainty of this formula is

$$\begin{aligned}\sigma\left(N_{\mathrm{DQ}}^{\mathrm{true}}\right) = \Bigg[&\left(\frac{N_{J/\psi,\mathrm{bkg}}}{a_{\Upsilon}\varepsilon_{\Upsilon}\ a_{J/\psi}\varepsilon_{J/\psi}\ N_{\mathrm{bkg,bkg}}}\right)^2 \sigma^2\left(N_{\Upsilon,\mathrm{bkg}}\right) \\ &+ \left(\frac{N_{\Upsilon,\mathrm{bkg}}}{a_{\Upsilon}\varepsilon_{\Upsilon}\ a_{J/\psi}\varepsilon_{J/\psi}\ N_{\mathrm{bkg,bkg}}}\right)^2 \sigma^2\left(N_{J/\psi,\mathrm{bkg}}\right) \\ &+ \left(\frac{N_{\Upsilon,\mathrm{bkg}}\ N_{J/\psi,\mathrm{bkg}}}{a_{\Upsilon}\varepsilon_{\Upsilon}\ a_{J/\psi}\varepsilon_{J/\psi}\ N_{\mathrm{bkg,bkg}}^2}\right)^2 \sigma^2\left(N_{\mathrm{bkg,bkg}}\right)\Bigg]^{1/2},\end{aligned} \tag{4.18}$$

where we ignore the statistical uncertainty from the acceptance and efficiency corrections that are negligible due to the large MC samples used to estimate them. Because the ridge and background components from the fit are larger and have smaller relative statistical uncertainty than the pure signal component, using this formula will provide smaller statistical uncertainty in the measurement of the uncorrelated double-quarkonia yield.

4.2 Acceptance and efficiency corrections

There are two correction factors that must be accounted for in this measurement. The first is the acceptance, which reflects the physical coverage where the detector can measure particles. Because of the limited coverage it is possible for Υ or J/ψ produced in collisions to go unrecorded by the detector if one or both of their muons fall outside the area of acceptance. We therefore need to estimate the fraction of all produced dimuons that are accepted in order to correct for this loss. We call this fraction the acceptance correction factor.

To estimate the acceptance factor, a PYTHIA [62] simulation is used to generate Υ and J/ψ mesons and simulate their decays into muon pairs. The kinematics of the simulated muons are then checked to determine if they fall within the acceptance of the detector. For muons from Υ decays this kinematic region is $p_T^\mu > 3.5$ GeV and $|\eta^\mu| < 2.4$. Muons from J/ψ decays must fall in the region defined by Ref. [31] for untriggered muons, which is

- $|\eta^\mu| < 2.4$;
- if $|\eta^\mu| < 0.3$, then $p_T^\mu > 3.4$ GeV;
- if $0.3 < |\eta^\mu| < 1.1$, then $p_T^\mu > 3.3$ GeV;
- if $1.1 < |\eta^\mu| < 1.4$, then $p_T^\mu > 7.7 - 4.0 \cdot |\eta^\mu|$ GeV;
- if $1.4 < |\eta^\mu| < 1.55$, then $p_T^\mu > 2.1$ GeV;
- if $1.55 < |\eta^\mu| < 2.2$, then $p_T^\mu > 4.25 - 1.39 \cdot |\eta^\mu|$ GeV;
- if $2.2 < |\eta^\mu|$, then $p_T^\mu > 1.2$ GeV.

The acceptance factor is defined as the fraction of generated Υ or J/ψ whose daughter muons both fall within their acceptance region. For Υ this is

$$a_\Upsilon = \frac{N_{\mathrm{GEN}}(p_T^{\mu\mu} < 30\text{ GeV}, \mathrm{y}^{\mu\mu} < 2.4, p_T^\mu > 3.5\text{ GeV}, \eta^\mu < 2.4)}{N_{\mathrm{GEN}}(p_T^{\mu\mu} < 30\text{ GeV}, \mathrm{y}^{\mu\mu} < 2.4)}. \tag{4.19}$$

For J/ψ the equation is identical except for the different acceptance region for muons in the numerator, as noted above. Integrated over the entire kinematic range studied ($p_T^{\mu\mu} < 30$ GeV, $\mathrm{y}^{\mu\mu} < 2.4$), the acceptance factor for Υ is measured as

0.37±0.01 and for J/ψ it is measured as 0.044±0.013. The systematic uncertanties quoted here are explained in Sec. 4.4.1.

Because this analysis is limited to a specific region of phase space, another type of acceptance correction is also useful. The phase space acceptance factor estimates what fraction of all quarkonia produced in collisions will fall within the studied kinematic range. This factor is found by taking the ratio of generated Υ or J/ψ (i.e. the denominator from Eq. 4.19) within the kinematic range of the analysis as the numerator over the total number generated in all phase space. The phase space correction factor is measured as 0.83 for Υ and 0.77 for J/ψ.

The second correction factor is the efficiency. This factor comes from multiple sources: the efficiency of the muon quality selections, of the trigger, and of the reconstruction algorithm. To estimate the efficiency, we use the Monte Carlo samples described in Sec. 3.2. The efficiency factor is defined as

$$\varepsilon = \frac{N_{\mathrm{RECO}}(\mathrm{Acc}, \mathrm{muID}, \mathrm{trigger}, \mathrm{VtxProb})}{N_{\mathrm{GEN}}(\mathrm{Acc})} \otimes \mathrm{SF}(p_T^{\mu^+}, \eta^{\mu^+}) \times \mathrm{SF}(p_T^{\mu^-}, \eta^{\mu^-}), \quad (4.20)$$

where the denominator is the number of generated dimuons that are within the acceptance, as described above, and the numerator is the number of matched reconstructed dimuons that also satisfy the selection criteria. This ratio would be sufficient if the simulated Monte Carlo samples matched the data perfectly, but typically they do not. We therefore multiply the ratio by “scale factors” $\mathrm{SF}(p_T^{\mu^+}, \mathrm{y}^{\mu^+})$ and $\mathrm{SF}(p_T^{\mu^-}, \mathrm{y}^{\mu^-})$ for the two respective daughter muons of each dimuon, which account for differences between simulation and data.

The scale factors were obtained at CMS by the tag-and-probe method. In this method two objects are paired, one labeled the “tag” and the other the “probe”. For finding muon efficiencies, the tag and the probe are two daughter muons matched to the same decay of a resonance such as J/ψ or Z. The tag is subjected to very strict selection criteria so as to identify it as a muon with very high confidence. The probe is instead subject to much looser selections intended to be as unbiased as possible. Ideally, if the probe criteria were completely unbiased, we could measure the absolute efficiency of the probe selections; in practice it is not exact but close. By reconstructing the tag and probe pair and verifying that they originate from the same decay point and that their 4-momentum sum results in an invariant mass consistent with a J/ψ or Z as noted above, the probe can be identified with high confidence by its association to the tag despite the loose selection. The dimuon resonance is then fitted and the yield extracted. This is done twice: first for "passing probes", which are tag-and-probe pairs whose probe passes a particular selection; second, the fit is performed for all probes irrespective of that selection. By dividing the resonance yield from the passing probes by the resonance yield from all probes, the efficiency of the probe's selection criteria can be measured. This method only measures the efficiency out of the known muons identified by tags, not all muons, so it finds only a relative efficiency. Therefore, the process is conducted twice, once for real data and once for MC. One can then obtain a quantitative estimate of the difference between data and MC by taking a ratio of these two efficiencies. If the ratio is 1, the MC matches the data. Departures from 1 can then be taken into account as a correction "scale factor". This scale factor is defined as

$$\mathrm{SF}_{\mu\mu} = \frac{\varepsilon_{\mu\mu}\,(\mathrm{data})}{\varepsilon_{\mu\mu}\,(\mathrm{MC})}. \tag{4.21}$$

For this analysis of double-quarkonia, which studies pairs of Υ and J/ψ candidates, several different scale factors are applied. For the Υ candidate, the scale factors for trigger, reconstruction, and muon identification are used. The trigger scale factor is further broken down into two parts, the L2 efficiency and the L3 efficiency. Both muons are required to pass the L2 trigger. Only one muon is required to pass the L3 trigger, which is a subset of the L2. To properly account for the probabilities of every combination of these two triggers among the two muons, the trigger efficiency scale factor is calculated using the formula

$$\mathrm{SF}^{\mathrm{trig}}_{\mu\mu} = \frac{\varepsilon^{\mathrm{trig}}_{\mu\mu}\,(\mathrm{data})}{\varepsilon^{\mathrm{trig}}_{\mu\mu}\,(\mathrm{MC})}, \tag{4.22}$$

where

$$\varepsilon_{\mu\mu}^{\mathrm{trig}} = \varepsilon_1^{\mathrm{L3}}\varepsilon_2^{\mathrm{L2}} + \left(\varepsilon_1^{\mathrm{L2}} - \varepsilon_1^{\mathrm{L3}}\right)\varepsilon_2^{\mathrm{L3}}. \tag{4.23}$$

The trigger efficiency scale factor is then multiplied by the reconstruction and muon identification scale factors for the same two muons of the Υ candidate. The J/ψ candidate is not required to pass any trigger, so only the reconstruction and muon identification scale factors from its daughter muons are needed and can be simply multiplied together.

After all of these steps for efficiency calculations, the overall efficiency factors integrated over the entire kinematic range were measured to be 0.49 ± 0.02 for Υ and 0.39 ± 0.02 for J/ψ. The systematic uncertanties quoted here are explained in Sec. 4.4.2.

The measured efficiencies are also compared with previous efficiency measurements from other analyses of Υ [30]and J/ψ [32]. These comparisons are of efficiencies plotted as a function of $p_T^{\mu\mu}$ for particular centralities used by those other analyses. The comparison of Υ efficiency is shown in Fig. 4.5 in 0–10% centrality, and the comparison of J/ψ efficiency is shown in Fig. 4.6 in 0–100% centrality. Note that the red points on the right plot of Fig. 4.6 are for 0–100% centrality but the legend displays 0–10%.

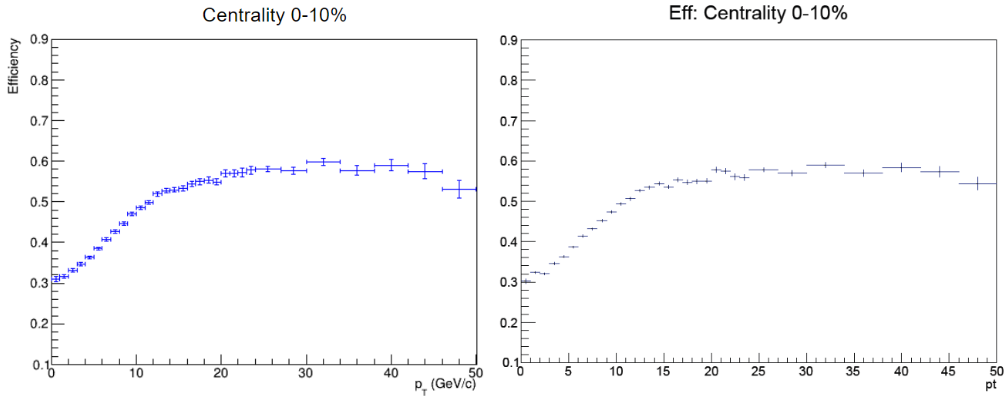

Figure 4.5. Comparison of measured Υ efficiency vs $p_T^{\mu\mu}$(left) with efficiency measurement from Ref. [30].

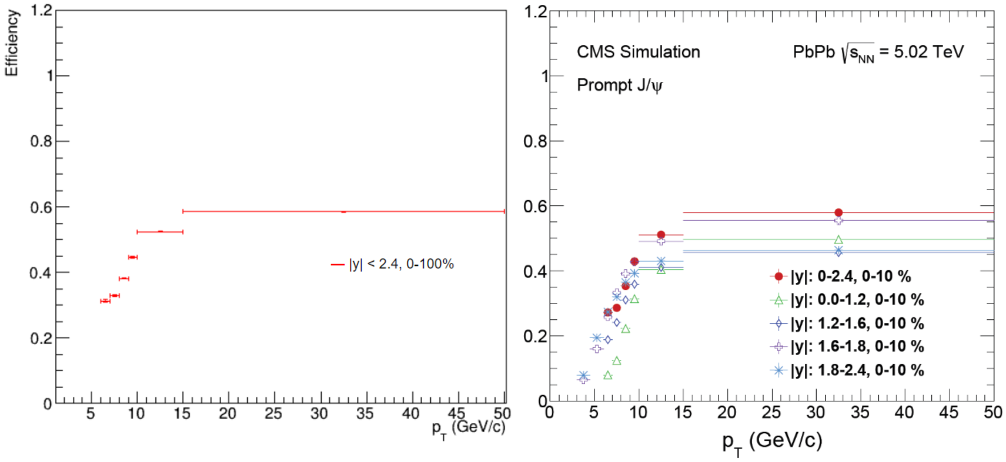

Figure 4.6. Comparison of measured J/ψ efficiency vs $p_T^{\mu\mu}$(left) with efficiency measurement from Ref. [32]. The comparable efficiency on the right plot is shown by the red points. Note that the red points on the right plot are for 0–100% centrality, but the legend displays 0–10%.

4.3 Prompt and non-prompt J/ψ

There are three categories of J/ψ that we observe in the detector. First, there are "direct" J/ψ produced in the initial nucleon-nucleon interactions. Second, excited states such as $\psi\,(2S)$ and χ_c produced in the initial nucleon-nucleon interactions can decay to the ground state J/ψ. These are radiative (electromagnetic) decays which occur so quickly that the resulting "feed-down" J/ψ are indistinguishable from direct J/ψ. These first two categories are collectively known as "prompt" J/ψ. The third category is J/ψ produced by the decay of B hadrons. This is a weak decay process that is much slower than the radiative decays from the previous category, taking approximately 1.5×10^{-12} s.

Measurements of J/ψ typically use prompt J/ψ (direct and feed-down), so for our measurement of Υ+J/ψ production we are primarily interested in pairs that include a prompt J/ψ. Therefore, we would like to estimate the ratio of non-prompt to prompt J/ψ production.

One distinguishable factor of non-prompt J/ψ is the distance traveled by the B hadron prior to decay. This distance is measureable in the detector and is typically denoted as $c\tau$, where c is the speed of light and τ is the decay time needed to travel the observed distance. By requiring that $c\tau$ be within 3σ of zero, as shown in Fig. 4.7, where σ is the standard deviation of the measured $c\tau$, we can reduce the number of J/ψ we measure from secondary decays. To estimate the impact of this selection, we perform two J/ψ fits for comparison, one requiring $c\tau < 3\sigma$ and one without this cut, and measure the yield in both cases. These fits are shown in Fig. 4.8. From the ratio of their yields, we find that the selection on $c\tau$ reduces the overall J/ψ yield by 24%.

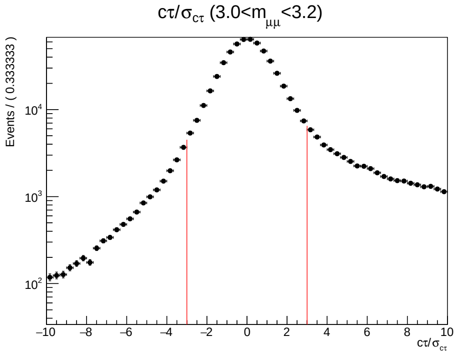

Figure 4.7. Distribution of $c\tau$ in units of standard deviation for dimuons in the mass range of the J/ψ, $3.0 < m_{\mu\mu} < 3.2$. The range of the cut on $c\tau$ is indicated by the red lines.

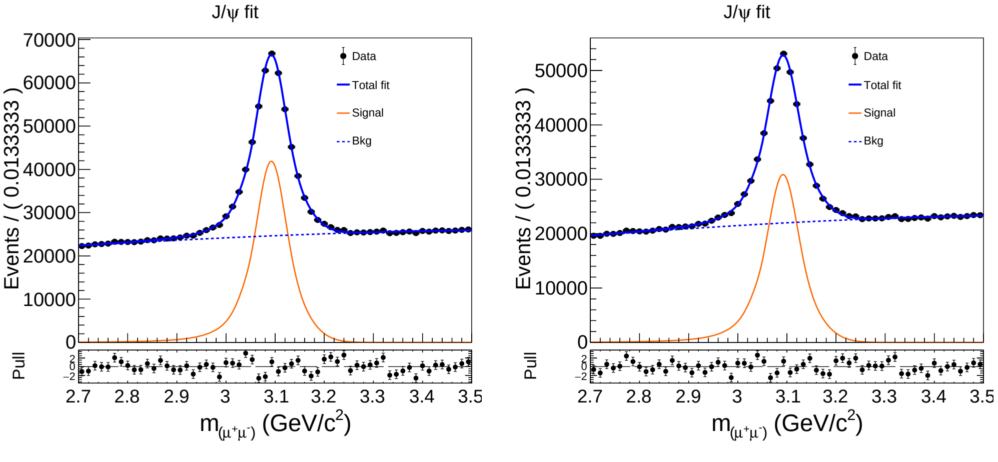

Figure 4.8. Fit of J/ψ with no $c\tau$ cut (left) and with $c\tau < 3\sigma$ (right).

4.4 Systematic uncertainties

4.4.1 Acceptance

The systematic uncertainty for the acceptance correction is estimated in two ways. First, the p_T spectrum of the MC sample is weighted to match data. This is done by dividing the kinematic range into p_T bins and comparing the signal count between data and MC. The MC contains only signal and so the count can be taken directly. For data, the signal is extracted using band subtraction. Examples of this subtraction are illustrated in Fig. 4.9, where all counts to the left, right, and below the peak are removed. In each p_T bin the ratio of data to MC is then used to weight the MC. The ratios obtained for both Υ and J/ψ as functions p_T are shown in Fig. 4.10. The acceptance factor is determined once by using the reweighted MC, and once without this weighting, and the difference in the resulting correction factor is calculated.

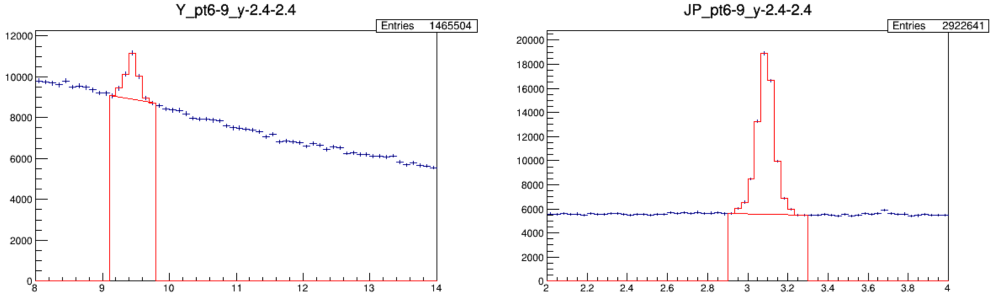

Figure 4.9. Invariant mass plots of Υ (left) and J/ψ (right) from data. All events below and beside the signal peak are subtracted, as delineated by the red lines.

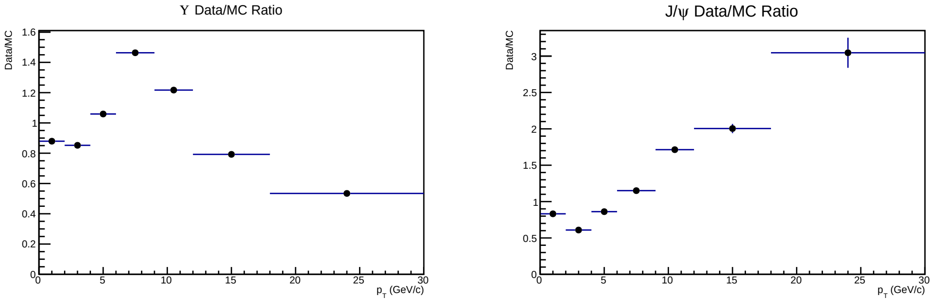

Figure 4.10. Ratios of data/MC vs p_T for Υ (left) and J/ψ (right) signal counts used for reweighting the MC for acceptance estimation.

The second way of estimating the systematic uncertainty of the acceptance correction is by adjusting the p_T setting of the PYTHIA MC sample. The nominal MC sample uses a minimum invariant p_T of 1 GeV, while the alternative sample is set at 2 GeV. The acceptance is determined twice using both samples and the difference between them is calculated.

For a conservative estimate, the systematic uncertainty of the acceptance factor is taken as the larger of the two differences calculated in the above methods. This uncertainty was measured to be 3.1% for Υ and 29% for J/ψ. Out of all systematic uncertainties, the uncertainty in acceptance for J/ψ is dominant. This is because the CMS detector has little coverage at low p_T for the J/ψ, so any modification to the p_T spectrum will have a large effect on the estimated acceptance.

4.4.2 Efficiency

The efficiency correction has a similar source of systematic uncertainty as the acceptance correction: from the p_T spectrum of the MC sample. To estimate the uncertainty we again use a p_T reweighting procedure to match the p_T spectrum of the MC sample to that of data. This procedure is the same as for acceptance, using band subtraction to obtain the yields from data. Figure 4.11 shows the obtained ratios for both Υ and J/ψ as functions of p_T.

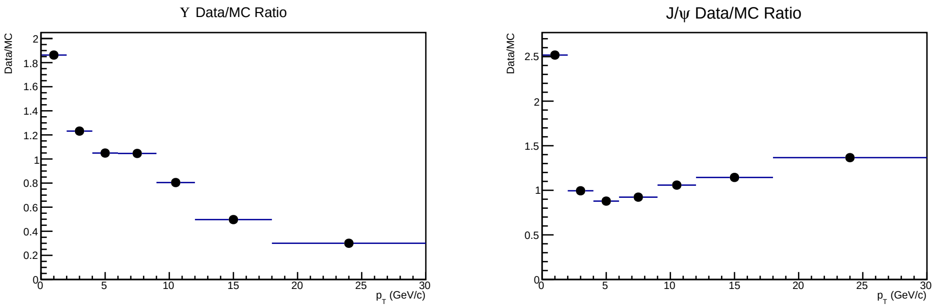

Figure 4.11. Ratios of data/MC as functions of p_T for Υ (left) and J/ψ (right) signal counts used for reweighing the MC for efficiency estimation.

The systematic uncertainty of the efficiency correction factor is taken as the difference in the resulting correction factor with and without weighting. We measured this uncertainty to be 5.1% for Υ and 4.6% for J/ψ.

4.4.3 Signal PDF

Since we are not absolutely certain that the PDF we chose to model the signal is the true PDF, this introduces a systematic uncertainty in the signal extraction. We estimate the size of this systematic uncertainty by comparing our nominal result to a result obtained using an alternative signal PDF.

For the alternative signal PDF, we choose the Hypatia function [66]. This function is defined as

$$\text{Hypatia2}\left(x,\mu,\sigma,\lambda,\zeta,\beta,a_l,n_l,a_r,n_r\right)=\begin{cases}\frac{G(\mu-a_l\sigma,\mu,\sigma,\lambda,\zeta,\beta)}{\left(1-\frac{x}{n_l G(\dots)/G'(\dots)-a_l\sigma}\right)^{n_l}} & \text{if } \frac{x-\mu}{\sigma}<-a_l\\ G\left(x,\mu,\sigma,\lambda,\zeta,\beta\right) & \text{otherwise}\\ \frac{G(\mu+a_r\sigma,\mu,\sigma,\lambda,\zeta,\beta)}{\left(1-\frac{x}{-n_r G(\dots)/G'(\dots)-a_r\sigma}\right)^{n_r}} & \text{if } \frac{x-\mu}{\sigma}>a_r\end{cases} \tag{4.24}$$

where

$$\begin{aligned}&G\left(x,\mu,\sigma,\lambda,\zeta,\beta\right)=\\ &\left((x-\mu)^2+A_\lambda^2\left(\zeta\right)\sigma^2\right)^{\frac{1}{2}\lambda-\frac{1}{4}}e^{\beta(x-\mu)}K_{\lambda-\frac{1}{2}}\left(\zeta\sqrt{1+\left(\frac{x-\mu}{A_\lambda\left(\zeta\right)\sigma}\right)^2}\right),\end{aligned} \tag{4.25}$$

The ratio $A_\lambda^2\left(\zeta\right)$ is

$$A_\lambda^2\left(\zeta\right)=\frac{\zeta K_\lambda\left(\zeta\right)}{K_{\lambda+1}\left(\zeta\right)}, \tag{4.26}$$

and K_λ are cylindrical harmonics or special Bessel functions of the third kind. For more details, see Ref. [66]. The Hypatia function resembles the nominal Crystal Ball function and has parameters for the peak location, width, and tails for the lower and upper ends, and so is reasonable to use as an alternative signal PDF.

To distinguish the systematic uncertainty of the PDF choice from the statistical uncertainty of the fit, 100 pseudoexperiments are performed using pseudodata generated from the nominal fit. Each set of pseudodata is fitted twice, once using the nominal signal PDF and again using the alternative signal PDF. The relative difference in double-quarkonia yield is measured and stored in a histogram that contains all 100 entries from the pseudoexperiments, as seen in Fig. 4.12 The mean and the RMS of this histogram both describe how the two results differ, so we take their quadratic sum as a conservative estimate of the systematic uncertainty. This uncertainty due to variation of the signal PDFs was measured to be 2.2% for Υ and 5.4% for J/ψ.

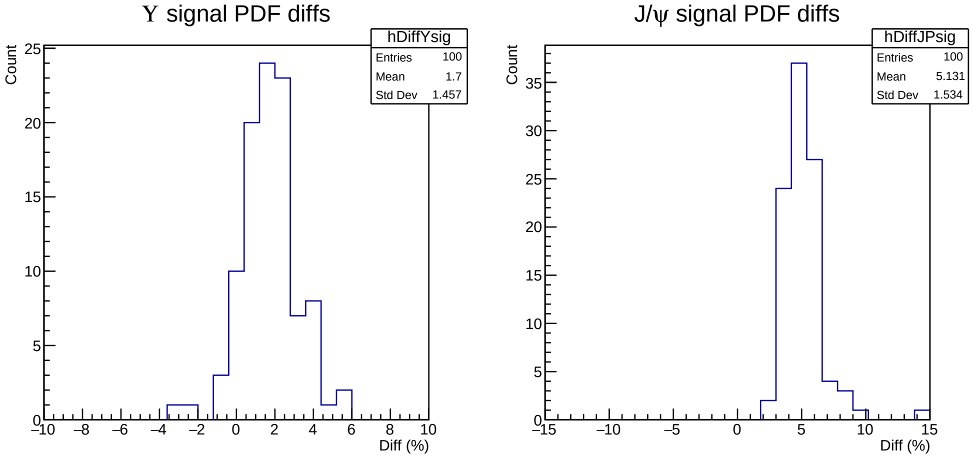

Figure 4.12. Percentage differences in double-quarkonia yield between nominal and alternate signal PDF for Υ (left) and J/ψ (right).

4.4.4 Background PDF

The uncertainty due to the choice of background PDF is estimated in the same way as for the signal PDF, by substituting an alternative background PDF and performing 100 pseudoexperiments. In this case, the alternative background PDF is a 4th-order Chebychev polynomial.

The results of the pseudoexperiments are shown in Fig. 4.13. From this, the systematic uncertainty due to variation of the background PDFs was measured to be 5.8% for Υ and 7.0% for J/ψ.

4.4.5 Fixed parameters

When the shape parameters of the signal PDFs in the two-dimensional fit are first fixed by preliminary one-dimensional fits, this specific choice of fixed parameters may introduce another source of systematic uncertainty. To estimate this uncertainty, the parameters are fixed by an alternative method: performing the preliminary fits on the MC samples from Sec. 3 instead of on data. The shape parameters from both methods for the Υ and J/ψ signal PDFs are tabulated in

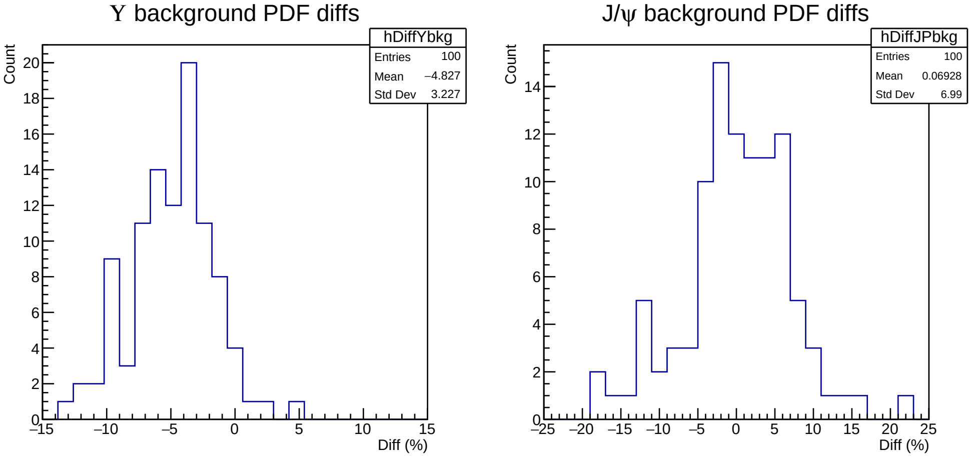

Figure 4.13. Percentage differences in double-quarkonia yield between nominal and alternate background PDF for Υ (left) and J/ψ (right).

Parameter	Υ Data	Υ MC	J/ψ Data	J/ψ MC
n	3.7179	1.3509	3.7138	1.5223
α	3.281	1.9027	1.5109	2.0011
σ	0.21917	0.17534	0.023636	0.030704
f	0.40638	0.20939	0.29781	0.77713
x	0.35977	0.45872	2.0227	2.1067

Table 4.1. Shape parameters of Υ and J/ψ signal PDFs obtained from 1D fits to data and MC.

Table 4.1. Variation in the shape parameters between fits data and to MC are expected due from differences in the invariant mass distributions, as the MC is not an exact match to data. Pseudoexperiments are again used, fitting each set of pseudodata twice using the signal shape parameters determined from both methods and comparing the difference in double-quarkonia yield.

The results of the pseudoexperiments are shown in Fig. 4.14. The uncertainty due to variation of the signal shape parameters was measured to be 6.9% for Υ and 5.0% for J/ψ.

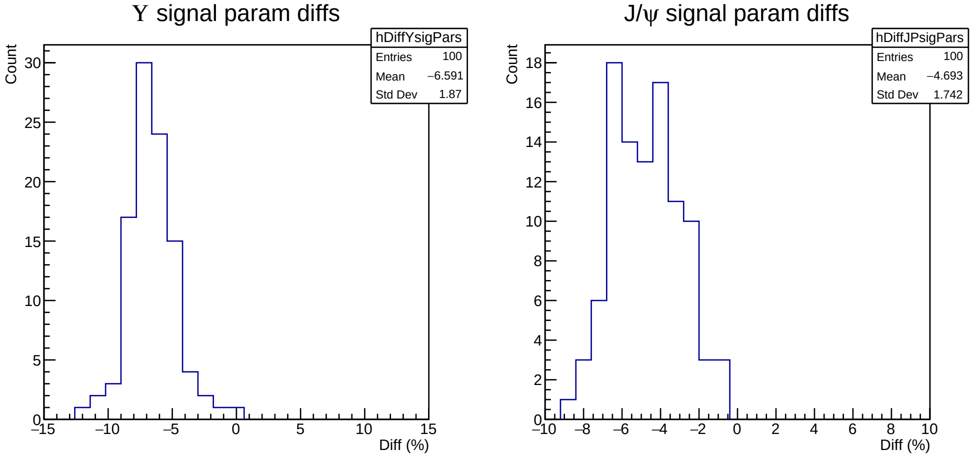

Figure 4.14. Percentage differences in double-quarkonia yield between nominal and alternate signal parameters for Υ (left) and J/ψ (right).

4.5 Closure test

To verify that the calculational procedure derived in Sec. 4.1 properly describes the yield of double quarkonia, a closure test is performed by creating and analyzing a MC sample that has a known quantity of double quarkonia.

To begin, the sample is created by generating many dimuon-mass pairs that represent paired Υ and J/ψ candidates. For each mass pair, two random probabilities, p_{Υ} and $p_{J/\psi}$, are independently evaluated to determine if the first mass will represent an Υ or background dimuon, and if the second mass will represent a J/ψ or background dimuon. These two probabilities are tunable parameters that determine the signal-to-background ratio of the sample, but do not directly represent any physical cross sections. Then, the masses for the dimuon pair are generated by sampling the one-dimensional PDFs, Υ signal, J/ψ signal, Υ background, and J/ψ background, which were obtained from the nominal fit to data.

Next, acceptance and efficiency losses are also simulated. Four tunable "efficiency" parameters—$\varepsilon^{\Upsilon}_{\mathrm{sig}}$, $\varepsilon^{\Upsilon}_{\mathrm{bkg}}$, $\varepsilon^{J/\psi}_{\mathrm{sig}}$, and $\varepsilon^{J/\psi}_{\mathrm{bkg}}$—are used to represent the consolidated acceptance and efficiency: $\varepsilon^{\Upsilon}_{\mathrm{sig}}$ for Υ signal, $\varepsilon^{\Upsilon}_{\mathrm{bkg}}$ for Υ background, $\varepsilon^{J/\psi}_{\mathrm{sig}}$ for J/ψ signal, and $\varepsilon^{J/\psi}_{\mathrm{bkg}}$ for J/ψ background. Each generated dimuon is evaluated using the corresponding efficiency parameter as a random probability to decide if it remains or is lost. If either dimuon in a pair is lost, the entire pair is lost.

This process creates a two-dimensional sample of dimuon masses with the same shape of distributions as in data, but with exactly known quantities of each quarkonium generated and how many are lost to inefficiency. Most importantly, this includes knowledge of the number of uncorrelated double-quarkonia generated, which is the quantity for which we wish to verify our yield extraction process.

Finally, the generated sample is analyzed using the same process as is done for real data, by fitting and calculating the extracted yields. The fitting model by construction matches the shape of the sample exactly, but with statistical fluctuations. This process of generating and analyzing the sample is repeated in numerous pseudoexperiments. The calculated yields are then compared to the known signal counts from the sample generation across all pseudoexperiments to evaluate the accuracy of the analysis procedure.

Two test cases were conducted. Case 1 generated 10^6 pairs using the following parameters:

- $p_\Upsilon = 0.1$
- $p_{J/\psi} = 0.25$
- $\varepsilon^{\Upsilon}_{\text{sig}} = 0.237$
- $\varepsilon^{\Upsilon}_{\text{bkg}} = 0.0223$
- $\varepsilon^{J/\psi}_{\text{sig}} = 0.8$
- $\varepsilon^{J/\psi}_{\text{bkg}} = 0.45$

After running many pseudoexperiments for this case, we compare the results in Figs. 4.15 and 4.16. From the left plot of Fig. 4.15 we see that the mean difference between the double quarkonia yield calculated from Eq. 4.17 and the known yield in the MC sample is approximately 0.2% and the width of the distribution is 7.1%, which indicates that the calculated yield has no significant bias. The right plot shows the same differences but in units of standard deviation of the double quarkonia yield calculated from the fit. The width of this plot is very nearly 1, indicating that the error calculation for the fitted double quarkonia yield is accurate. Comparatively, we see in Fig. 4.16 that the yield extracted directly from the pure signal component of the fit ($N_{\Upsilon,J/\psi}$ from Eq. 4.9) has a mean of 4% and but much greater width of 43%, so although still unbiased this method is less precise.

This test case supports that the analysis procedure is effective for extracting the double quarkonia yield, and has smaller statistical uncertainty than extracting the yield from the pure signal component of the fit.

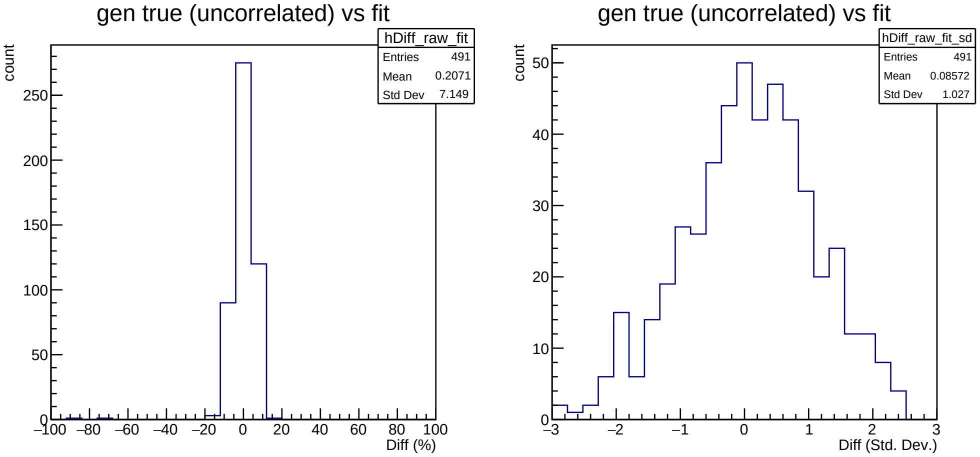
gen true (uncorrelated) vs fit

gen true (uncorrelated) vs fit

Figure 4.15. Case 1: Difference between the true number of uncorrelated double quarkonia generated in Monte Carlo and the uncorrelated yield calculated from the fit using Eq. 4.17 The differences are recorded from many pseudoexperiments and plotted twice, in units of percentage of the true number (left) and standard deviation from the fit (right).

Next, Case 2 also generates 10^6 pairs using the same parameters as in Case 1, but then in addition adds 5×10^4 Υ+J/ψ directly into the sample. This simulates the presence of correlated Υ+J/ψ not accounted for by the procedure in Sec. 4.1, which calculates only the uncorrelated yield. This case tests for the possibility of a large portion of correlated double quarkonia and how our analysis procedure would be sensitive to it.

Figure 4.17 shows the difference between the yield of double quarkonia ex-

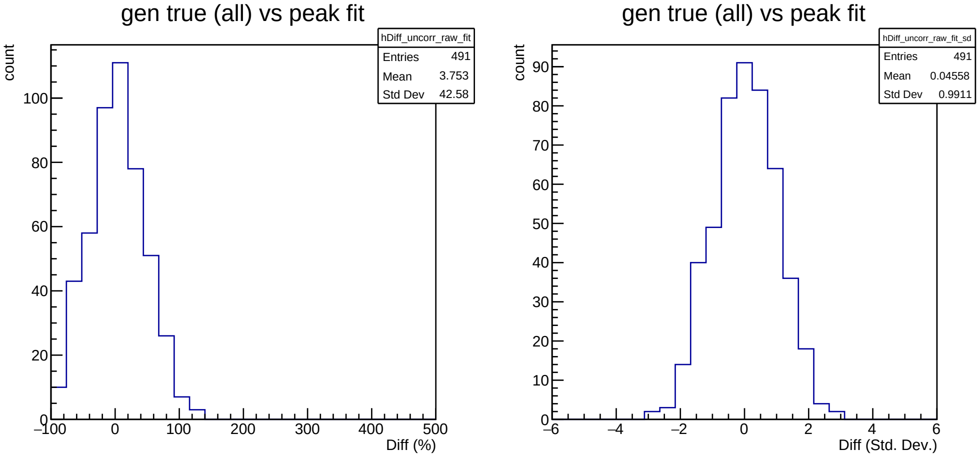

Figure 4.16. Case 1: Difference between the true number of all double quarkonia generated in Monte Carlo and the yield extracted from the pure signal component $N_{\Upsilon,\mathrm{J}/\psi}$ of the fit. The differences are recorded from many pseudo-experiments and plotted twice, in units of percentage of the true number (left) and standard deviation from the fit (right).

tracted from the pure signal component of the fit and the known total Υ+J/ψ count in the sample. We see that the width of this distribution is 13%, compared to the width of 43% seen for Case 1 in Fig. 4.16. This smaller width is expected, given the larger yield in Case 2 that can be more precisely fitted.

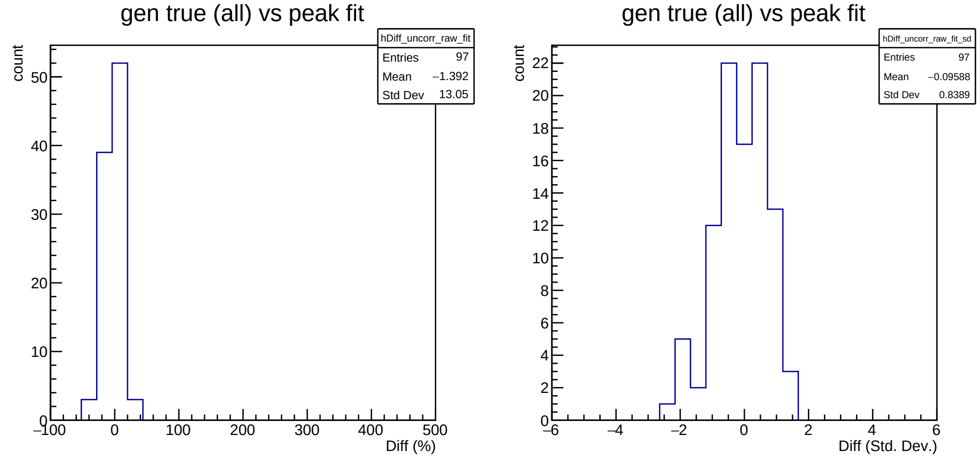

Figure 4.17. Case 2: Difference between the true number of all double quarkonia generated in Monte Carlo and the yield extracted from the pure signal component $N_{\Upsilon,\mathrm{J}/\psi}$ of the fit. The differences are recorded from many pseudo-experiments and plotted twice, in units of percentage of the true number (left) and standard deviation from the fit (right).

In addition, since the yield calculated using Eq. 4.17 is of uncorrelated $\Upsilon+J/\psi$ only, while the pure signal yield $N_{\Upsilon,\mathrm{J}/\psi}$ from Eq. 4.9 is of both correlated and uncorrelated $\Upsilon+J/\psi$, we can subtract them to measure the yield of correlated $\Upsilon+J/\psi$ alone. Figure 4.18 shows this subtraction compared to the known count of correlated $\Upsilon+J/\psi$ added to the sample. We see that this distribution has a mean of -2.2% and width of 20%, indicating that our analysis method is capable of effectively measuring the yield of correlated $\Upsilon+J/\psi$ without bias if enough statistics are available. While the current data are insufficient for this measurement, it may be possible in the future with larger datasets.

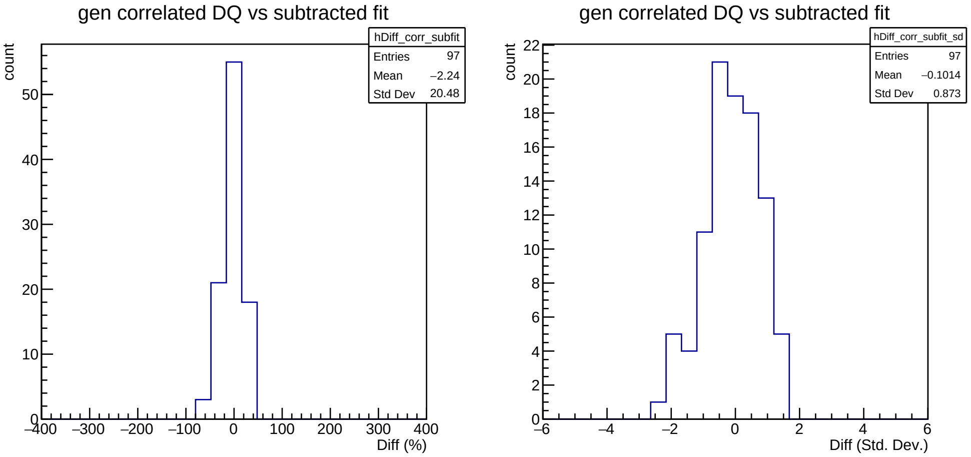
gen correlated DQ vs subtracted fit

gen correlated DQ vs subtracted fit

Figure 4.18. Case 2: Difference between the true number of correlated double quarkonia generated in Monte Carlo and the yield of the pure signal component $N_{\Upsilon,\mathrm{J}/\psi}$ minus the uncorrelated yield calculated from Eq. 4.17. The differences are recorded from many pseudoexperiments and plotted twice, in units of percentage of the true number (left) and standard deviation from the fit (right).

Chapter 5

Results

Using the two-dimensional fit and calculation method described in 4.1, we have measured the yield of Υ+J/ψ pairs in $\mathrm{Pb}+\mathrm{Pb}$ collisions. The plots of the two-dimensional fit and the corresponding projections onto the two axes have been shown in Sec. 4.1, and are reproduced here as Figs. 5.1 and 5.2 for discussion. The lower panels beneath each plot in Fig. 5.2 show the "pull" of the fit in these projections, which is a tool to help gauge how well the model fits the data. The pull displays the differences between the fitted model and binned data points, in units of the standard deviation of each datum point. We see that the points in these pulls are within two standard deviations and are not systematically high or low, indicating that the model fits the data well. Figure 5.3 shows the pull of the fit in two dimensions. This pull has three points that are 2–3 standard deviations away, but out of 120 bins this is not unreasonable. There is also no systematic shift high or low, so this pull is consistent with a uniform distribution and indicates that the model fits the data reasonably well.

The raw yields of the four fit components as defined in Eq. 4.9 are:

- $N_{\Upsilon,J/\psi} = 6 \pm 7$
- $N_{\Upsilon,\mathrm{bkg}} = 114 \pm 20$
- $N_{J/\psi,\mathrm{bkg}} = 92 \pm 20$

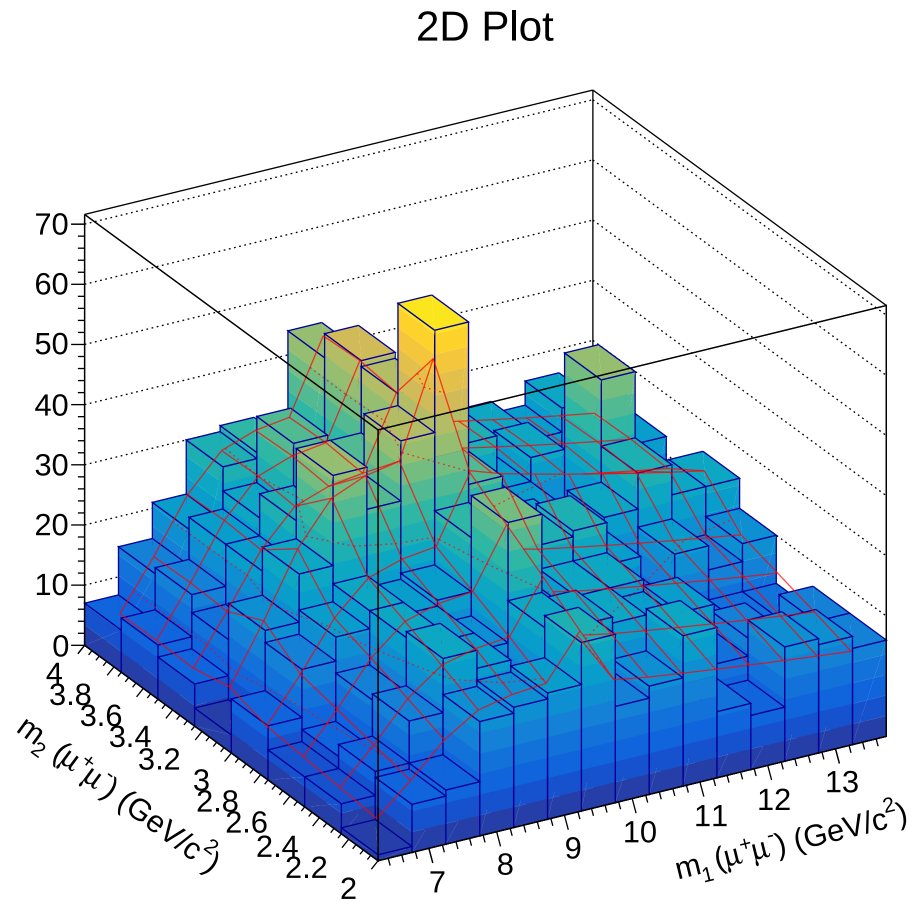

Figure 5.1. Two-dimensional fit of dimuon pairs in data. The bars represent data and the red wireframe represents the fitted model.

- $N_{\text{bkg,bkg}} = 2528 \pm 56$

where $N_{\Upsilon,J/\psi}$ is the total number of Υ+J/ψ pairs, $N_{\Upsilon,\text{bkg}}$ is the number of Υ paired with background dimuons, $N_{J/\psi,\text{bkg}}$ is the number of J/ψ paired with background dimuons, and $N_{\text{bkg,bkg}}$ is the number of purely background dimuon pairs. Using Eq. 4.17, we measure the yield of uncorrelated Υ+J/ψ to be

$$N_{\text{DQ}} = 1325 \pm 378(\text{stat.}) \pm 437(\text{sys.})$$

We see that we were able to obtain a statistically significant nonzero result for the uncorrelated yield, while the total number Υ+J/ψ pairs directly from the fit is consistent with zero. Our method of calculation was able to extract greater

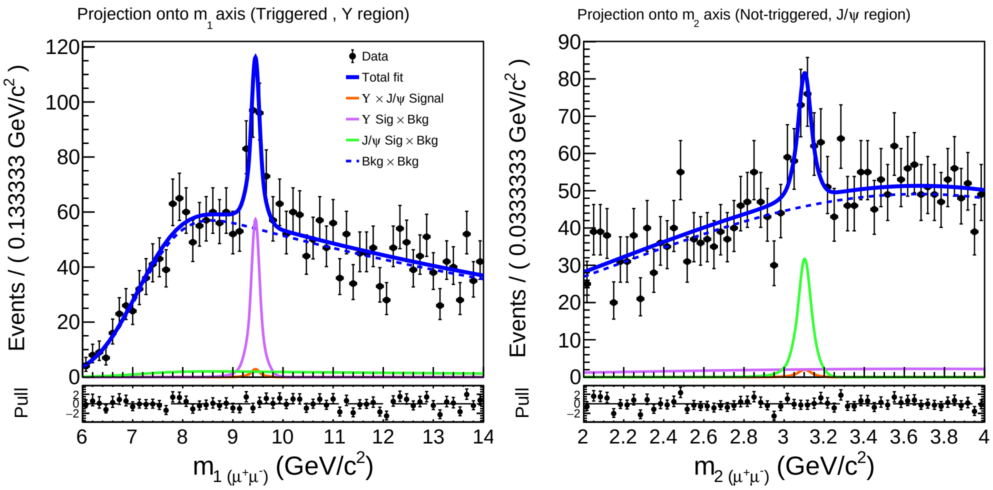

Figure 5.2. Projections of two-dimensional fit of dimuon pairs in data. The left panel shows the projection onto the Υ axis and the right panel shows the projection onto the J/ψ axis.

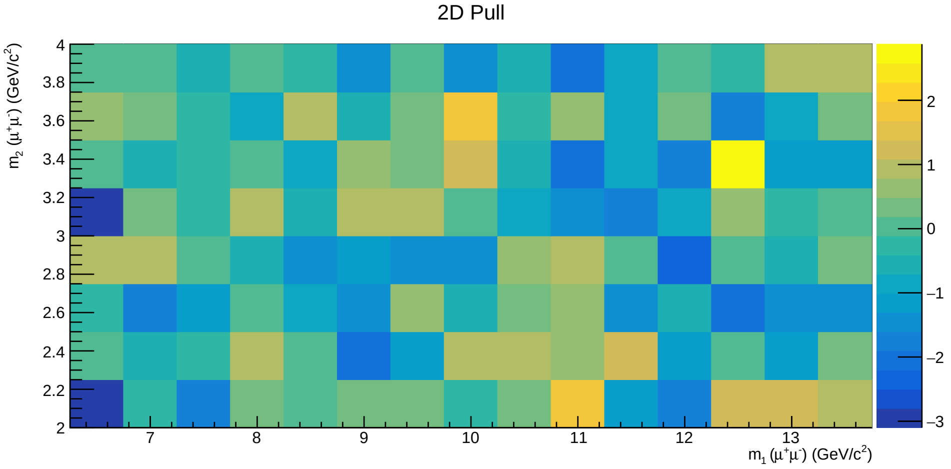

Figure 5.3. Pull of two-dimensional fit of dimuon pairs in data. The z-axis represents the difference between the fit and data, divided by the statistical uncertainty of the data in each bin.

statistical precision for the uncorrelated yield compared to obtaining the total double-quarkonium yield directly as a fit parameter. The yield of correlated double-quarkonium, which would be the difference between the total and uncorrelated, is therefore also consistent with zero by our measurement. An observation of this correlated signal will require an analysis with more data.

We found that the process of measuring double quarkonia in Pb + Pb collisions differed significantly from prior measurements in $p+p$ collisions, due the large amount of background present in Pb + Pb. Figure 5.4 illustrates this difference by comparing a previous measurement of Υ+Υ production in $p + p$ collisions [33] with our result. While $p + p$ collisions (left) exhibited a clear, distinct peak at the (m_Υ, m_Υ) mass coordinates, in Pb + Pb (right) the defining features are the two ridges indicating independent Υ and J/ψ production paired with background dimuons. This difference required us to develop our new method of measurement in 4.1 using these ridges, as the background was too great to resolve the presence of a central signal peak.

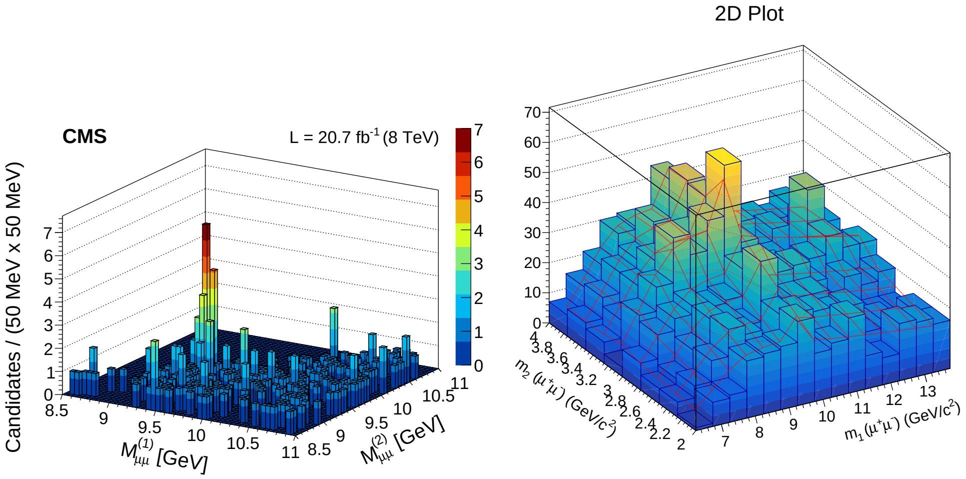

Figure 5.4. Left panel: Two-dimensional plot of dimuon pairs in $p + p$ data from [33]. Right panel: Two-dimensional plot of dimuon pairs in Pb + Pb data from this thesis, where the bars represent data and the red wireframe represents the fitted model.

5.1 Comparison to theory and simulation

We can compare our result to theoretical predictions. As noted in Sec. 1.6, the DPS cross section in Pb + Pb collisions includes contributions from three terms, accounting for three cases. In the first case, two partons from one nucleon in the first nucleus interact with two partons from one nucleon in the second nucleus. In the second case, two partons from one nucleon in the first nucleus interact with two partons from two different nucleons in the second nucleus. Finally, in the third case, two partons from two nucleons in the first nucleus interact with two partons from two different nucleons in the second nucleus. The “pocket-formula” [53, 67] for DPS is

$$\sigma^{\mathrm{DPS}}_{AA\to ab} = \frac{m}{2}\frac{\sigma^{\mathrm{SPS}}_{NN\to a}\cdot\sigma^{\mathrm{SPS}}_{NN\to b}}{\sigma_{\mathrm{eff,AA}}}, \tag{5.1}$$

where the contributions from the three terms outlined above for Pb + Pb collisions is contained in

$$\sigma_{\mathrm{eff,AA}} = \frac{1}{A^2\left[\sigma^{-1}_{\mathrm{eff,pp}} + \frac{2}{A}T_{\mathrm{AA}}\left(0\right) + \frac{1}{2}T_{\mathrm{AA}}\left(0\right)\right]}. \tag{5.2}$$

From this, the DPS cross section for Υ+J/ψ in Pb + Pb collisions at 5.5 TeV is predicted to be 28 mb [67].

In addition, the yield of Υ+J/ψ is also predicted in Ref. [67] under a particular set of assumptions. These assumptions include a collision energy of $\sqrt{s_{NN}}$ = 5.5 TeV, an integrated luminosity of 1 nb^{-1}, and branching ratios of 6% for J/ψ and 2.5% for Υ for dimuon and dielectron decay. Their calculation uses combined acceptance and efficiency factors $a \times \varepsilon$ of 0.01 for J/ψ over the rapidity range of $0 < |y| < 2$, and 0.2 for Υ over the range $0 < |y| < 2.5$. Suppression of the yield in the Pb + Pb collisions is neglected. With all these conditions, their predicted yield of Υ+J/ψ after acceptance and efficiency losses is $\sim$ 340. This does not include any uncertainty estimate, which we will discuss further below.

To compare with this prediction, we need to account for differences between their assumptions and the conditions of our measurement. We do this by multiplying their predicted yield by several factors.

First, the predicted yield includes both the dimuon and dielectron decay channels, but our analysis measures only quarkonia from dimuon decays, so we divide by a factor of 4 to compensate for using half the number of decay channels for Υ and for J/ψ.

To account for changes in quarkonium yields from differing collision energy, we multiply by the ratios of cross sections at $\sqrt{s_{NN}} = 5.02$ TeV over $\sqrt{s_{NN}} = 5.5$ TeV for both b and c quarks in $p + p$ collisions. Using cross-section calculations from a fixed-to-next-to-the-leading-order (FONLL) model [68, 69], we estimate these factors to be 0.92 and 0.95 for b and c quarks respectively.

Next, we adjust for the difference in luminosities. The integrated luminosity of our data is 1.7 nb^{-1}compared to the 1 nb^{-1}used in the prediction, so we multiply by 1.7.

The predicted yield is then divided by their simplified acceptance and efficiency factors, 0.01 and 0.2 as noted earlier, to return the yield to what it would be before losses. In addition, because their phase space is different from that in our analysis, we need to multiply by the ratio of our phase space factors, 0.55 and 0.66, over their corresponding factors. We estimate their phase space factors in a similar fashion to as we did in Sec 4.2, by dividing the number of J/ψ falling within $0 < |y| < 2$ and Υ falling within $0 < |y| < 2.5$ over the total number of each quarkonia generated in a Monte Carlo simulation using Pythia. These factors for their phase space are found to be 0.46 for J/ψ and 0.69 for Υ.

Finally, we also consider the suppression of quarkonia in heavy-ion collisions. Guided by a Glauber Monte-Carlo simulation that estimates the distribution of the number by participating nucleons, N_{part}, which is then mapped to measurements the nuclear modification factor of Υ [5] and J/ψ [44] in $\text{Pb} + \text{Pb}$ collisions as a function of centrality within our same phase space coverage, we estimate integrated suppression factors R_{AA} of approximately 0.4 for both Υ and J/ψ.

After all adjustments for making the comparison to our measurement, the final predicted double-quarkonia yield is

$$\begin{aligned}
N_{\text{DQ}}^{\text{theory}} =& 340 \times \frac{N_{\Upsilon,\text{data}}^{\text{channels}}}{N_{\Upsilon,\text{theory}}^{\text{channels}}} \times \frac{N_{J/\psi,\text{data}}^{\text{channels}}}{N_{J/\psi,\text{theory}}^{\text{channels}}} \times \frac{\sigma_b\left(5.02\text{TeV}\right)}{\sigma_b\left(5.5\text{TeV}\right)} \times \frac{\sigma_c\left(5.02\text{TeV}\right)}{\sigma_c\left(5.5\text{TeV}\right)} \times \frac{\mathcal{L}_{\text{data}}}{\mathcal{L}_{\text{theory}}} \times \\
& \frac{a\varepsilon_{\Upsilon}^{\text{data}}}{a\varepsilon_{\Upsilon}^{\text{theory}}} \times \frac{a\varepsilon_{J/\psi}^{\text{data}}}{a\varepsilon_{J/\psi}^{\text{theory}}} \times \frac{a_{\Upsilon,\text{data}}^{\text{phase}}}{a_{\Upsilon,\text{theory}}^{\text{phase}}} \times \frac{a_{J/\psi,\text{data}}^{\text{phase}}}{a_{J/\psi,\text{theory}}^{\text{phase}}} \times R_{\text{AA}}\left(\Upsilon\right) \times R_{\text{AA}}\left(J/\psi\right) \\
=& 340 \times \frac{1}{2} \times \frac{1}{2} \times 0.92 \times 0.95 \times 1.7 \times \\
& \frac{0.37 \times 0.49}{0.2} \times \frac{0.044 \times 0.39}{0.01} \times \frac{0.66}{0.69} \times \frac{0.55}{0.46} \times 0.4^2 \\
=& 36
\end{aligned} \tag{5.3}$$

For comparison, our measured yield after efficiency and acceptance losses (that is, without applying correction factors) is $N_{\mathrm{DQ}} = 4.1 \pm 1.1(\mathrm{stat.}) \pm 1.4(\mathrm{sys.})$. This value predicted by theory is larger than our measured yield, but we note that the prediction has no uncertainty estimates associated to it. It is likely that the uncertainty of this value is quite high. For instance, this prediction relies on the SPS cross sections of Υ and J/ψ. From NLO [70] and FONLL calculations [68, 69], we see that the uncertainties of these cross sections are greater than 40% even if only considering renormalization and factorization scales and variation of the b and c quark masses. Other sources of uncertainty, such as from the quarkonium production model or the phase space, would contribute even further. While the authors did not provide a full uncertainty estimation in their paper, we expect that known sources of uncertainty, such as uncertainties in the underlying cross section (which are correlated for the Υ and the J/ψ) could explain roughly a factor of 2–3 of the difference. An additional factor 2–3 would be needed from variation in the model assumptions to fully bring it into agreement with our data.

Another comparison can be made with a Glauber Monte Carlo model designed to simulate double-quarkonia production. For this model, independent probabilities of Υ and J/ψ production calculated are as

$$p_{\mathcal{Q}} = \frac{\sigma_{\mathcal{Q}}}{\sigma_{\mathrm{pp}}^{\mathrm{inel}}} \cdot \frac{1}{F_{\mathcal{Q}}^{\mathrm{direct}}} \times \mathcal{BR}\left(\mathcal{Q} \to \mu^{+}\mu^{-}\right) \tag{5.4}$$

where $\mathcal{Q}$ is either Υ or J/ψ, $\mathcal{BR}$ is the branching ratio of that quarkonium to dimuon decay, $\sigma_{\mathcal{Q}}$ is the cross section of that quarkonium, $\sigma_{\mathrm{pp}}^{\mathrm{inel}}$ is the inelastic $p+p$ cross section, and $F_{\mathcal{Q}}^{\mathrm{direct}}$ is the fraction of these quarkonia that are from direct production [71]. A Glauber Monte Carlo model is used to simulate 10^{10} nucleus-nucleus collisions, matching the expected number of $\mathrm{Pb}+\mathrm{Pb}$ collisions in the 2018 data collected by CMS. For each simulated nucleus-nucleus collision, the probabilities defined in Eq. 5.4 are randomly evaluated for every nucleon-nucleon interaction to determine if an Υ is produced and whether a J/ψ is produced. If both an Υ and a J/ψ are produced in the same nucleus-nucleus collision, it is counted as a double-quarkonia. The N_{part} value of each simulated collision event is also determined by the Glauber Monte Carlo, and this N_{part} is then used to assign an nuclear modification factor to account for suppression as described above. Acceptance and efficiency losses are also simulated. The total double-quarkonia count after these suppression, acceptance, and efficiency losses is the final Υ+J/ψ yield of the simulation.

For conditions matching our measurement, this simulation predicts an Υ+J/ψ yield of 11 ± 3(stat.). Because this simulation relies on Υ and J/ψ cross sections, it will also be subject to the same 40% uncertainties noted above, which together amount to a factor of $1.4^2 \approx 2$. As above, we compare this again to our uncorrected measured yield of $N_{\mathrm{DQ}} = 4.1 \pm 1.1(\mathrm{stat.}) \pm 1.4(\mathrm{sys.})$. This predicted yield from the simulation is greater than our measurement, but the limited uncertainty estimate from cross sections alone accounts for this difference and brings the model to agreement with our data.

The main finding of this thesis is that we have observed double-quarkonia production for the first time in heavy-ion collisions. Our result is consistent with uncorrelated production of quarkonium pairs being the dominant mechanism, and that these quarkonia are then suppressed in the Quark Gluon Plasma. The uncorrelated production takes advantage of the many nucleon-nucleon interactions in each individual $\mathrm{Pb}+\mathrm{Pb}$ collision, so that these double-quarkonium events are much more common than in $p+p$ collisions.

Chapter 6

Conclusion

Using Pb + Pb collision data at $\sqrt{s_{NN}} = 5.02$ TeV collected by the CMS detector, we have measured for the first time the yield of simulataneous uncorrelated Υ+J/ψ production in heavy-ion collisions. This measurement was accomplished by pairing Υ and J/ψ candidates reconstructed from dimuon decays into a two-dimensional distribution of invariant masses. This distribution was fitted with a four-component model accounting for total signal of correlated+uncorrelated Υ+J/ψ, single-quarkonia Υ+$\mu\mu$ and J/ψ+$\mu\mu$, and pure background $\mu\mu$+$\mu\mu$. The yield of total correlated + uncorrelated Υ+J/ψ directly from this fit was consistent with zero. To overcome low statistics for this rare double-production, we devised a method to calculate the uncorrelated double-quarkonia yield using the Υ+$\mu\mu$, J/ψ+$\mu\mu$, and $\mu\mu$+$\mu\mu$ components of the fit. The higher yields of these components provided reduced stastistical uncertainty in the calculated Υ+J/ψ yield compared to the direct signal component of the fit. With this method our yield of uncorrelated Υ+J/ψ in the kinematic range ($p_T^{\mu\mu} < 30$ GeV, $\mathrm{y}^{\mu\mu} < 2.4$) was measured as $1325 \pm 378(\text{stat.}) \pm 437(\text{sys.})$, which is a statistically significant signal at over 3σ. We compared our uncorrelated Υ+J/ψ result with theoretical predictions from NLO calculations and with Glauber Monte Carlo simulations, and found they are consistent within systematic uncertainties. A closure test that we performed suggests that with sufficient data, the method used in this analysis is able to discern correlated from uncorrelated double-quarkonia. The techniques of this first measurement of Υ+J/ψ in heavy-ion collisions will be useful for future analyses with greater quantities of data.

Appendix A

Scale factors for asymmetric dimuons

As described in Sec 4.2, the efficiency factor is defined as

$$\varepsilon = \frac{N_{\mathrm{RECO}}(\mathrm{Acc}, \mathrm{muID}, \mathrm{trigger}, \mathrm{VtxProb})}{N_{\mathrm{GEN}}(\mathrm{Acc})} \otimes \mathrm{SF}(p_T^{\mu^+}, \eta^{\mu^+}) \times \mathrm{SF}(p_T^{\mu^-}, \eta^{\mu^-}), \quad \text{(A.1)}$$

where the denominator of the ratio is the number of dimuons in the Monte Carlo simulation that are within acceptance and the numerator is the number of matched reconstructed dimuons that also satisfy the selection criteria. Since Monte Carlo simulations typically differ from data, we multiply by scale factors to correct for these differences.

The scale factors are associated with individual muons. We could simply multiply our dimuon efficiency ratio by the scale factors of each constituent muon individually if the selections on those muons were symmetric, but in the case of the Υ trigger efficiency they are not. The trigger selection is broken down into two parts: the L2 trigger and the L3 trigger. Both muons are required to pass the L2 trigger, but only one muon from the Υ decay is required to pass the L3 trigger, which is a strict subset of the L2.

To make the combined scale factor we use the procedure outlined by [72]. This procedure is illustrated by the probability tree in Fig. A.1. The probability t denotes the efficiency of the L2 trigger, and t' the efficiency of the L3 trigger, where passing the L3 trigger implies passing the L2 trigger. We first consider one muon, denoted μ_1, and branch into three possibilities: it passes both the L2 and L3 triggers, it passes only the L2 trigger, or it passes neither trigger. The third branch immediately disqualifies the dimuon from passing the trigger, but the first two branches depend on the second muon μ_2. If μ_1 passes both L2 and L3, then the dimuon passes if μ_2 either passes L2 and L3 or just passes L2. If μ_1 passes only L2, then the dimuon only passes if μ_2 passes both L2 and L3.

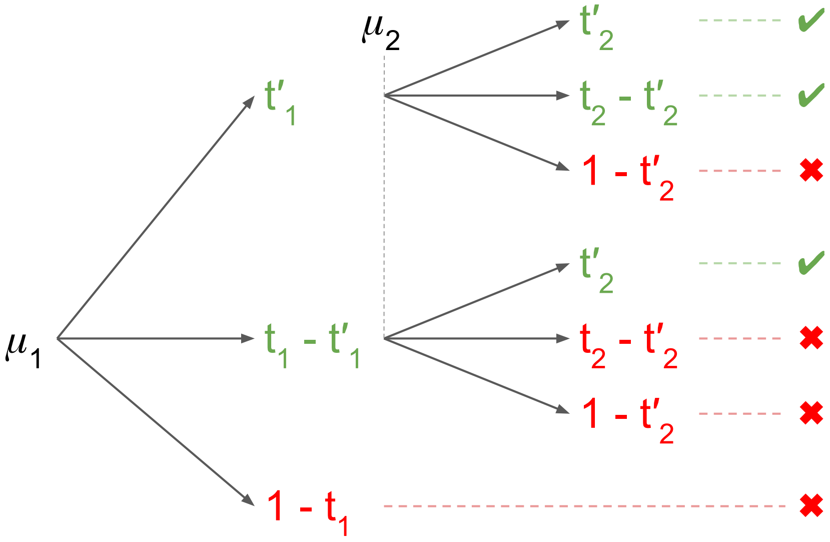

Figure A.1. Probability tree of asymmetric dimuons. Green denotes branches that pass the efficiency, and red denotes branches that do not pass.

By multiplying each stage of probability and adding branches together, we find

$$\begin{aligned} \varepsilon_{\mu\mu} &= t'_1 \left(t'_2 + t_2 - t'_2\right) + \left(t_1 - t'_1\right) t'_2 \\ &= t'_1 t_2 + \left(t_1 - t'_1\right) t'_2. \end{aligned} \tag{A.2}$$

Rewriting t and t' back in terms of L2 and L3 efficiencies, we have the formula

$$\varepsilon^{\mathrm{trig}}_{\mu\mu} = \varepsilon^{\mathrm{L3}}_1 \varepsilon^{\mathrm{L2}}_2 + \left(\varepsilon^{\mathrm{L2}}_1 - \varepsilon^{\mathrm{L3}}_1\right) \varepsilon^{\mathrm{L3}}_2 \tag{A.3}$$

which we can use to produce the combined Υ trigger scale factor out of the single-muon scale factors.

References

[1] "The standard model of paticle physics," Symmetry Magazine, Last accessed 2023. [Online]. Available: https://www.symmetrymagazine.org/standard-model

[2] Szabolcs Borsanyi and Gergely Endrodi and Zoltan Fodor and Christian Hoelbling and Sandor Katz and Stefan Krieg and Claudia Ratti and Kalman Szabo, "Transition temperature and the equation of state from lattice QCD, Wuppertal-Budapest results," *Journal of Physics: Conference Series*, vol. 316, no. 1, p. 012020, sep 2011. [Online]. Available: https://dx.doi.org/10.1088/1742-6596/316/1/012020

[3] P. Braun-Munzinger and B. Dönigus, "Loosely-bound objects produced in nuclear collisions at the LHC," *Nucl. Phys. A*, vol. 987, pp. 144–201, 2019.

[4] R. Vogt, in *Ultrarelativistic Heavy-Ion Collisions*, R. Vogt, Ed. Amsterdam: Elsevier Science B.V., 2007, pp. 385–426. [Online]. Available: https://www.sciencedirect.com/science/article/pii/B9780444521965500086

[5] A. M. Sirunyan *et al.*, "Measurement of nuclear modification factors of Υ(1S), Υ(2S), and Υ(3S) mesons in PbPb collisions at $\sqrt{s_{\mathrm{NN}}} = 5.02$ TeV," *Phys. Lett. B*, vol. 790, pp. 270–293, 2019.

[6] A. Tumasyan *et al.*, "Nuclear modification of Υ states in pPb collisions at $\sqrt{s_{\mathrm{NN}}} = 5.02$ TeV," *Phys. Lett. B*, vol. 835, p. 137397, 2022.

[7] F. Brezinski and G. Wolschin, "Gluodissociation and Screening of Υ States in PbPb Collisions at $\sqrt{s_{NN}} = 2.76$ TeV," *Phys. Lett. B*, vol. 707, pp. 534–538, 2012.

[8] H. Satz, "Quarkonium Binding and Dissociation: The Spectral Analysis of the QGP," *Nucl. Phys. A*, vol. 783, pp. 249–260, 2007.

[9] Y. Burnier, O. Kaczmarek, and A. Rothkopf, "Quarkonium at finite temperature: Towards realistic phenomenology from first principles," *JHEP*, vol. 12, p. 101, 2015.

[10] A. D. Martin, W. J. Stirling, R. S. Thorne, and G. Watt, "Parton distributions for the LHC," *Eur. Phys. J. C*, vol. 63, pp. 189–285, 2009.

[11] C. Borschensky and A. Kulesza, "Double parton scattering in pair production of J/ψ mesons at the LHC revisited," *Phys. Rev. D*, vol. 95, no. 3, p. 034029, 2017.

[12] M. Brice, "Aerial View of the CERN taken in 2008." 2008. [Online]. Available: https://cds.cern.ch/record/1295244

[13] ——, “The Linac 2 pre-injector,” 2008. [Online]. Available: http://cds.cern.ch/record/1157734

[14] CERN, “Hydrogen Bottle,” Last accessed 2023. [Online]. Available: https://visit.cern/content/hydrogen

[15] X. C. Vidal and R. C. Manzano, “LHC Pb collisions,” Last accessed 2023. [Online]. Available: https://www.lhc-closer.es/taking_a_closer_look_at_lhc/0.lhc_pb_collisions

[16] C. O’Luanaigh, “Heavy metal: Refilling the lead source for the LHC,” 2013. [Online]. Available: https://cds.cern.ch/record/1997797

[17] E. Lopienska, “The CERN accelerator complex, layout in 2022. Complexe des acclrateurs du CERN en janvier 2022,” 2022, general Photo. [Online]. Available: https://cds.cern.ch/record/2800984

[18] S. Boreham, M. Brice, P. Ginter, C. Marcelloni, and M. Hoch, “Photos from the CMS Photo Book,” 2008, CMS Collection. [Online]. Available: https://cds.cern.ch/record/1344500

[19] T. Sakuma and T. McCauley, “Detector and Event Visualization with SketchUp at the CMS Experiment,” *J. Phys. Conf. Ser.*, vol. 513, p. 022032, 2014.

[20] A. M. Sirunyan *et al.*, “Particle-flow reconstruction and global event description with the CMS detector,” *JINST*, vol. 12, no. 10, p. P10003, 2017.

[21] S. Chatrchyan *et al.*, “Alignment of the CMS Silicon Tracker during Commissioning with Cosmic Rays,” *JINST*, vol. 5, p. T03009, 2010.

[22] ——, “The CMS Experiment at the CERN LHC,” *JINST*, vol. 3, p. S08004, 2008.

[23] A. M. Sirunyan *et al.*, “Calibration of the CMS hadron calorimeters using proton-proton collision data at $\sqrt{s} = 13$ TeV,” *JINST*, vol. 15, no. 05, p. P05002, 2020.

[24] ——, “Performance of the CMS muon detector and muon reconstruction with proton-proton collisions at $\sqrt{s} = 13$ TeV,” *JINST*, vol. 13, no. 06, p. P06015, 2018.

[25] B. A. Gonzalez, “CMS Muon Drift Tubes HL-LHC Slice Test,” 10 2021.

[26] C. Collaboration, “Resistive plate chambers,” Last accessed 2023. [Online]. Available: https://cms.cern/detector/detecting-muons/resistive-plate-chambers

[27] T. Mc Cauley and C. Collaboration, "Event displays of PbPb collision events in the CMS detector at the end of 2018," 2018, CMS Collection. [Online]. Available: https://cds.cern.ch/record/2648517

[28] M. Jeitler, "The upgrade of the CMS trigger system," *JINST*, vol. 9, p. C08002, 2014.

[29] D. Kovalskyi, M. Tadel, A. Mrak-Tadel, B. Bellenot, V. Kuznetsov, C. D. Jones, L. Bauerdick, M. Case, J. Mulmenstadt, and A. Yagil, "Fireworks: A Physics Event Display for CMS," *J. Phys. Conf. Ser.*, vol. 219, p. 032014, 2010.

[30] Y. Kim, K. Lee, J. Park, G. Bak, H. Lee, D. H. Moon, and H. Kim, "Measurement of the anisotropic flow of upsilon mesons in pbpb collisions at 5.02 tev," CMS Note 2019/001, 2019.

[31] A. Stahl, E. Chapon, and O. Kukral, "Dimuon performance studies in 2018 PbPb and 2017 pp 5.02 TeV data," CMS Note 2018/316, 2022.

[32] G. Oh, S. Nanda, Z. Ye, D. H. Moon, G. Bak, P. Gwak, H. Kim, J. Park, and J. H. Yoo, "Measurements of the azimuthal anisotropy of charmonia in PbPb collisions at $\sqrt{s_{NN}} = 5.02$ TeV," CMS Note 2020/176, 2020.

[33] V. Khachatryan *et al.*, "Observation of $\Upsilon(1S)$ pair production in proton-proton collisions at $\sqrt{s} = 8$ TeV," *JHEP*, vol. 05, p. 013, 2017.

[34] R. L. Workman and Others, "Review of Particle Physics," *PTEP*, vol. 2022, p. 083C01, 2022.

[35] S. Chatrchyan *et al.*, "Observation of a New Boson at a Mass of 125 GeV with the CMS Experiment at the LHC," *Phys. Lett. B*, vol. 716, pp. 30–61, 2012.

[36] G. Aad *et al.*, "Observation of a new particle in the search for the Standard Model Higgs boson with the ATLAS detector at the LHC," *Phys. Lett. B*, vol. 716, pp. 1–29, 2012.

[37] F. Wilczek, "What QCD tells us about nature - and why we should listen," *Nucl. Phys. A*, vol. 663, pp. 3–20, 2000.

[38] ——, "QCD Made Simple," *Physics Today*, vol. 53, no. 8, pp. 22–28, 08 2000. [Online]. Available: https://doi.org/10.1063/1.1310117

[39] J. N. Guenther, "Overview of the QCD phase diagram: Recent progress from the lattice," *Eur. Phys. J. A*, vol. 57, no. 4, p. 136, 2021.

[40] D. H. Rischke, "The Quark gluon plasma in equilibrium," *Prog. Part. Nucl. Phys.*, vol. 52, pp. 197–296, 2004.

[41] M. M. Aggarwal *et al.*, “An Experimental Exploration of the QCD Phase Diagram: The Search for the Critical Point and the Onset of De-confinement,” 7 2010.

[42] M. Strickland, “Thermal Bottomonium Suppression,” *AIP Conf. Proc.*, vol. 1520, no. 1, pp. 179–184, 2013.

[43] A. Andronic *et al.*, “Heavy-flavour and quarkonium production in the LHC era: from proton–proton to heavy-ion collisions,” *Eur. Phys. J. C*, vol. 76, no. 3, p. 107, 2016.

[44] A. M. Sirunyan *et al.*, “Measurement of prompt and nonprompt charmonium suppression in PbPb collisions at 5.02 TeV,” *Eur. Phys. J. C*, vol. 78, no. 6, p. 509, 2018.

[45] T. Matsui and H. Satz, “J/ψ Suppression by Quark-Gluon Plasma Formation,” *Phys. Lett. B*, vol. 178, pp. 416–422, 1986.

[46] A. Capella, L. Bravina, E. G. Ferreiro, A. B. Kaidalov, K. Tywoniuk, and E. Zabrodin, “Charmonium dissociation and recombination at RHIC and LHC,” *Eur. Phys. J. C*, vol. 58, pp. 437–444, 2008.

[47] L. Grandchamp and R. Rapp, “Thermal versus direct J / Psi production in ultrarelativistic heavy ion collisions,” *Phys. Lett. B*, vol. 523, pp. 60–66, 2001.

[48] X. Du, M. He, and R. Rapp, “Color Screening and Regeneration of Bottomonia in High-Energy Heavy-Ion Collisions,” *Phys. Rev. C*, vol. 96, no. 5, p. 054901, 2017.

[49] R. Vogt, “Shadowing effects on J/ψ and Υ production at energies available at the CERN Large Hadron Collider,” *Phys. Rev. C*, vol. 92, no. 3, p. 034909, 2015.

[50] J. J. Aubert *et al.*, “The ratio of the nucleon structure functions $F2_n$ for iron and deuterium,” *Phys. Lett. B*, vol. 123, pp. 275–278, 1983.

[51] F. Arleo and S. Peigné, “Quarkonium suppression in heavy-ion collisions from coherent energy loss in cold nuclear matter,” *JHEP*, vol. 10, p. 073, 2014.

[52] E. G. Ferreiro and J.-P. Lansberg, “Is bottomonium suppression in proton-nucleus and nucleus-nucleus collisions at LHC energies due to the same effects?” *JHEP*, vol. 10, p. 094, 2018, [Erratum: JHEP 03, 063 (2019)].

[53] D. d’Enterria and A. M. Snigirev, “Enhanced J/Ψ-pair production from double parton scatterings in nucleus-nucleus collisions at the Large Hadron Collider,” *Phys. Lett. B*, vol. 727, pp. 157–162, 2013.

[54] F. Abe *et al.*, “Measurement of double parton scattering in $\bar{p}p$ collisions at $\sqrt{s} = 1.8$ TeV,” *Phys. Rev. Lett.*, vol. 79, pp. 584–589, 1997.

[55] V. M. Abazov *et al.*, "Double parton interactions in γ+3 jet events in pp^{-} bar collisions $\sqrt{s} = 1.96$ TeV." *Phys. Rev. D*, vol. 81, p. 052012, 2010.

[56] G. Aad *et al.*, "Measurement of hard double-parton interactions in $W(\rightarrow l\nu)+$ 2 jet events at $\sqrt{s}$=7 TeV with the ATLAS detector," *New J. Phys.*, vol. 15, p. 033038, 2013.

[57] D. G. d'Enterria, "Hard scattering cross-sections at LHC in the Glauber approach: From pp to pA and AA collisions," 2 2003.

[58] W. Herr and B. Muratori, "Concept of luminosity," 2006. [Online]. Available: https://cds.cern.ch/record/941318

[59] V. Khachatryan *et al.*, "The CMS trigger system," *JINST*, vol. 12, no. 01, p. P01020, 2017.

[60] R. Frhwirth, "Application of Kalman filtering to track and vertex fitting," *Nuclear Instruments and Methods in Physics Research Section A: Accelerators, Spectrometers, Detectors and Associated Equipment*, vol. 262, no. 2, pp. 444–450, 1987.

[61] C. Collaboration, "Data formats and data tiers," 2016, Last accessed 2023. [Online]. Available: https://twiki.cern.ch/twiki/bin/view/CMSPublic/WorkBookDataFormats

[62] T. Sjöstrand, S. Ask, J. R. Christiansen, R. Corke, N. Desai, P. Ilten, S. Mrenna, S. Prestel, C. O. Rasmussen, and P. Z. Skands, "An introduction to PYTHIA 8.2," *Comput. Phys. Commun.*, vol. 191, pp. 159–177, 2015.

[63] I. P. Lokhtin, L. V. Malinina, S. V. Petrushanko, A. M. Snigirev, I. Arsene, and K. Tywoniuk, "Heavy ion event generator HYDJET++ (HYDrodynamics plus JETs)," *Comput. Phys. Commun.*, vol. 180, pp. 779–799, 2009.

[64] S. Agostinelli *et al.*, "GEANT4: A Simulation toolkit," *Nucl. Instrum. Meth.*, vol. A506, pp. 250–303, 2003.

[65] J. E. Gaiser, "Charmonium Spectroscopy From Radiative Decays of the J/ψ and ψ'," Other thesis, 8 1982.

[66] D. Martínez Santos and F. Dupertuis, "Mass distributions marginalized over per-event errors," *Nucl. Instrum. Meth. A*, vol. 764, pp. 150–155, 2014.

[67] D. d'Enterria and A. M. Snigirev, "Pair production of quarkonia and electroweak bosons from double-parton scatterings in nuclear collisions at the LHC," *Nucl. Phys. A*, vol. 931, pp. 303–308, 2014.

[68] M. Cacciari, S. Frixione, N. Houdeau, M. L. Mangano, P. Nason, and G. Ridolfi, "Theoretical predictions for charm and bottom production at the LHC," *JHEP*, vol. 10, p. 137, 2012.

[69] M. Cacciari, M. L. Mangano, and P. Nason, “Gluon PDF constraints from the ratio of forward heavy-quark production at the LHC at $\sqrt{S} = 7$ and 13 TeV,” *Eur. Phys. J. C*, vol. 75, no. 12, p. 610, 2015.

[70] S. J. Brodsky and J.-P. Lansberg, “Heavy-Quarkonium Production in High Energy Proton-Proton Collisions at RHIC,” *Phys. Rev. D*, vol. 81, p. 051502, 2010.

[71] Y. Feng, J.-P. Lansberg, and J.-X. Wang, “Energy dependence of direct-quarkonium production in *pp* collisions from fixed-target to LHC energies: complete one-loop analysis,” *Eur. Phys. J. C*, vol. 75, no. 7, p. 313, 2015.

[72] G. Falmagne, “How to apply scale factors on asymmetric dimuons/trimuons?” 2020, CMS Internal Document.